UNIVERSIDADE FEDERAL DE MINAS GERAIS

Instituto de Ciências Exatas

Programa de Pós-Graduação em Física

Rafael dos Reis Barreto

NON-TRIVIAL SURFACE EFFECTS IN NOVEL GeS AND Sb4Te3 LAYERED MATERIALS

Belo Horizonte
2024

Rafael dos Reis Barreto

NON-TRIVIAL SURFACE EFFECTS IN NOVEL GeS AND Sb_4Te_3 LAYERED MATERIALS

Tese apresentada ao Programa de Pós-Graduação em Física da Universidade Federal de Minas Gerais como requisito parcial para obtenção do grau de Doutor em Ciências, área de concentração: Física.

Orientador: Prof. Dr. Rogério Magalhães Paniago

Coorientador: Prof. Dr. Mario Sergio de Carvalho Mazzoni

Belo Horizonte
2024

Dados Internacionais de Catalogação na Publicação (CIP)

B273n Barreto, Rafael dos Reis.

Non-trivial surface effects in novel GeS and Sb_4Te_3 layered materials / Rafael dos Reis Barreto. – 2024.

129 f. : il.

Orientador: Rogério Magalhães Paniago.

Coorientador: Mário Sérgio de Carvalho Mazzoni.

Tese (doutorado) – Universidade Federal de Minas Gerais, Departamento de Física.

Bibliografia: f. 111-129.

1. Ferroeletricidade. 2. Estrutura eletrônica. 3. Microscopia. 4. Espectroscopia de tunelamento. 5. Poços quânticos. I. Título. II. Paniago, Rogério Magalhães. III. Mazzoni, Mário Sérgio de Carvalho. IV. Universidade Federal de Minas Gerais, Departamento de Física.

CDU – 537.226 (043)

Ficha catalográfica elaborada por Romário Martins Ribeiro – CRB6 3595

Biblioteca Professor Manoel Lopes de Siqueira – Departamento de Física - UFMG

SEI/UFMG - 3106798

UNIVERSIDADE FEDERAL DE MINAS GERAIS

INSTITUTO DE CIÊNCIAS EXATAS

PROGRAMA DE PÓS-GRADUAÇÃO EM FÍSICA

ATA DE DEFESA DE TESE

ATA DA SESSÃO DE ARGUIÇÃO DA 426ª TESE DO PROGRAMA DE PÓS-GRADUAÇÃO EM FÍSICA, DEFENDIDA POR RAFAEL DOS REIS BARRETO orientado pelo professor Rogério Magalhães Paniago e coorientado pelo professor Mário Sérgio de Carvalho Mazzoni, para obtenção do grau de **DOUTOR EM CIÊNCIAS, área de concentração sica**. Às 14:00 horas de doze de março de dois mil e vinte e quatro, na Sala de Seminários do Departamento de Física - 4117, reuniu-se a Comissão Examinadora, composta pelos professores **Rogério Magalhães Paniago** (Orientador - Departamento de Física/UFMG), **Mário Sérgio de Carvalho Mazzoni** (Coorientador - Departamento de Física/UFMG), **Maria Carolina de Oliveira Aguiar** (Departamento de Física/UFMG), **Leandro Malard Moreira** (Departamento de Física/UFMG), **Arnaldo Naves de Brito** (Instuto de Física Gleb Wataghin/UNICAMP) e a doutora **Bruna Fernanda Baggio** (LNNano/CNPEM) para dar cumprimento ao Argo 37 do Regimento Geral da UFMG, submetendo o mestre **RAFAEL DOS REIS BARRETO** à arguição de seu trabalho de Tese de Doutorado, que recebeu o tulo de **"Non-Trivial surface effects in novel GeS and Sb4Te3 layered materials".** O candidato fez uma exposição oral de seu trabalho durante aproximadamente 50 minutos. Após esta, os membros da comissão prosseguiram com a sua arguição, e apresentaram seus pareceres individuais sobre o trabalho, concluindo pela aprovação do candidato.

Belo Horizonte, 12 de março de 2024.

Prof. Rogério Magalhães Paniago
Orientador do estudante
Departamento de Física/UFMG

Prof. Mário Sérgio de Carvalho Mazzoni
Coorientador do estudante
Departamento de Física/UFMG

Profa. Maria Carolina de Oliveira Aguiar
Departamento de Física/UFMG

Prof. Leandro Malard Moreira
Departamento de Física/UFMG

Prof. Arnaldo Naves de Brito
Instuto de Física Gleb Wataghin/UNICAMP

Dra. Bruna Fernanda Baggio
LNNano/CNPEM

Candidato: Rafael dos Reis Barreto

Documento assinado eletronicamente por **Rafael dos Reis Barreto**, **Usuário Externo**, em 13/03/2024, às 14:42, conforme horário oficial de Brasília, com fundamento noart. 5º do Decreto nº 10.543, de 13 de novembro de 2020.

Documento assinado eletronicamente por **Arnaldo Naves de Brito**, **Usuário Externo**, em 13/03/2024, às 14:50, conforme horário oficial de Brasília, com fundamento no art. 5º do Decreto nº 10.543, de 13 de novembro de 2020.

Documento assinado eletronicamente por **Leandro Malard Moreira**, **Professor do Magistério Superior**, em 13/03/2024, às 15:23, conforme horário oficial de Brasília, com fundamento no art. 5º do Decreto nº 10.543, de 13 de novembro de 2020.

Documento assinado eletronicamente por **Rogerio Magalhaes Paniago**, **Professor do Magistério Superior**, em 13/03/2024, às 16:24, conforme horário oficial de Brasília, com fundamento no art. 5º do Decreto nº 10.543, de 13 de novembro de 2020.

Documento assinado eletronicamente por **Rogerio Magalhaes Paniago**, **Professor do Magistério Superior**, em 13/03/2024, às 16:24, conforme horário oficial de Brasília, com fundamento no art. 5º do Decreto nº 10.543, de 13 de novembro de 2020.

Documento assinado eletronicamente por **Rogerio Magalhaes Paniago**, **Professor do Magistério Superior**, em 13/03/2024, às 16:24, conforme horário oficial de Brasília, com fundamento no art. 5º do Decreto nº 10.543, de 13 de novembro de 2020.

Documento assinado eletronicamente por **Rogerio Magalhaes Paniago**, **Professor do Magistério Superior**, em 13/03/2024, às 16:24, conforme horário oficial de Brasília, com fundamento no art. 5º do Decreto nº 10.543, de 13 de novembro de 2020.

A autencidade deste documento pode ser conferida no site https://sei.ufmg.br/sei/controlador_externo.php?acao=documento_conferir&id_orgao_acesso_externo=0 , informando o código verificador **3106798** e o código CRC **1F0423FF**.

Agradecimentos

Gostaria de agradecer aos meus pais, Vanderley e Marlúcia, minha madrastra Ione e minha irmã Natália, por estarem sempre presentes e me apoiarem incondicionalmente. Seu encorajamento, afeto, união e fé em mim foram fundamentais para minha jornada acadêmica.

Também quero agradecer ao meu orientador, o professor Rogério Paniago, pela paciência e comprometimento durante todo o período do meu doutorado. Nossa relação sempre foi de excelente apesar de inúmeras discurssões, todas com intuito de bem comum, seja da parte cientifica ou pessoal. Seus ensinamentos, conselhos e discussões foram essenciais para meu desenvolvimento como pesquisador, e sua abordagem prática e aplicada da ciência tem sido uma grande fonte de inspiração.

Agradeço a meu coorientador, Mario Mazzoni pelos seus valiosos ensinamentos teóricos, e por sua paciência, dedicação e disponibilidade em me ajudar sempre que precisei. Apesar de nunca ter trabalhado com DFT antes, sempre se mostrou disposto a me ensinar e me auxiliar nessa nova caminhada. Sua orientação foi fundamental para meu desenvolvimento acadêmico e profissional.

Também sou grato ao Angelo Malachias (meu coorientador de consideração) por seu suporte técnico e científico durante toda minha jornada de doutorado. Sempre fez parte de todo trabalho que eu realizei ao longo do doutarado e também responsável pelos momentos mais divertidos dentro do laboratório. Foi um prazer disputar a final de tocaia no pantanal com o Dr. Angelo.

Assim como sou grato ao Gustavo Sáfar por estar sempre pronto para me ajudar com dúvidas relacionadas ao trabalho assim como agradeço ainda ao corpo técnico do departamento de Física, pelos valiosos ensinamentos técnicos e experimentais que foram fundamentais para meu desenvolvimento como físico experimental e aplicado.

Por fim, agradeço aos meus amigos e colegas do departamento de física, dos laboratórios de Nanoscopia UHV e Nanomateriais pelo suporte emocional e experimental ao longo de minha jornada acadêmica. E também às agências de financiamento FAPEMIG, INCT-Nanocarbono, CNPq e CAPES pelo apoio financeiro.

Resumo

Neste trabalho, estudamos dois materiais que possuem empilhamento por camadas separados por ligações de Van der Walls, o Sulfeto de Germânio (GeS) e o Telureto de Antimônio (Sb_4Te_3). Utilizamos microscopia e espectroscopia de tunelamento (STM/STS) e espectroscopia de fotoemissão resolvida em ângulo (ARPES) para investigar as propriedades únicas desses dois materiais.

O primeiro projeto consistiu no estudo da ferroeletricidade no plano da superfície do GeS utilizando STM/STS. Obtivemos um resultado experimental notável de fenômenos dependentes da espessura à temperatura ambiente, relacionados à fase ferroelétrica superficial induzida em nanocamadas de GeS. Utilizamos deposição em fase vapor para sintetizar nanoflakes de sulfeto de germânio em um substrato de grafite pirolítico altamente orientado (HOPG). Os nanoflakes com diferentes espessuras foram estudados usando STM/STS e modelados por meio de cálculos de teoria do funcional da densidade (DFT). A corrente de tunelamento foi alterada pela espessura do material. Observamos claramente um padrão de histerese, ao qual atribuímos um comportamento ferroelétrico bidimensional, consistente com as condições de polarização. Esse efeito aumenta à medida que o número de camadas é reduzido.

O segundo projeto foi dedicado ao estudo da estrutura eletrônica do Sb_4Te_3, utilizando medidas de ARPES em alto resolução no material topológico Sb_4Te_3. Utilizando DFT combinado com medidas de ARPES, observamos que o comportamento topológico exibido por Sb_2Te_3 e Sb_2 persiste, caracterizado por estados eletrônicos que surgem do acoplamento spin-órbita, warping hexagonal associado à simetria de inversão temporal e independência de energia de fótons nesses estados superficiais. Ao comparar os resultados com as bandas do bulk e da superfície, observamos estados eletrônicos confinados entre o Sb_4Te_3 bulk e a terminação em Sb_2. A independência em energia de fótons desse estado indica confinamento ao longo da direção de empilhamento.

Palavras-chave Ferroeletricidade, materiais lamelares, microscopia e espectroscopia de tunelamento de varredura (STM/STS), espectroscopia de fotoemissão resolvida em ângulo (ARPES), poços quânticos, warping hexagonal, materiais topológicos.

Abstract

In this work we have studied different layered materials, Germanium Sulfide (GeS) and Antimony Telurite (Sb_4Te_3). We used scanning tunneling microscopy and spectroscopy (STM/STS) and angle-resolved photoemission spectroscopy (ARPES) to study the unique properties of these two materials.

The first project was dedicated to the study of the surface in-plane ferroeletricity of GeS using STM/STS. We obtained a remarkable experimental STS evidence of thickness-dependent phenomena surface-induced ferroelectricity in germanium sulfide nano-flakes. We used vapor-phase deposition to synthesize ultrathin nano-flakes on a highly oriented pyrolytic graphite substrate (HOPG). Nanostructures of variable thicknesses were studied using scanning tunneling microscopy and spectroscopy and the electronic structure was modelled using density functional theory (DFT) calculations. Tunneling current under negative-positive-negative biases was altered by the thickness of the material. We clearly observe a hysteresis pattern, which we attribute to a two-dimensional ferroelectric behavior, consistent with screening conditions of polarization charges. This effect increases as the number of layers is reduce.

The second project was dedicated to the study of the electronic structure of Sb_4Te_3. We present HR-ARPES measurements conducted on this topological material. Using DFT combined with ARPES measurements, we observe that the topological behavior exhibited by Sb_2Te_3 and Sb_2 persists, characterized by electronic states which emerge from spin-orbit coupling, hexagonal warping associated with time reversal symmetry and photon-energy independence in these surface states. By comparing the results with the calculated bulk and surface bands, we observe a confined electronic state between the bulk Sb_4Te_3 and the Sb_2 termination. The photon-energy independence of this state indicates confinement along the stacking direction.

Keywords: Ferroelectricity, layered materials, scanning tunnelling microscopy (STM) and spectroscopy (STS), angle-resolved photonemission spectroscopy (ARPES), quantum well, hexagonal warping, topological materials.

Contents

1. Introduction

This thesis concerns the study of the electronic properties of novel 2D materials. More specifically, we have chosen few-layer structures of the semiconductor Germanium Sulfide (GeS), and the topological material antimony telurite (Sb_4Te_3), built upon intercalation of Sb_2Te_3 and Sb_2 layers.

In recent years, layered materials exhibiting van der Waals interactions in their stacking configurations have attracted significant attention by the scientific community, due to their novel electronic properties and future technological application [1], [2], [3], [4]. These materials manifest diverse properties, such as enhanced surface electrical conductivity, electronic transitions, quantum well states, charge storage capabilities and ferroelectricity [5], [6], [7], [8]. These properties arise from alterations in their stacking patterns. These emergent properties hold the promise of the developments of novel device technologies [9], [10].

Germanium sulfide is a layered semiconductor with a crystal structure analogous to that of black phosphorus and SnS, and with a direct bandgap in the visible region (1.65 eV)[11], [12], [13]. The anisotropic crystal structure of GeS gives rise to anisotropy in the optoelectronic properties, such as polarized optical absorption [11], [12], [13], and photo-conductivity [14], as well as unusual electronic properties, including multiferroic behavior with coupled ferroelectricity and ferroelasticity [15], [16], [17]and potential applications in third-generation photovoltaics [18].

One important property of GeS is its low toxicity and environmental impact when compared with other semiconductors, e.g., those containing heavy metals such as cadmium or lead [19]. GeS nanowires have emerged as important semiconductor nanostructures and efficient light emitters with a tunable interlayer twist [20], [21]. GeS nanoribbons and 2D flakes also show potential in electronic and optoelectronic applications for telecommunication and computing, as visible-light photodetectors with high sensitivity and broad spectral response. It is also used as a photoabsorbers for use in solar energy conversion [21], [22], [23]. Similar to other 2D layered materials, GeS is expected to show thickness-dependent properties, i.e., phenomena in the ultra-thin limit, e.g., absorption dominated by tightly bound excitons with large binding energy (1 eV) [24], [25]. One thickness-dependent property that we observed in

our work was the dependence of the tunneling current upon the GeS thickness. Scanning tunneling spectroscopy, when combined with tunneling microscopy, is a powerful technique to assess the hysteretic electronic behavior correlated with the film structure [26], [27], [28], [29]. In the present work, we focus on this technique, and we demonstrate the existence of a thickness-dependent phenomenon in few-layer GeS associated with the tunneling current that can be ascribed to ferroelectric behavior. This is observed as a hysteretic loop when forward and backward biases are applied to the same region of the GeS flake, deposited on highly-oriented pyrolytic graphite (HOPG).

In this context, the recent discovery of ferroelectricity in two-dimensional van der Waals materials represents a unique opportunity to unveil this phenomenon in the ultrathin limit [6], [30], [31]. Ferroelectric materials have received significant attention due to the fundamental aspects of the physics involved in their behavior as well as to their switchable properties, which make them attractive in a variety of applications, including non-volatile memories and neuromorphic computing [32], [33], [34], [35], [36]. Achieving stable ferroelectricity in ultrathin films is particularly important, with technological implications in the miniaturization of sensors, memories and optoelectronic devices [37], [38]. However, the investigation of polarization effects in the surface structure and the detailed description of the hysteretic behavior are still a challenge. We characterized the GeS/HOPG heterostructure by STS measurements, and compared the spectra with first-principles calculations based on density functional theory, which allowed for the mapping of the density of states (DoS) both in the bulk and in the limit of low dimensionality.

Topological materials have also been extensively studied due to their unique properties. For instance, these materials may be insulators in their bulk and conductors at the surface, and topological surface states are protected from backscattering. As a result, several studies have focused on the electronic behavior, aiming to apply them in novel devices. The incorporation of these materials into current electronics, however, requires a complete understanding of their properties under different conditions.

The second study in this thesis is on the antimony tellurite family, specifically Sb_4Te_3, which exhibits a stacking arrangement comprising two quintuple-layers (QL) of Sb_2Te_3 and two bi-layers of Sb_2 [39], [40]. Notably, Sb_4Te_3 consists of both a 3D topological insulator material (Sb_2Te_3) and a 2D topological insulator (Sb_2), rendering it an intriguing subject for

investigation [41], [42]. Despite its potential, Sb_4Te_3 has remained relatively unexplored. This work aims to provide a comprehensive picture of this material for future device applications.

We have synthesized Sb_4Te_3 using the Bridgman technique, following the established procedure outlined in the literature [40]. Upon successful synthesis, we characterized the material using Energy Dispersive Electron Spectroscopy (EDS) to verify the Sb/Te atomic ratio. Raman spectroscopy was employed to confirm the structural phase. Domains containing Sb_4Te_3 and Sb_2 were identified in our sample. By utilizing X-ray powder diffraction (XPD) and crystal truncation rod (CTR), we determined the percentage of each phase and the average presence of each surface termination. Combining these results with Scanning Tunneling Microscopy (STM) allowed us to confirm the presence of all possible surfaces.

After this investigation, we conducted Angle-Resolved Photoemission Spectroscopy (ARPES) measurements to explore the electronic band properties of Sb_4Te_3. Firstly, we conducted ARPES measurements using a helium lamp to characterize the sample. HR-ARPES measurements were performed at Bloch Beamline of the Sweedish Syncrothon lighsource Max IV. Our ARPES observations revealed clear signatures indicative of topological behavior. The presence of surface states, as predicted by density functional theory calculations, displaying hexagonal warping, indicate the persistence of time-reversal symmetry in this material. Moreover, the absence of photon-energy dependence in these states confirmed their surface nature.

The HR-ARPES results revealed two additional electronic bands distinct from the bulk and surface states. These bands exhibit the same energy dispersion along the Γ-M direction as reported for Sb_2 quantum wells [43], [44], [45], [46]. We attributed these bands to an electronically confined states situated between the Sb_4Te_3 bulk and an additional Sb_2 surface layer. In this scenario, Sb_4Te_3 acts as a potential barrier for this additional surface layer. This configuration creates a quantum well, confining electrons in the stacking direction. This localized behavior was further examined by varying the photon energy, revealing a localized in-plane behavior, as evidenced by the photon-energy independence.

This thesis is organized into the following chapters:

Chapter 2 provides an overview of the fundamental physics underlying the two main projects: topological materials and ferroelectricity.

Chapter 3 delves into the theoretical framework of density functional theory, laying the groundwork for understanding the computational methods employed throughout the thesis.

Chapter 4 offers an in-depth explanation of the scanning tunneling microscopy/spectroscopy and angle-resolved photoemission spectroscopy techniques, which were pivotal in the experimental investigations conducted in this work.

Chapter 5 presents the first project, focusing on the exploration of ferroelectricity at the 2D limit of GeS using scanning tunneling spectroscopy technique.

Chapter 6 details the second project, which involves the investigation of the topological material Sb_4Te_3. This chapter discusses the observations made through angle-resolved photoemission spectroscopy in conjunction with density functional theory, highlighting the topological states and quantum confined states within this material.

Chapter 7 provides a comprehensive summary of the findings from both projects.

Chapter 8 serves to elucidate the scientific contributions made throughout the duration of the PhD program.

2. Theoretical Foundation of Condensed Matter

2.1 Semiconductors

It is well known that condensed matter exhibits three basic electronic states, conducting (metallic), semiconducting and insulating. Metallic states are those where the Fermi level cut the valance and conduction band, as a consequence, electrons are free to move, which rise to a relatively high conductivity. When there is a gap between the valence and conduction bands the material can be semiconducting (for small gap) or an insulator (for large gap). Semiconductors can be formed by pure elements, such as silicon or germanium, or compounds such as gallium arsenide or cadmium selenide. In figure 1 we show the difference between these electronic states.

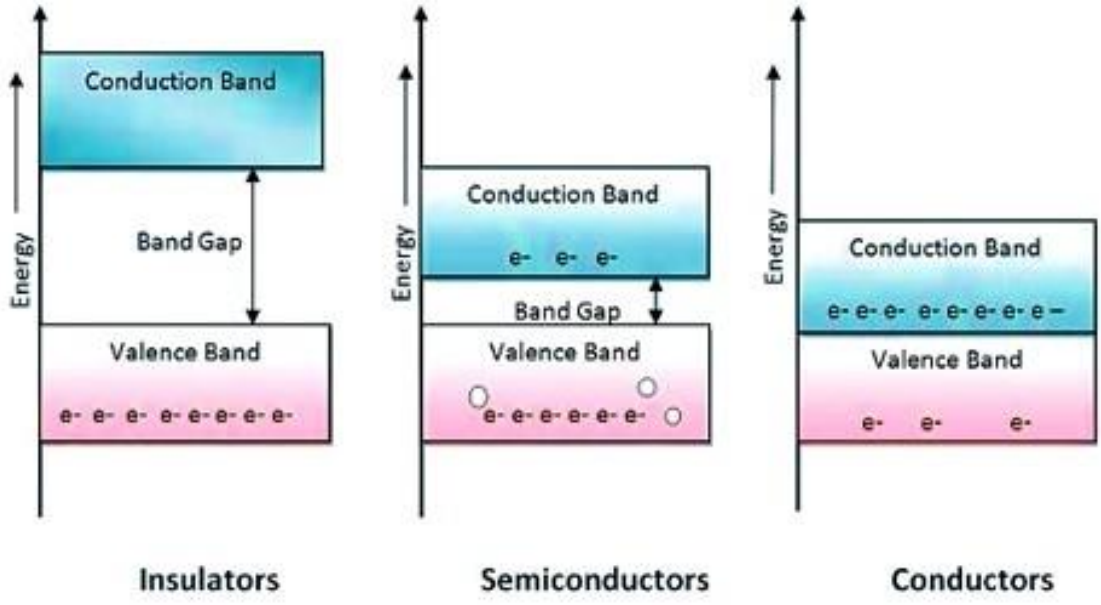

Figure 1: Band model example show the different between a metal, an insulator and a semiconductor.

Table 1 shows some examples of energy gaps of a few semiconductors' materials.

Material	Gap at 300K (eV)	Classification
Ge	0.66	Semiconductor
Si	1.12	Semiconductor
GaAs	1.42	Semiconductor
C (Diamond)	5.47	Insulator
SiO_2	9.0	Insulator
Si_3O_4	5.0	Insulator

Table 1: Table with some examples of semiconductor and insulators materials [47].

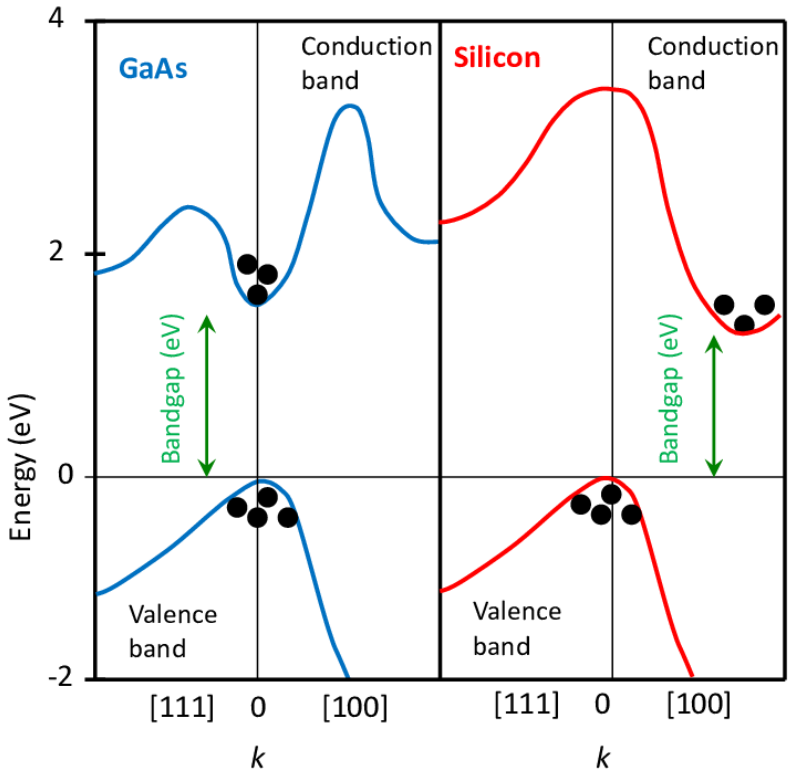

Figure 2: Band structure of GaAs (left) and Si (right). The red lines show the energy gap in both cases.

Figure 2 presents the band structure of two types of semiconductors: on the left, direct band gap (GaAs), and, on the right, an indirect gap semiconductor (Si). If the top of the valence band and the bottom of the conduction band are localized at the same k point, the gap is direct, if its is in a different k point, its is called indirect gap. Scanning tunneling spectroscopy direct measures

the local electronic density of states. Angle-resolved spectroscopy is able to determine the global band structure of a specific material. In figure 3 the connection between the density of states and the band structure is illustrated for Si. In essence, the density of states is a momentum integral of the electronic states for a given energy range.

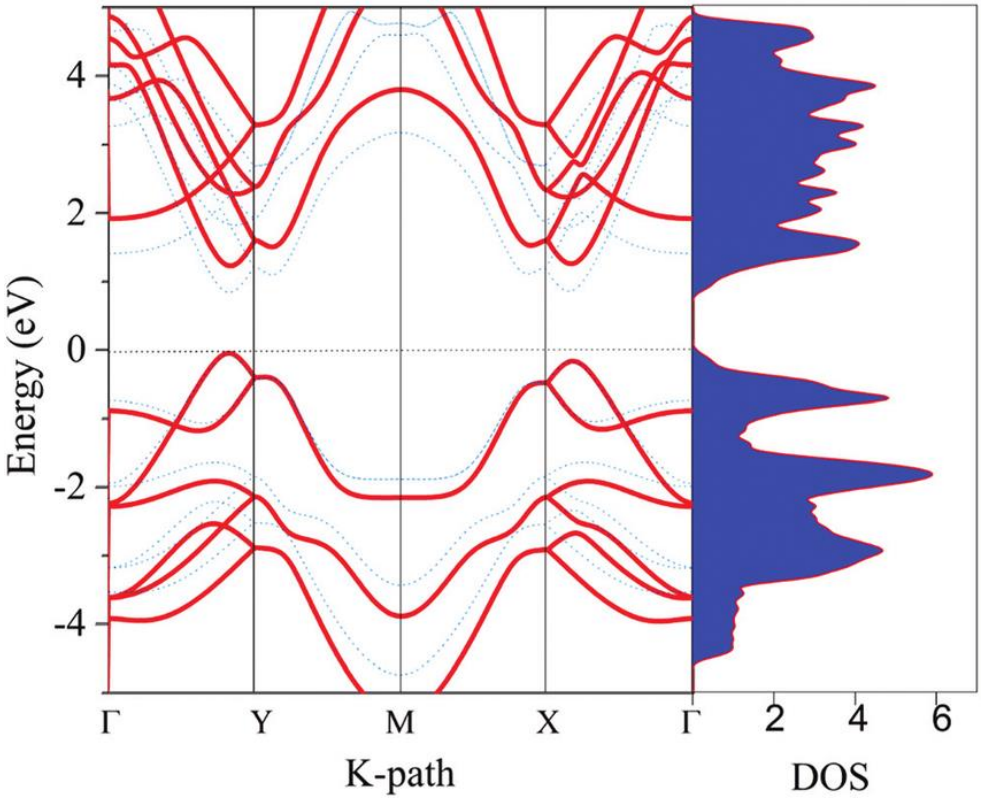

Figure 3: Electronic band structure of the single-layered SnSe based on PBE (blue dashed line) and HSE06 (red solid line) functionals and the corresponding density of states (DOS). The Fermi energy level is shift to 0 eV [48].

2.2 Physical Properties of Low Dimensional System

Reducing the number of layers in a nanomaterial, often referred to as nanoscale thinning, can have various effects on its properties, behavior and applications. The specific outcomes depend on the type of material, its structure, and the intended application. We discuss below selected effects that are relevant to this thesis.

Quantum Confinement Effects: In nanomaterials, particularly two-dimensional structures like graphene or transition metal dichalcogenides (TMDs), quantum confinement effects arise due to the reduced dimensions of the material. As the number of layers decreases, the electronic band structure becomes quantized, leading to discrete energy levels. In semiconducting materials, this can result in the control of the band structure, impacting the electronic properties of the material. For example, in TMDs, a transition from an indirect to a direct bandgap may occur as the number of layers is reduced. Quantum confinement effects also play a crucial role in applications, such as in nanoelectronics, where precise control over electronic states is essential.[49]

Enhanced Surface Effects: Reducing the number of layers in nanomaterials increases the significance of surface effects. At the nanoscale, a higher percentage of atoms reside near or at the surface, influencing the material's reactivity, catalytic activity and interactions with the environment. Surface-dominated properties, such as topological states, wettability and chemical reactivity, become more prominent. Heightened surface reactivity is exploited in catalysis, where nanocatalysts with optimized surface effects demonstrate enhanced activity. Additionally, in nanocomposites, the surface interactions play a pivotal role in determining the overall material properties [50], [51], [52].

Optical Properties: Thinning nanomaterials may affect their optical properties in significant ways. In 2D materials like graphene or TMDs, the number of layers directly impacts their absorption and emission spectra [53]. As the number of layers decreases, quantum confinement effects become more pronounced, leading to tunable optical properties. Quantum dots, semiconductor nanoparticles with size-dependent optical behaviors, exhibit changes in absorption and emission characteristics, as the number of layers is reduced. This tunability is exploited in applications such as sensors, imaging devices, and displays [54], [55].

Mechanical Properties: The mechanical properties of nanomaterials are strongly influenced by their thickness. Single-layer graphene, for example, exhibits remarkable strength, flexibility, and elasticity. Reducing the number of layers in other materials can affect their stiffness, strength, and flexibility, making them suitable for applications in nanocomposites, flexible electronics, and advanced materials requiring tailored mechanical properties. The enhanced mechanical properties at the nanoscale open avenues for the development of lightweight and high-strength materials [56], [57].

Electronic Properties, Energy Storage and Transport: Electronic properties in nanomaterials, particularly those with layered structures, are intricately linked to the number of layers. Each layer contributes to the overall electrical behavior, and quantum effects come into play as dimensions are reduced. The tunability of electrical conductivity and semiconducting behavior by adjusting the number of layers is crucial for designing electronic devices, sensors, and other nanoelectronic applications. Also, it is reported that different materials become ferroeletric at the 2D limit. In the realm of energy storage and transport, nanomaterials play a pivotal role. By reducing the number of layers, the efficiency, conductivity, and overall performance of materials used in batteries, supercapacitors, and thermoelectric devices can be optimized. Tuning the nanomaterial structure allows for tailoring energy storage capacitors, charge/discharge rates, and thermal conductivity [58], [59], [60], [61], [62], [63], [64].

Magnetic Properties: Materials with magnetic properties, such as thin films or nanoparticles, exhibit changes in behavior as the number of layers is reduced. In magnetic multilayers, the interlayer coupling between magnetic moments may vary, affecting the overall magnetic behavior. Understanding and controlling these magnetic properties are crucial for applications in data storage, sensors, and magnetic devices. Nanomaterials with tailored magnetic properties have already revolutionize information storage and sensing technologies [65], [66], [67].

Exploring these diverse aspects of nanomaterials as number of layers is reduced provides a comprehensive understanding of the unique properties and potential applications that arise in the nanoscale regime. Researchers and engineers can leverage this knowledge to design innovative nanomaterials for a wide range of technological applications.

2.3 Topological Insulators

2.3.1 Quantum Hall Effect

Edwin Hall gave the first steps that led to the study of topological insulators in 1879 with the discovery of the Hall Effect [68]. Almost a century later, Klauss von Klitzing investigated

the Hall effect in samples with high electron mobility. They observed that, for a MOSFET with a large magnectic field applied, the Hall resistivity ρ_H presents plateaus which are integer multiples of $\frac{e^2}{2}$, as represented in figure 4 [69].

The conductivity plateaus are due to Landau levels. Landau levels represent the formal solution for the expected classical behavior of a closed electrons orbits inside the material when a finite magnetic field is applied. However, at the edges of the material these orbits can not be closed, forming additional surface electron open trajectories.

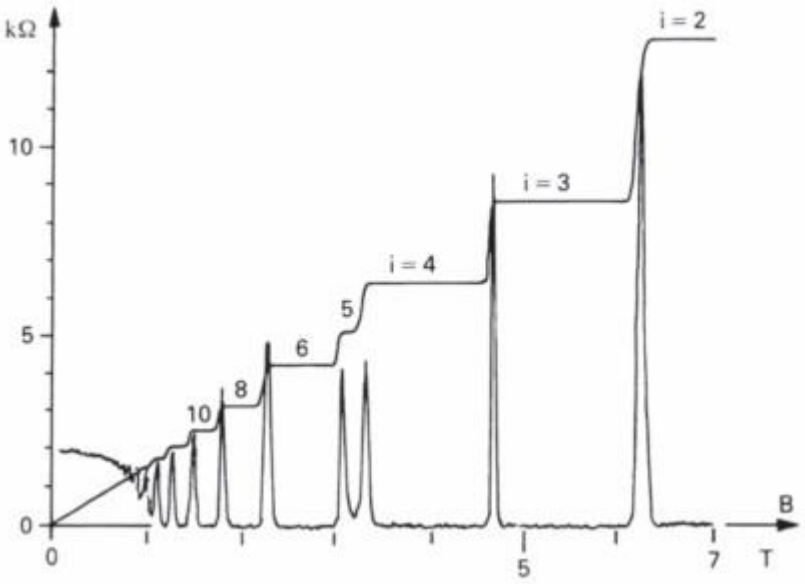

Figure 4: Longitudinal resistivity ρ_{xx} and transverse ρ_H as a function of the applied magnetic field. For smaller magnetic field ($B < 1T$), we perceive a proportionality between B and the Hall resistance for $\rho_H = -\frac{B}{ne}$, as expected. When the magnetic field exceeds $2T$, a strange structure appears on the curve, which for higher fields extremes reveals itself as a staircase with steps of increasing height [70], [71].

These edge trajectories lead to electronic states that propagate along the material in only one direction. They have chirality but no quantized energy. Therefore, these states have no energy gap. They are metallic and can conduct electric current without being scattered by impurities. This Quantum Hall Effect (QHE) was the first observation of a state of matter that has energy gap in the bulk, but with a conducting state at the edge [32], [33].

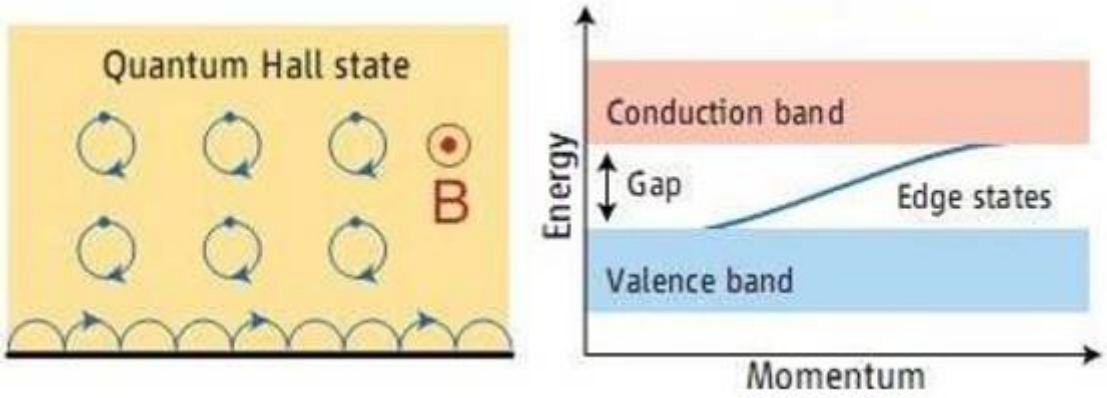

Figure 5: Electron orbit is broken at the surface giving rise to edge current [72].

2.3.2 Topology Concepts and Berry Phase

One of the important concepts that is discussed in this section is Berry phase. It is born as a correction to the quantum adiabatic theorem and has a deep connection with the phenomenon of topological insulator. To show how this quantum phase arises in the adiabatic theorem, let us consider a Hamiltonian $H[\boldsymbol{R}(t)]$ parameterized by $\boldsymbol{R} = (R_1(t), R_2(t), \dots, R_n(t))$, where $R_i(t)$ referes to the i-th state, such that it has at least on eigenvalue $E_n[\boldsymbol{R}(t)]$ associated with eigenfunction $|\Psi_n[\boldsymbol{R}(t)]\rangle$. By adiabatically varying the parameter $R(t)$ so that the system does not change its quantum state, the eigenstate can be written as [73]:

$$|\Psi_n[\boldsymbol{R}(t)]\rangle' = e^{i\phi_n(t)}|\Psi_n[\boldsymbol{R}(t)]\rangle, \tag{1}$$

where $\phi_n(t)$ is the phase that the state will get through this process. $|\Psi_n[\boldsymbol{R}(t)]\rangle'$ is the eigenfunction after the adiabatically variation. We can then write the following time-dependent Schrödinger equation for this state.

$$i\hbar\frac{d}{dt}\left[e^{i\phi_n(t)}\,|\Psi_n[\boldsymbol{R}(t)]\rangle\right] = H[\boldsymbol{R}(t)]e^{i\phi_n(t)}\,|\Psi_n[\boldsymbol{R}(t)]\rangle. \tag{2}$$

Then multiplying the entire expression 2 by the conjugate complex $\langle\Psi_n[\boldsymbol{R}(t)]|e^{-i\phi_n(t)}$ we have:

$$\frac{d}{dt}\phi_n(t) = \langle\Psi_n[\boldsymbol{R}(t)]|i\nabla_R|\Psi_n[\boldsymbol{R}(t)]\rangle\frac{d}{dt}\boldsymbol{R}(t) - \frac{E_n[\boldsymbol{R}(t)]}{\hbar}. \tag{3}$$

Integrating both sides of the equation 3 in the interval $0 \le t' \le t$, we get:

$$\Delta\phi_n = \int_0^t \langle \Psi_n[\boldsymbol{R}(t')]|i\nabla_R|\Psi_n[\boldsymbol{R}(t')]\rangle \frac{d}{dt'}\boldsymbol{R}(t')dt' - \frac{1}{\hbar}\int_0^t E_n[\boldsymbol{R}(t')]dt',$$

$$\Delta\phi_n = \int_{\boldsymbol{R}(0)}^{\boldsymbol{R}(t)} \langle \Psi_n[\boldsymbol{R}(t')]|i\nabla_R|\Psi_n[\boldsymbol{R}(t')]\rangle d\boldsymbol{R} - \frac{1}{\hbar}\int_0^t E_n[\boldsymbol{R}(t')]dt',$$

$$\Delta\phi_n = \int_{\boldsymbol{R}(0)}^{\boldsymbol{R}(t)} \boldsymbol{A}_n(\boldsymbol{R}) \cdot d\boldsymbol{R} - \frac{1}{\hbar}\int_0^t E_n[\boldsymbol{R}(t')]dt', \quad (4)$$

Note that are two distinct terms contributing to the variation of the complete phase of the system. The first term is called the geometric phase or also Berry phase, which will define as Φ_γ, where $\boldsymbol{A}_n(\boldsymbol{R}) = \langle \Psi_n[\boldsymbol{R}(t')]|i\nabla_R|\Psi_n[\boldsymbol{R}(t')]\rangle$ is know as the Berry connection of eigenstate n. The second term is called the dynamic phase.

It is interesting to note that $\boldsymbol{A}_n(\boldsymbol{R})$ is variant under gauge transformation, so it has no physical reality. But in analogy with electromagnetism, likewise that the potential vector $\boldsymbol{A}$, which is a mathematical object, is related to the magnetic field $\boldsymbol{B} = \boldsymbol{\nabla} \times \boldsymbol{A}$, we can define another quantity in terms of the connection of Berry that is invariably tailored. For this, let us now consider that the adiabatic process discussed earlier is cyclic along a path γ, so equation 4 becomes:

$$\Delta\phi_n = \oint_\gamma \boldsymbol{A}_n(\boldsymbol{R}) \cdot d\boldsymbol{R} - \frac{1}{\hbar}\oint_\gamma E_n[\boldsymbol{R}(t')]dt' = \oint_\gamma \boldsymbol{A}_n(\boldsymbol{R}) \cdot d\boldsymbol{R} = \Phi_\gamma \quad (5)$$

Here the dynamic phase becomes zero trivially. Now, involking Stokes theorem, we can transform the line integral of equation 5 into an integral of the surface Γ associated with the contour γ, such as:

$$\Phi_\gamma = \oint_\gamma \boldsymbol{A}_n(\boldsymbol{R}) \cdot d\boldsymbol{R} = \iint_\Gamma \boldsymbol{\nabla}_R \times \boldsymbol{A}_n(\boldsymbol{R}) \cdot d\boldsymbol{s} = \iint_\Gamma \boldsymbol{F}_n(\boldsymbol{R}) \cdot d\boldsymbol{s} = \Phi_\Gamma, \quad (6)$$

where $\boldsymbol{F}_n(\boldsymbol{R}) = \boldsymbol{\nabla}_R \times \boldsymbol{A}_n(\boldsymbol{R})$ is know as the Berry curvature and is invariant under gauge transformations. We associate the Berry flux Φ_Γ through the surface Γ with Berry phase Φ_γ in around the contour γ. The curvature being gauge invariant has a physical reality extremely interesting that connects mathematics and physics in a very elegant way as we will see shortly.

The main reason that allows this connection is called Chern's theorem [74], this theorem affims that the Berry flux Φ_Γ across any two-dimensional manifold Γ is quantized by units of 2π, that means:

$$\iint_{\Gamma} \boldsymbol{F}_n(\boldsymbol{R}) \cdot d\boldsymbol{s} = 2\pi C \rightarrow C = \frac{1}{2\pi} \iint_{\Gamma} \boldsymbol{F}_n(\boldsymbol{R}) \cdot d\boldsymbol{s} = \frac{\Phi_{\Gamma}}{2\pi}, \tag{7}$$

where $C \in Z$. We know the integer C as the Chern number of surfaces Γ and it can be shown that this is the topological invariant associated with the variety of states $|\Psi_n[\boldsymbol{R}(t')]\rangle$ defined under this surface.

The importance of this invariant in Physics came in 1982, two years after the QHE experiments. Thouless, Khomoto, Nighingale and Nijs showed that the transverse conductivity of an QHE-like system can be written as [75], [76]:

$$\sigma_H = \frac{e^2}{\hbar} \sum_n \left[\frac{1}{2\pi} \int_{BZ} \boldsymbol{F}_n(\boldsymbol{k}) \cdot d\boldsymbol{k} \right] = \frac{e^2}{\hbar} \sum_n C_n, \tag{8}$$

where the sum is performed under the occupied bands showed by the index n. Furthemore the authors also showed that the Berry curvature integral of equation 8 is non-zero, this implies that the system in question has $C \neq 0$ which makes it different from trivial insulating systems known until then, which would have $C = 0$. It was also the first time that a connection between a completely geometric object derived from topology studies and a physical observable was made. For this reason, is also known the Chern number C in the literature as the TKNN index, in honor of the four authors.

In order to clarify the difference between systems with invariants in different topologies, let us use a classic example. In figure 6 can be observed how it is possible to deform continuously and smoothly a mug on a donut. This deformation is possible because both varieties have the same number of "holes", and we associate to them a topological invariant $C = 1$ known as genus, which is derived from the Gauss-Bonnet theorem [77] and classifies different surfaces by its topology. It is said that the mug and the donut to be a topologically equivalent. It would not be possible, for example, to deform a sphere, which has $C = 0$, in the same donut as this would imply breaking its surface, which violates the softly deformation requirement.

It can apply this same idea of deformation in quantum mechanics when we talk about Hamiltonians. If we associate a so-called trivial insulator with a Hamiltonian $H_A(\lambda)$ parametrized by λ, and for a topological insulator a Hamiltonian $H_B(\lambda)$, we will see in the next sub-section that it is not possible to perform an adiabatic transformation in λ, which takes $H_A(\lambda)$

to $H_B(\lambda)$ without a gap closure (or phase transitions), because both have different topological invariant values.

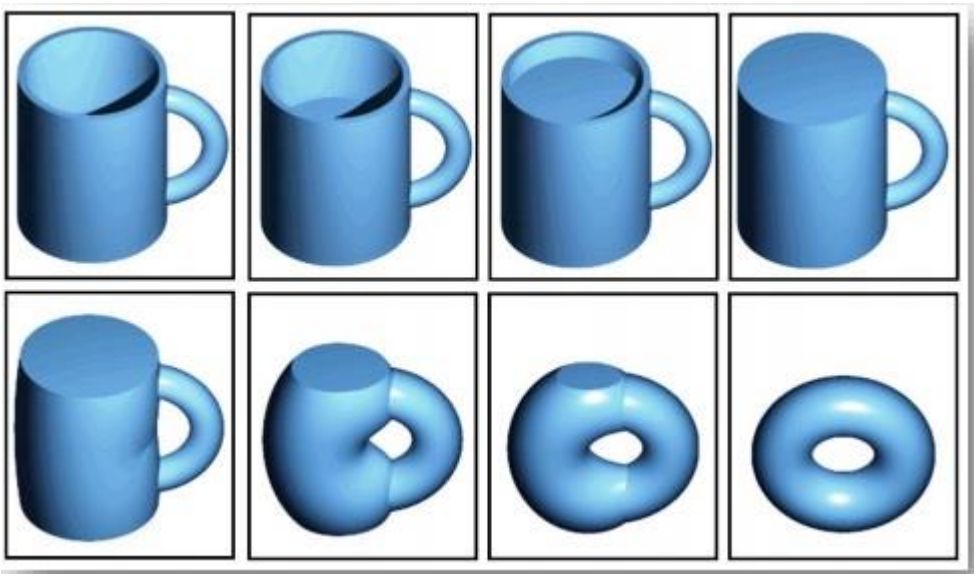

Figure 6: Comparison between a cup and a donut as being equal in topological language [78].

2.3.3 Spin Quantum Hall Effect or 2D Topological Insulators

In 2004, a new state of matter, as well as the Quantum Hall Effect that also displays topological order, were discovered. This new state of matter was first predicted to occur in two-dimensional (2D) quantum wells in 2006 [79], [80]. In 2007, it was observed experimentally in quantum wells of HgTe/CdTe [81].

All insulating states found in nature that preserve the symmetry of temporal inversion and have a non-degenerate ground state can be classified in two topologically distinct classes. We associate these classes with the topological invariante Z_2 (group of two integer elements 0 and 1, where 0 represents trivial insulator, like vacuum and 1 is non-trivial) [82].

The mechanism behind the 2D topological insulators is the strong spin-orbit coupling (SOC). It leads to a band inversion which breaks down the degeneracy of the atomic levels creating edge states that are spin polarized.

To better understand this new topological state, consider systems with spin ½ particles. We denote (TR) for time reversal and (TRS) for time reversal symmetry. The time reversal operator Θ has the following properties:

$$\Theta^{\dagger}\Theta = 1, \tag{9}$$

$$\Theta^{\dagger}\vec{r}\Theta = \vec{r}, \tag{10}$$

$$\Theta^{\dagger}\vec{p}\Theta = \Theta^{\dagger}m\frac{d\vec{r}}{dt}\Theta = -m\frac{d\vec{r}}{dt}, \tag{11}$$

$$\Theta^{\dagger}\vec{L}\Theta = \Theta^{\dagger}(\vec{r}\times\vec{p})\Theta = (\vec{r}\times -\vec{p}) = -\vec{L}, \tag{12}$$

where $\vec{r}$, $\vec{p}$ and $\vec{L}$ are the position, momentum and angular momentum, respectively. Trivially property of angular momentum expands to spin. Disregarding spin, the operator TR is simply the conjugation operator, K. Thus, if $\Psi(\vec{r},t)$ is a wavefunction, we have:

$$\Theta^{\dagger}\Psi(\vec{r},t)\Theta = \Psi^{*}(\vec{r},t). \tag{13}$$

Considering spin ½, the TR operator has to invert the spin, so it has the form $\Theta = -i\sigma_i K$, where σ_i is the Pauli matrices, and it transforms as $\Theta^{\dagger}\sigma_i\Theta = -\sigma_i$. To have a time reversal symmetry is to be invariant by the operator $\Theta([H,\Theta]) = 0$. Therefore, the Hamiltonian becomes:

$$H(-k) = \Theta H(k)\Theta^{-1}. \tag{14}$$

For any point (Γ_i) from Brillouin zone (BZ):

$$-\Gamma_i = \Gamma_i + n_i G_i, \tag{15}$$

where n is 0 or 1 and $\vec{G}$ is a vector of reciprocal lattice. Then the system satisfies the condition $H(-\Gamma_i) = H(\Gamma_i)$ and, therefore, has time reversal symmetry, these points will always be degenerate, as they share the same self-energy. With a square lattice, there are 4 points that satisfy this condition. For a spin ½ system, this invariance implies that there are a pair number of degenerate states, this means that the bands cross. A pair of these bands is called Kramers pairs. Whenever there are these pairs and they are gap-separeted from other pairs, one can define a topological invariant associated [78], [82].

Consider a band structure of the edge of a two-dimensional topological insulator as a function of a crystalline moment along the edge. As the system Hamiltonian is invariant under time reversal due to spin-orbit coupling, the Kramers theorem's guarantees that, for certain points in the BZ, there will be states that are degenerates. As there are edge states, there will be points where these states will be degenerate, the states referring to the up and down spins will be equal at these points, called Dirac points [78], [82].

Spin Quantum Hall Effect (SQHE) can be seen as two copies of the QHE, where the states with opposite spins counter-propagate at the edge of the material. As in the QHE, in regions where the topological invariant changes, as at the interface between the SQHE and the vaccum, there are metallic states, seen in figure 7.

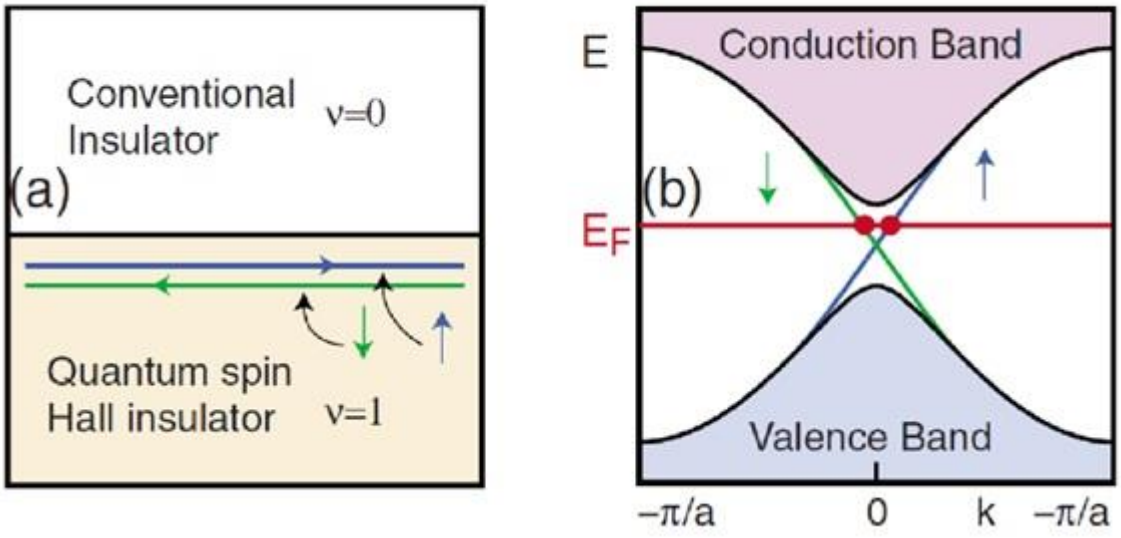

Figure 7: SQHE edge states. In (a) interface between an SQHE that has $\nu = 1$ and the conventional insulator $\nu = 1$, where ν is the Z_2 topological invariant. There are metallic edge states that are spins polarized, particles with different up and down components of spin propagating in opposite directions, the two propagation "channels" being connected by the time reversal symmetry. In (b) a schematic of the band structure it shown where the material bulk and spin polarized edge metallic states are localized [78].

Trivial conductors have electrons with spin up and down propagating in both directions and are fagile, since states are susceptible to Anderson localization, even in the presence of a weak disorder. In contrast to this, in SQHE edge states cannot be localized in the presence of a strong disorder because of the time reversal symmetry, as long as this impurity does not have a magnetic character [78], [82].

2.3.4 3D Topological Insulators

The three-dimensional topological insulators (3D-TIs) also present metallic surface states protected by time-reversal symmetry. The $Bi_{1-x}Sb_x$ was the first material to exhibit a topological order of a 3D-TI. Subsequently, the second generation, composed by Bi_2Se_3, Bi_2Te_3 and Sb_2Te_3, proved to be excellent 3D-TIs, figure 8. They exhibit strong spin-orbit couplings and have topological order at room temperature [39], [83].

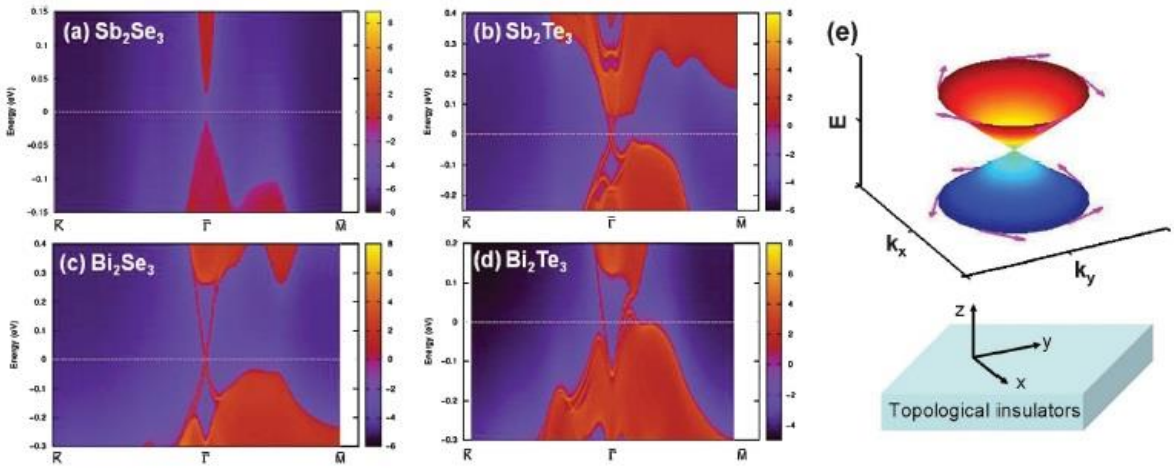

Figure 8: Energy dispersion near the Γ point, polarization and helical texture of the spins on the surface of the 3D-TI. (a): Dispersion of a trivial insulating compound for comparison. (b)-(d): Energy spectrum of the second-generation 3D-TI. Only a Dirac cone. (e): Polarization of the spins at the top of the surface of a 3D-TI [72].

Similar to $HgTe/CdTe$ quantum wells, the strong spin-orbit interacion induces a quantum mechanics phase transition in the above compounds, causing the band inversion at Γ point. This occurs when the parameter λ in the term associated with the spin-orbit interaction of the Hamiltonian ($\lambda\vec{L}\cdot\vec{S}$, where $\vec{L}$ and $\vec{S}$ are the orbital and spin angular moments respectively) is greater than a critical value, $\lambda > \lambda_c$. This process of parity inversion of electronic levels leads to a formation of massless Dirac fermion-like surface states in the compounds of second-generation [72], [83], [84].

This $(Bi, Sb)_2(Te, Se)_3$ family has a rhombohedral crystal structure of $R\bar{3}m$ phase. The system has a unit cell of five atomic layers, which belong to three-layer groups, also containing

five atoms called Quintuple Layers (QLs), as seen in figure 9. The links between the QLs are very weak due to Van der Walls interactions.

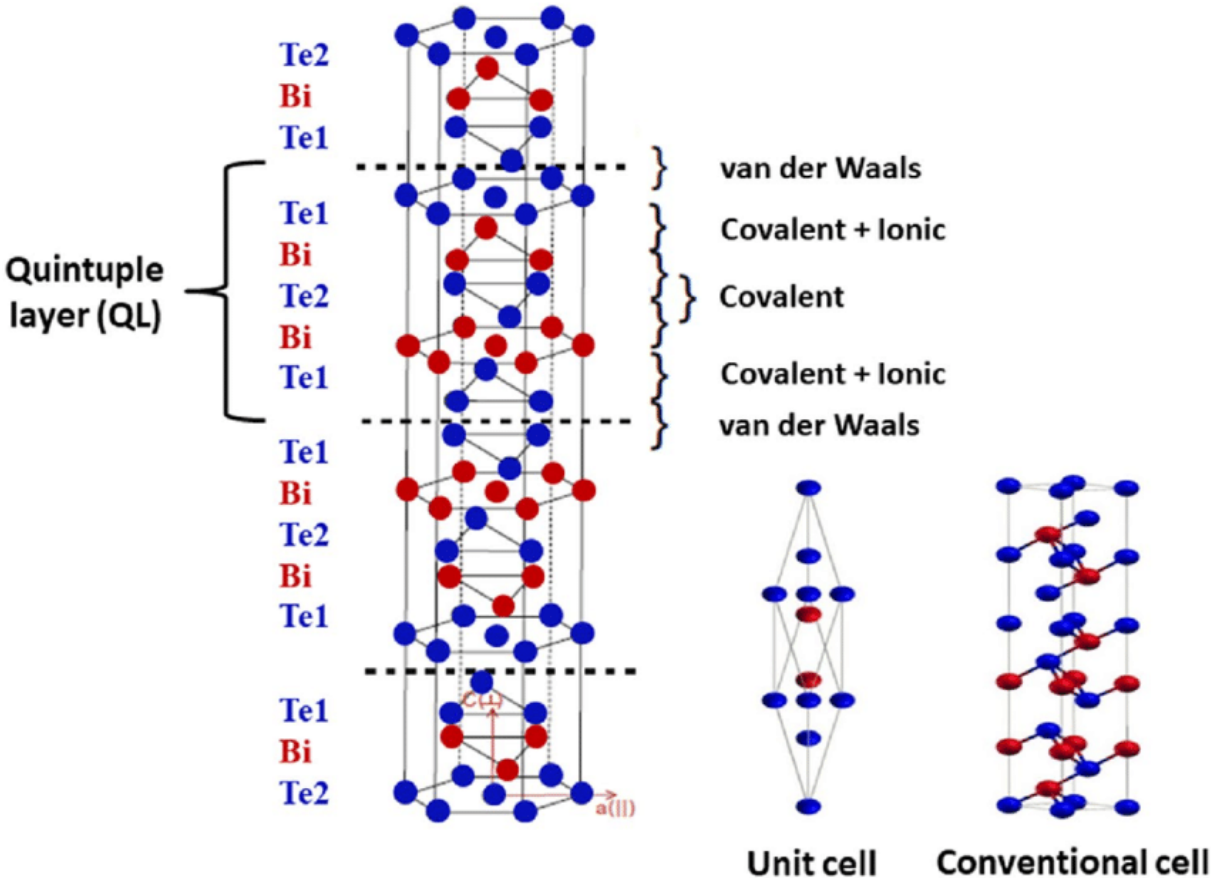

Figure 9: Crystal structure of Bi_2Te_3. On the right, rhombohedral unit cell and hexagonal conventional cell (bismuth atoms are represented in red, tellurium atoms in blue) [85].

2.3.5 Hexagonal Warping

The Bi_2Te_3 has a snowflake-pattern at Fermi surface. This pattern is explained by a hexagonal warping term that appears in the surface Hamiltonian using the $\boldsymbol{k} \cdot \boldsymbol{p}$ theory. The strength of hexagonal warping is characterized by a single parameter, which is extracted from the size of the Fermi surface. Using the $\boldsymbol{k} \cdot \boldsymbol{p}$ theory, the lowest order in k of the surface Hamiltonian is $H_0 = v_F(k_x\sigma_y - k_y\sigma_x)$, which describes an isotropic 2D Dirac fermion [86]. The form of H_0 is strictly fixed by symmetry. The Fermi surface of H_0 at any Fermi energy is a circle. However, the Fermi surface observed in Angle-resolved Photoemission Spectroscopy is noncircular, but snowflake-like [87]. This observation can be explained by higher orders

terms in $\boldsymbol{k}\cdot\boldsymbol{p}$ Hamiltonian $H(\boldsymbol{k})$ that breaks the emerging $U(1)$ rotational symmetry of H_0. The Hamiltonian up to third order in $\boldsymbol{k}$ being invariant under time-reversal symmetry is:

$$H(\boldsymbol{k}) = E_0(k) + v_{\boldsymbol{k}}\left(k_x\sigma_y - k_y\sigma_x\right) + \frac{\lambda}{2}(k_+^3 - k_-^3)\sigma_z, \tag{16}$$

where, $E_0 = k^2/(2m^*)$, $k_\pm = k_x \pm ik_y$ and $\sigma_\pm = \sigma_x \pm i\sigma_y$. Where m^* is the effective mass and v_k is the particle velocity at a specific k point. The last term in (16), which is called H_w, is most important. Unlike the other terms, H_w is only invariant under threefold rotation (as the Bi_2Te_3 crystal structure does) and therefore is solely responsible for the hexagonal distortion of the otherwise circular Fermi surface [86]. The surface band dispersion of $H(\boldsymbol{k})$ is:

$$E_\pm(\boldsymbol{k}) = E_0(k) \pm \sqrt{v_k^2k^2 + \lambda^2k^6\,cos^2(3\theta)}. \tag{17}$$

Here $E_\pm$ denote the energy of upper and lower band, and θ is the azimuth angle of momentum $\boldsymbol{k}$ with respect to the x axis (ΓK). Although the Hamiltonian H is threefold invariant, the band structure is sixfold symmetric under $\theta \to \theta + \frac{2\pi}{6}$ because of time-reversal symmetry. Different values of λ change the shape from a circular-like ($\lambda = 0$) to a snowflake-like ($\lambda > 0$), seen in figure 10.

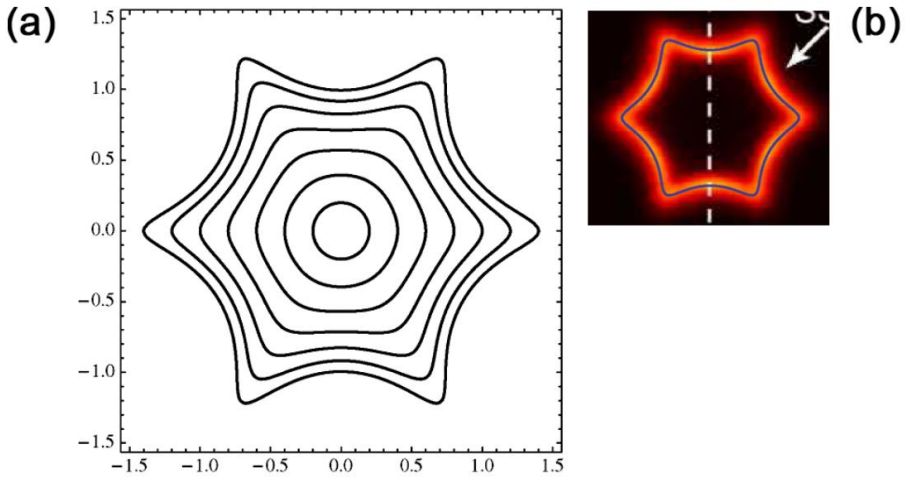

Figure 10: (a) Constant energy contour of $H(\boldsymbol{k})$. k_x and k_y axis are in the unit of $\sqrt{v/\lambda}$. (b) Snowflake pattern of Bi_2Te_3 Fermi surface comparing the model with the ARPES experiment [88].

2.4 Ferroeletricity

Ferroelectric materials are frequently compared to their ferromagnetic counterparts to facilitate the understand of ferroelectricity. The sole analogy lies in the switching behavior. In ferromagnets, magnetization can be altered by an external magnetic field, while in ferroelectrics polarization can be modified by an external electric field. A critical criterion to define ferroelectricity is the existence of electronic charge polarization (spontaneous polarization) induced within the unit cells of a material. Figure 11-(a) illustrates an exemple of spontaneous polarization in an oxide perovskite unit cell (ABO_3), where A-site cations occupy the cube's corners, the B-site cation resides at the body center, and the oxygen ions are positioned at the face centers.

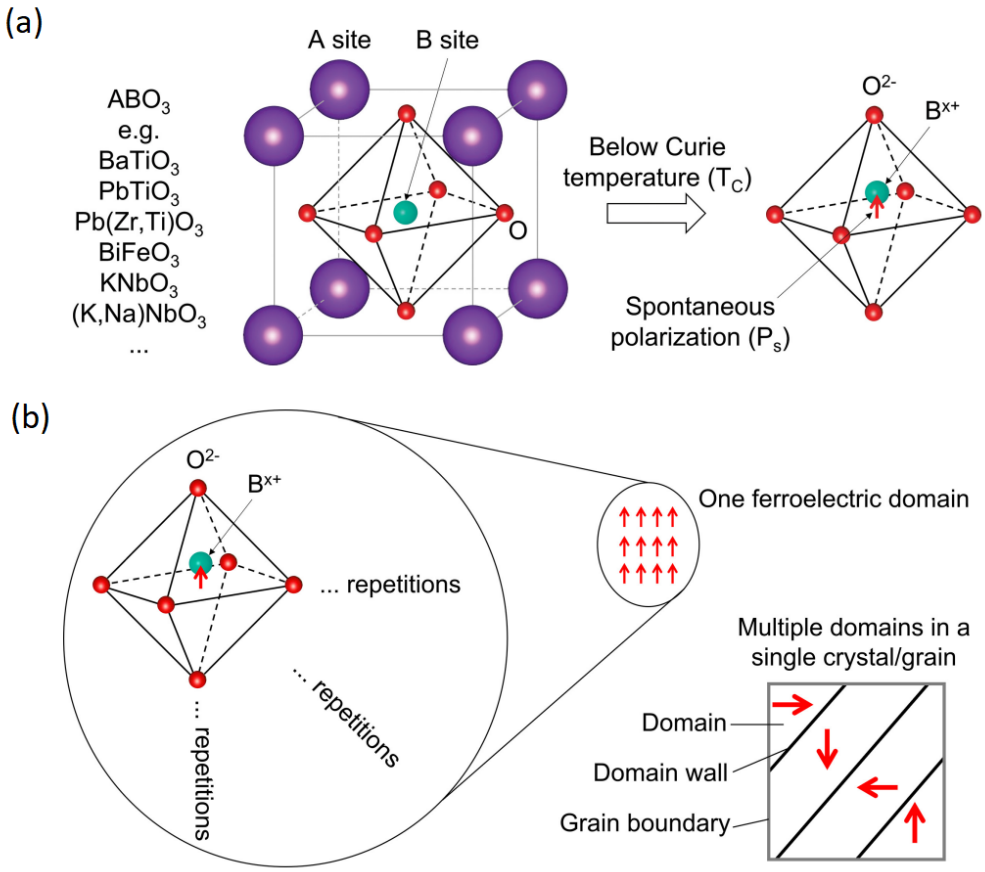

Figure 11: (a) Schematics of the oxide perovskite unit cell (ABO_3) and spontaneous polarization. Note that the A-site cations are not shown in the schematic on the right for a better

visual presentation. Note the displacement of the B atom. (b) Schematics of domains and domain walls[89].

Below the Curie temperature (T_C), the BO_6 octahedron undergoes a natural distortion, causing the B-site cation to shift away from the high-symmetry position. This separation of cation and anion centers results in spontaneous polarization. The example in Figure 11 illustrates the cubic (C) to tetragonal (T) phase transition. In the C phase, spontaneous polarization is prohibited, while in the T phase, spontaneous polarization occurs along the 001 direction, indicating an upward vertical orientation of the BO_6 octahedra, with the B-site cation shifting along this direction [89].

While multiple orientations are permited for spontaneous polarizations within a given phase, the practical transition of an established spontaneous polarization in an individual unit cell to an alternative direction remains predominant. In practice, the manipulation of ferroelectric polarization occurs through domains, primarily facilitated by the motion of domain walls. Figure 11-(b) schematically shows that a group of unit cells exhibiting spontaneous polarization in a congruent direction constitutes a domain. Within a given domain, the polarization direction is uniform, yet, in a crystalline structure, adjacent domains may exhibit polarizations oriented in different directions. The interface delineating two domains with disparate polarization orientations is termed a domain wall. Upon application of an external electric field, certain domains undergo reorientation, aligning themselfs in the direction of the electric field [89].

The extent of domain switching and domain wall motion depends upon the strength of the external electric field. Figure 12 presents a standard ferroelectric hysteresis loop (P–E loop) illustrating the relationship between the polarization of a ferroelectric material and the external electric field. In a non-polarized ferroelectric state, lacking a net polarization, domains are randomly oriented (point 0 in Figure 12). With the application of an electric field, domains begin to allign, and the greater the electric field, the more domains are allined (0→1 in Figure 12), culminating in saturation (point 1). At this stage, a majority of the domains have been permanently switched, leaving behind a remanent polarization (point 2) after the removal of the electric field (1→2). The remanent polarization can be erased by applying a negative electric field until the coercive field (2→3), restoring a zero net polarization (point 3). Further increase of the negative electric field (3→4) results in the attainment of saturation in the opposite

direction (point 4). The subsequent sequence (4→5→6) is a repetition along the other remanent polarization direction (point 5), reaching at the positive coercive field with yet another zero net polarization (point 6). The loop (1→6) replicates itself after the first cycle, and its shape is influenced by the frequency of the electric field as well as the material properties [89].

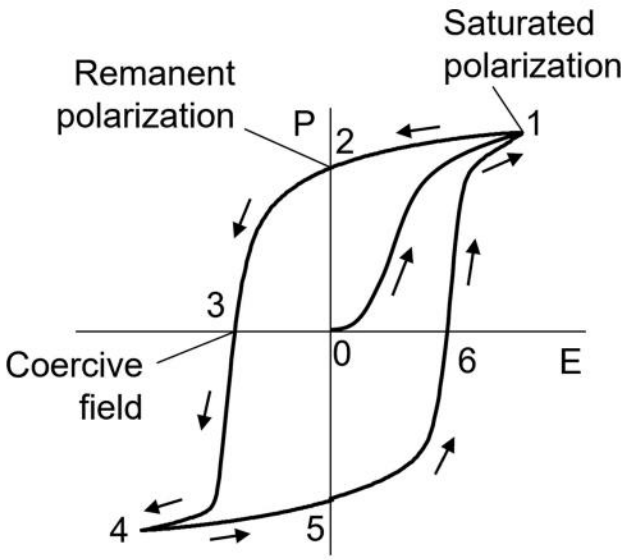

Figure 12: Example ferroelectric hysteresis loop (P–E loop). P is polarization [89].

3 Density Function Theory (DFT)

Among all the modern quantum theories that propose to treat problems of many bodies in a rigorous and efficient way, the Density Funcional Theory (DFT) is certainly one of the most important and popular, if the electron interactions are not strong inside the material. Featuring great versatility and flexibility, the DFT stands outin its huge range of applications, being used to study systems and physical properties such as superconductors [90], effects of including SOC [90], ionic liquids [91], properties of alloys [92], among others.

Significant result of the DFT is its ability to determine the electronic density of a system which carries all the information of the ground state. Pierre Hohenberg and Walter Kohn [93] defined the bases of the theory using two fundamental theorems.

3.1 The Many Body Problem

The proper treatment of quantum systems requires the construction of an operator Hamiltonian, which will carry important information about the physics of the system in question. For a system composed of N interacing electrons (indicated by the indices i and j) and M atomic nuclei (indicated by A and B), the Hamiltonian is given by:

$$H = T_e + T_n + V_{ee} + V_{nn} + V_{en}\,. \tag{18}$$

The kinectic energy of electrons and nuclei are, respectively:

$$T_e = -\sum_{i=1}^{N} \frac{1}{2m} P_i^2\,, \qquad T_n = -\sum_{A=1}^{M} \frac{1}{2M_A} P_A^2\,. \tag{19}$$

The Coulomb potentials of electron-electron repulsion, nuclei-nuclei repulsion and electron-nuclei repulsion are, respectively:

$$V_{ee} = -\sum_{i=1}^{N}\sum_{j>1}^{N} \frac{1}{r_{ij}}, \qquad V_{nn} = \sum_{A=1}^{M}\sum_{B>A}^{M} \frac{Z_A Z_B}{r_{AB}}, \qquad V_{en} = \sum_{i=1}^{N}\sum_{A=1}^{M} \frac{Z_A}{r_{iA}} \tag{20}$$

Given the above Hamiltonian, one can get the properties of the quantum system through the solution of the time-independent Schrödinger equation:

$$H\Psi\left(\vec{r}_1, \dots, \vec{r}_N, \vec{R}_1, \dots, \vec{R}_M\right) = E\Psi\left(\vec{r}_1, \dots, \vec{r}_N, \vec{R}_1, \dots, \vec{R}_M\right), \tag{21}$$

where the vectors $\vec{r}_i$ and $\vec{R}_A$ locate electrons and nuclei, respectively.

This formulation of the problem requires the determination of a function of 3(N+M) variables (not considering the spin degrees of freedom). As a way to reduce our problem, we can use a well-established approach to treat crystalline solids and molecules. It is called $Born - Oppenheimer\ Approximation$ [94], [95], which shows that we can treat the nuclear coordinates as slow variables. This is due to the large difference in mass between the massive nucleus and the electrons. We can decouple the motion of both and define the electronic Hamiltonian by:

$$H = T_e + V_{ee} + V_{ext}. \tag{22}$$

The Kinect energy of nuclei T_n is neglected within this approximation and the term V_{nm} is a constant because the nuclei are fixed in space. In the last term of equation 22, V_{ext}, we included the electron-nucleus interactions and any other contributions of external fields. The eigenvalue corresponding to the above Hamiltoninan is the electronic energy.

3.2 Functional Definition

For an arbitrary function $y = f(x)$, given a value (number) x, a mathematical object of this type returns another y value (number), that is, a function is a kind of rule or map that takes one number into another number. Similarly for a functional, which is usually defined in the literature with the notation $F[x]$, the variable x is actually a function, a functional is a map that takes a function in to a number. To illustrate this ideia, we can think of the following example: suppose a system which has an associated particle density $\rho(\boldsymbol{r})$, for such a system, we know that the total number of particles N is given by:

$$N[\rho(\boldsymbol{r})] = \int \rho(\boldsymbol{r}) d^3r, \tag{23}$$

which means that, given a particle density function, the functional returns a real number N.

3.3 Hohenberg-Kohn Theorems

According to the theorems of Hohenberg and Kohn [93]the Schrödinger equation of N electrons, whose basic variable was the wavefunction with $3N$ degrees of freedom, can have as new variable, the electron density, with only 3 degrees of freedom. Two theorems are fundamentals to the density functional theory:

Theorem 1 – *The external potential V_{ext} sensed by the electrons is a unique functional of the electron density $\rho(\vec{r})$.*

Theorem 2 – *The energy of ground state E_0 is minimal for the density $\rho_0(\vec{r})$ of the ground state.*

Given the ground state electron density $\rho_0(\vec{r})$, it is possible to calculate all the physical observables. Now we can write the energy as a functional of $\rho(\vec{r})$.

$$E[\rho] = \min_{\Psi\to\rho}\langle\Psi|T_e + V_{ee} + V_{en} + V_{nn}|\Psi\rangle,$$

$$E[\rho] = \langle\Psi|T_e + V_{ee}|\Psi\rangle + \int \rho(\vec{r})V_{ext}(\vec{r})d^3r,$$

$$E[\rho] = F[\rho] + V_{ext}[\rho]. \quad (24)$$

To use these theorems, we have to get the analytic expressions of each functional described above. It is important to note that $F[\rho] = \langle\Psi|T_e + V_{ee}|\Psi\rangle$ is a universal functional and has the same form for any system. But, $V_{ext}[\rho] = \int \rho(\vec{r})V_{ext}(\vec{r})d^3r$ depends on the geometry of the system.

3.4 Kohn-Sham Equations

To determine the energy as a functional of density, we will use the Kohn-Sham scheme [96], in which we map the system of interacting N electrons in a system of N non-interacting electrons with the same electron density. Writing the energy and all its operators as functionals of ρ, we have that:

$$\langle\Psi|H_e|\Psi\rangle \to E(\rho) = T[\rho] + V_{Ne}[\rho] + V_{NN}[\rho] + V_{ee}[\rho] = T[\rho] + U[\rho] + V_{ext}[\rho], \quad (25)$$

where, $U[\rho] = V_{ee}[\rho]$ and $V_{ext}[\rho] = V_{Ne}[\rho] + V_{NN}[\rho]$.

So far everything is accurate (within the Born-Oppenheimer approximation). To have explicit formulas of the funcionals, we write the kinetic energy operator as follows:

$$T[\rho] = T_s[\rho] + T_c[\rho] = \frac{\hbar^2}{2m}\sum_i^N \int \bar{\phi}_i(\vec{r})\nabla^2\phi_i(\vec{r})d^3r + T_c[\rho], \tag{26}$$

where $T_s[\rho]$ is the kinetic energy of a non-interacting system for which $\phi_i(\vec{r})$ are the one single-particle orbitals. Here, T_s is not an explicit functional of density, and $T_c[\rho]$ is a correlation term. In the same way, we write the potential energy in the form:

$$U[\rho] = U_H[\rho] + U_x[\rho] = -\frac{e^2}{2(r\pi\varepsilon_0)}\int d^3r \int d^3r' \frac{\rho(\vec{r})\rho(\vec{r}')}{|\vec{r}-\vec{r}'|} + U_x[\rho], \tag{27}$$

where, $U_H[\rho]$ is the term that describes the classical Couloumb interaction of the electronic cloud, described by Hartree's theory. We can couple the exchange and correlation term on to unique functional, $E_{xc}[\rho] = T_c[\rho] + U_x[\rho]$, kown as the exchange-corralation term. Combining the equations 24, 25, 26 and 27, we find that

$$E[\rho] = T_s[\rho] + U_H[\rho] + V_{ext}[\rho] + E_{xc}[\rho]. \tag{28}$$

All contributions to exchange and correlation are included in the last term, $E_{xc}[\rho]$. According to the Variational theorem, taking the minimum of $E[\rho]$, with the constraint that the total number N of particles is fixed, according to $N = \int \rho(\vec{r})d^3r$, we may write:

$$\frac{\delta}{\delta\rho(\vec{r})} = \left[E[\rho] - \mu\left(\int \rho(\vec{r})d^3r - N\right)\right] = 0. \tag{29}$$

Here, the problem is reformulated in terms of the Lagrange functional and the Lagrange multiplier μ. Substituting $E[\rho]$ in expression 29 we get:

$$\frac{\delta E[\rho]}{\delta\rho(\vec{r})} = \frac{\delta T_s[\rho]}{\delta\rho(\vec{r})} + \frac{\delta U_H[\rho]}{\delta\rho(\vec{r})} + \frac{\delta TV_{ext}[\rho]}{\delta\rho(\vec{r})} + \frac{\delta E_{xc}[\rho]}{\delta\rho(\vec{r})} = \mu,$$

$$\frac{\delta T_s[\rho]}{\delta\rho(\vec{r})} + v_{ext}(\vec{r}) + v_H(\vec{r}) + v_{xc}(\vec{r}) = \mu. \tag{30}$$

The last three terms on the left side of equation 30 can be seen as potentials. The Kohn-Sham ideia is to introduce an auxialiary set of single particles states $\phi_i(\vec{r})$, so that thi system generates the same electron density as the many-body wavefuncion. Given the potential $v_s = v_{ext}(\vec{r}) + v_H(\vec{r}) + v_{xc}(\vec{r})$, we get the same density as the problem of interest, where now it is enough to solve the equation 31 for the non-interacting electrons.

$$\left[-\frac{\hbar^2\nabla^2}{2m}+v_s(\vec{r})\right]\phi_i(\vec{r})=e_i\phi_i(\vec{r}). \tag{31}$$

So, we can reproduce the density $\rho(\vec{r})$ by the equation:

$$\rho(\vec{r})=\sum_i^N f_i|\phi_i(\vec{r})|^2, \tag{32}$$

where f_i represent the orbital occupation. Remembering that $v_H(\vec{r})$ and $v_{xc}(\vec{r})$ depend on $\rho(\vec{r})$, which depends on the orbital $\phi_i(\vec{r})$ which depends on $v_s(\vec{r})$, the problem has to be solved self-consistently. Note that the Kohn-Sham equations takes the form:

$$\left[-\frac{\hbar^2\nabla^2}{2m}+v_{ext}(\vec{r})+v_{xc}(\vec{r})+\frac{e^2}{4\pi\varepsilon_0}\int\frac{\rho(\vec{r})}{|\vec{r}-\vec{r}'|}d^3r'\right]\phi_i(\vec{r})=e_i\phi_i(\vec{r}). \tag{33}$$

When multiply on the left by $\overline{\psi_i}$, integrating into space coordinate and summing over all the orbitals we have:

$$\sum_i^N e_i=T_s[\rho]+\int v_{ext}\rho(\vec{r})d^3r+\frac{e^2}{4\pi\varepsilon_0}\int\int\frac{\rho(\vec{r})\rho(\vec{r}')}{|\vec{r}-\vec{r}'|}d^3r'd^3r=\int v_{xc}\rho(\vec{r})d^3r. \tag{34}$$

Comparing the equation 34 with 28, the total energy is:

$$E_0=\sum_i^N e_i-\frac{e^2}{8\pi\varepsilon_0}\int\int\frac{\rho(\vec{r})\rho(\vec{r}')}{|\vec{r}-\vec{r}'|}d^3r'd^3r-\int v_{xc}\rho_0(\vec{r})d^3r+E_{xc}[\rho_0]. \tag{35}$$

Numerical solutions of the Kohn-Sham equations depend on the choice of approximation for the exchange-correlation functional which will be discussed in the next section.

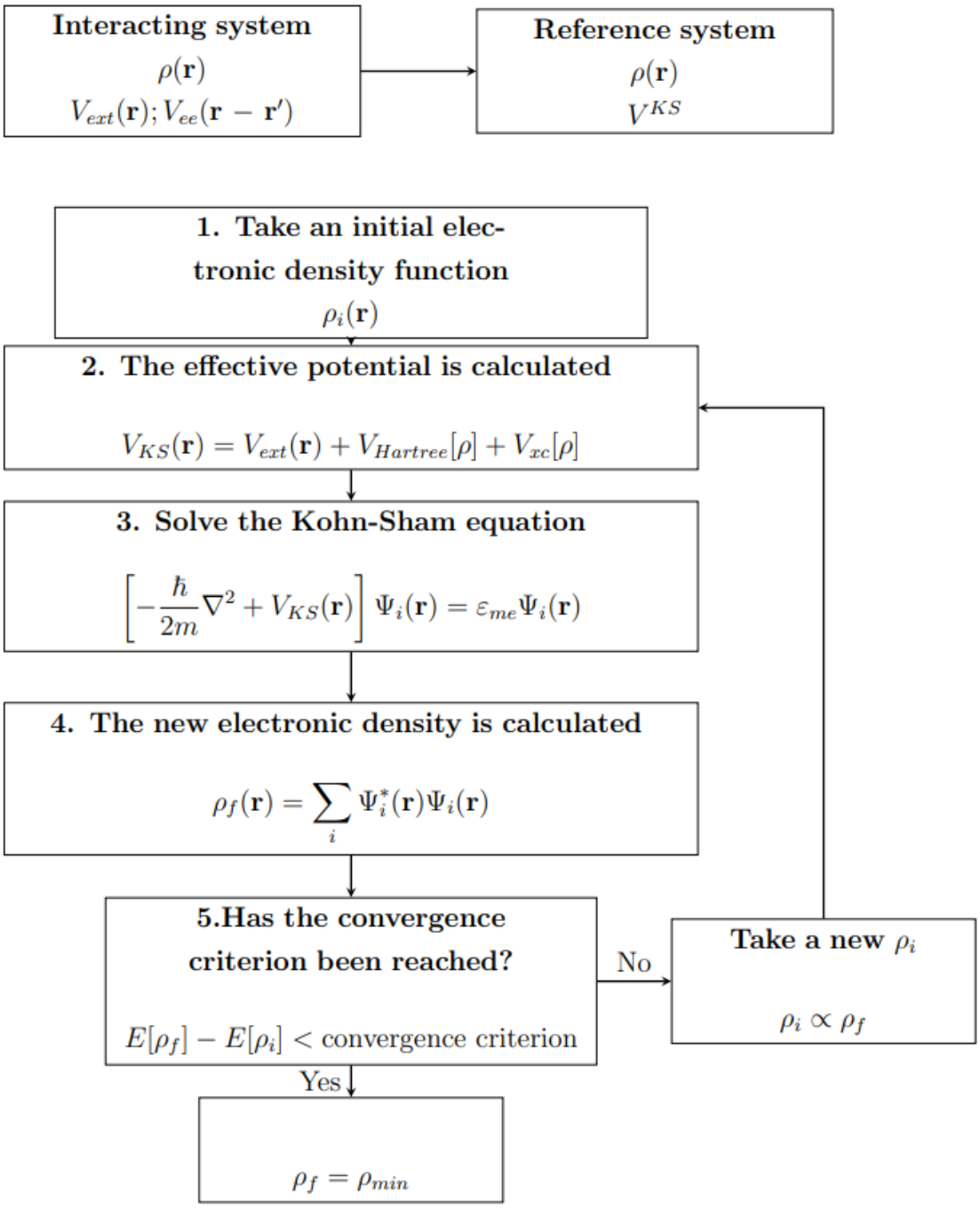

Figure 13: Schematic of the self-consistent calculation.

3.5 Functional Approximations for Funcional E_{xc}

As mentioned earlier, because of the complex nature of E_{xc}, it is necessary to construct sufficiently complete approximations so that it does not lose the information of important physical ingredients of the system. We are going to discuss some of the most used which can be found in the literature as the Local Spin Density Approximation (LSDA) and the Generalized Gradient Approximation (GGA).

3.5.1 LSDA Aproximation

The LSDA approximation is one of the simplest approximations we can use to handle the exchange-correlation functional in the DFT. The approach cousists in treating the electrons as a homogeneous gas, and in this limit the exchange-correlation functional has a strictly local character: it is assumed that for every point in space the exchange-correlation energy density is equal to that of a homogeneous electron gas with the same given density [93], so:

$$E_{xc}^{LSDA} = \int \rho(\vec{r})\varepsilon_{xc}^{hom}(\rho_{\uparrow}(\vec{r}), \rho_{\downarrow}(\vec{r}))dr = \int \rho(\vec{r})[\varepsilon_{x}^{hom} + \varepsilon_{c}^{hom}]dr, \qquad (36)$$

where $\rho_{\uparrow}(\vec{r})$ and $\rho_{\downarrow}(\vec{r})$ are the electronic density for spin up and down respectively. The parameterization is based on Monte Carlo simulations [97].

3.5.2 GGA Aproximation

The GGA approximation consists in assuming that the exchange-correlation functional depends not only on the density, but also on its gradient:

$$E_{xc}^{GGA} = \int \rho(\vec{r})\varepsilon_{xc}^{hom}(\rho_{\uparrow}(\vec{r}), \rho_{\downarrow}(\vec{r}), |\nabla\rho_{\uparrow}(\vec{r})|, |\nabla\rho_{\downarrow}(\vec{r})|, \dots)dr,$$

$$E_{xc}^{GGA} = \int \rho(\vec{r})\varepsilon_{x}^{hom}\big(\rho(\vec{r})\big)F_{xc}(\rho_{\uparrow}(\vec{r}), \rho_{\downarrow}(\vec{r}), |\nabla\rho_{\uparrow}(\vec{r})|, |\nabla\rho_{\downarrow}(\vec{r})|, \dots)dr, \qquad (37)$$

where F_{xc} is dimensionless [98]. There are many propositions for the F_{xc} function in the literature. The most commom are the parameterizations B88, proposed by Becke [99], and PBE, proposed by Perdew, Burke and Enzerhof [100].

3.6 Pseudopotentials

The concept of pseudopotential is extremely commom in DFT and brings many benefits to electronic structure calculations such as reduction of the number of functions in the basis set used for the construction of Hilbert space, reduction of the number of electrons in the system and inclusion of relativistic effects without the need to solve the Dirac equation. The ideia behind this concept is to replace the strong potential for interaction between nuclei and core electrons and its effects by an effective potential that acts only on valence electrons.

Therefore, it replaces the external potential V_{ext} of the Kohn-Sham equantion 33 by a pseudopotential $V_{PP}[\rho]$. There are many ways to generate these pseudopotentials and this remains a topic of research to this day[101]. There are also many classifications in the literature, such as conserved norm[102], ultrasoft[103], among others.

3.7 Periodic System and Bloch Theorem

In solid state physics, we say that crystals are defined by a Bravais lattice and an atomic basis associated to each point of the lattice. The Bravais lattice is a system of infinite points with regular arrangement along space. The lattice is defined by the translational symmetry: given any two lattice points $\vec{r}$ and $\vec{r}'$, there will be a translation vector from one to the other, as shown in the following equation:

$$\vec{r} = \vec{r}' + \vec{R}_n, \qquad \vec{R}_n = \sum_{i=1,2,3} l_{ni}\vec{a}_i\,, \tag{38}$$

where l_{ni} are integer. Since the ions in a perfect crystal are periodically positioned, the potential has the same periodicity, that is:

$$V(\vec{r} + \vec{R}_n) = V(\vec{R}). \tag{39}$$

Even knowing that the electronic problem in a solid is, in principle, a problem of many electrons, with the Hamiltonian including electron-electron and electron-nuclei interactions, we may formulate the problem in terms of single-particle states acted on by a periodic potential:

$$\left[-\frac{\hbar^2\nabla^2}{2m}+v_s(\vec{r})\right]\phi_{\vec{k}}(\vec{r})=e_i\phi_{\vec{k}}(\vec{r}). \tag{40}$$

Bloch's theorem establishes that an eigenfuncion $\phi_{\vec{k}}(\vec{r})$ of the electronic Hamiltonian must have the form of a plane wave times a function with the periodicity of the lattice:

$$\phi_{\vec{k}}(\vec{r})=\sum e^{i\vec{k}\cdot\vec{r}}u_{\vec{k}}(\vec{r}), \qquad u_{n\vec{k}}\left(\vec{r}+\vec{R}_n\right)=u_{n\vec{k}}(\vec{r}). \tag{41}$$

3.8 Basis Functions

3.8.1 Plane Wave Method

The problem of solving the Schrödinger equation for periodic systems has been of interest since the beginning of quantum mechanics. A possible choice of basis set is based on plane waves. Using this scheme, the function $u_{n\vec{k}}(\vec{r})$ can be expanded as plane waves $\phi_{\vec{k}}(\vec{r})=\sum_{\vec{G}}C_{\vec{k}+\vec{G}}e^{i(\vec{k}+\vec{G})\cdot\vec{r}}$, in which $\vec{G}_m=\sum_i g_{mi}\vec{b}_i$ are reciprocal lattice vector written in terms of the reciprocal vectors $\vec{b}_i$. Using equation 40 we have:

$$\left[-\frac{\hbar^2\nabla^2}{2m}+v_s(\vec{r})\right]\sum_{\vec{G}}C_{\vec{k}+\vec{G}}e^{i(\vec{k}+\vec{G})\cdot\vec{r}}=e_i\sum_{\vec{G}}C_{\vec{k}+\vec{G}}e^{i(\vec{k}+\vec{G})\cdot\vec{r}}. \tag{42}$$

Now multiplying the equation 42 in the left by $e^{-i(\vec{k}+\vec{G})\cdot\vec{r}}$, introducing the expansion for the potential and integrating in the first Brillouin zone, we have:

$$\left[-\frac{\hbar^2}{2m}\left(\vec{k}+\vec{G}\right)^2+e_{n\vec{k}}\right]C_{\vec{k}+\vec{G}}+\sum_{\vec{G}}V^S_{\vec{G}-\vec{G}'}C_{\vec{k}+\vec{G}}=0, \tag{43}$$

with the coefficients in the potential expansion given by:

$$V^S_{\vec{G}-\vec{G}'}=\int_{BZ}v_s e^{i(\vec{G}-\vec{G}')\cdot\vec{r}}dv. \tag{44}$$

The plane wave basis set has some advantages, since the convergence of the calculation can be controlled with a single parameter, the number of plane waves. The parameter cutoff energy, is given in electron-volt and is associated with the plane wave with the highest energy.

The calculation, therefore, includes all plane wave with kinetic energies less than the cutoff, which means $\left|\vec{G}+\vec{k}\right| < \vec{G}_{cut}$, in which $E_{cut} = \frac{\hbar^2}{2m}\, G_{cut}^2$.

Quantum-Espresso (QE) [104] and Vienna Ab initio Simulation Package (VASP) [105] are open-source code which employs the plane wave method in the electronic structure calculations. Programmed in C and Fortran languages, its uses DFT as a base and the pseudopotential theory discussed here.

3.8.2 Localized Basis Method

Another scheme to describe Bloch functions is based on the choice of a localized basis set. This method is, for instance, implemented in the Spanish Iniciative for Electronic Simulations with Thousands of Atoms (SIESTA) [106]. It is one of the most used in theoretical description of nanostructures, since it is more suitable for large scale calculations. In this method, one be expands the eigenvalues of the electronic Hamitonian in functions of centered at each lattice site:

$$\phi_{n\vec{k}}(\vec{r}) = \sum_{\vec{R}_n} \omega_{n\vec{k}}\left(\vec{r}-\vec{R}_n\right) e^{i\vec{R}_n\cdot\vec{k}}, \tag{45}$$

in which the function $\omega_{n\vec{k}}(\vec{r}-\vec{R}_n)$ are known as Wannier functions. A natural choice of localized basis set is the one formed by atomic orbitals. Therefore, the Wannier funcions may be written in terms of these functions as:

$$\omega_{n\vec{k}}\left(\vec{r}-\vec{R}_n\right) = \sum_{\mu,\alpha} C_{i\mu}\left(\vec{k}\right)\chi\left(\vec{r}-\vec{\tau}_\alpha-\vec{R}_n\right). \tag{46}$$

Substituing into the Kohn-Sham Hamiltonian, we get:

$$\sum_{\mu\alpha}\left[\sum_{\vec{R}_n} e^{i\vec{R}_n\cdot\vec{k}}\left(\frac{\hbar^2}{2m}\nabla^2 + V_s(\vec{r})\right)\chi\left(\vec{r}-\vec{\tau}_\alpha-\vec{R}_n\right)\right] C_{i\mu}\left(\vec{k}\right)$$

$$= e_i\left(\vec{k}\right)\sum_{\mu\alpha}\sum_{\vec{R}_n} e^{i\vec{R}_n}\chi\left(\vec{r}-\vec{\tau}_\alpha-\vec{R}_n\right)C_{i\mu}(\vec{k})\,. \tag{47}$$

Multiplying the equation 47 by a basis function $\bar{\chi}(\vec{r}-\vec{\tau}_\alpha)$ and integrating in real space, we have:

$$\sum_{m\mu}\left[H_{\nu\mu}(\vec{k}) - e_{n\vec{k}}S_{\nu\mu}(\vec{k})\right]C_{i\mu}(\vec{k}) = 0, \tag{48}$$

in which:

$$H_{\nu\mu}(\vec{k}) = \sum_{\vec{R}_n,\alpha} e^{i\vec{R}_n\cdot\vec{k}}\left[\int \bar{\chi}_\nu(\vec{r}-\vec{\tau}_\alpha)H_{KS}\chi_\nu(\vec{r}-\vec{\tau}_\alpha-\vec{R}_n)\right]d^3r\,,$$

$$S_{\nu\mu}(\vec{k}) = \sum_{\vec{R}_n,\alpha} e^{i\vec{R}_n\cdot\vec{k}}\left[\int \bar{\chi}_\nu(\vec{r}-\vec{\tau}_\alpha)\chi_\nu(\vec{r}-\vec{\tau}_\alpha-\vec{R}_n)\right]d^3r\,. \tag{49}$$

Thus, we get the eigeinvalues and eigenvectors of equation 48. The advantages of the localized basis set rely on the fact of the simple physical interpretation within the Tight Binding scheme, and the need of a much smaller size (number of funcions) if compared to the plane wave case.

4 Experimental Techniques

4.1 Scanning Tunneling Microscopy (STM)

4.1.1 The Quantum Tunneling Effect

Scanning tunneling microcopy and spectroscopy (STM/STS) are interesting techniques to investigate not only nanostructures of two-dimensional materials like graphene, but also other novel materials such as topological insulators and semiconductors. Roher and Binning invented the scanning tunneling microscope in 1981 [107]. This technique is based on the quantum phenomenon of tunneling and allows the imaging of atomic and molecular structures through the variation of the tunneling current between an atomically thin conducting tip and the investigated sample. Together with microscopy, tunneling spectroscopy is used to obtain information about the electronic density of states of the sample as a function of the electron energy, which is done locally [108].

In quantum mechanics, the motion equation of an electron of mass m and energy E subjected to a potential $U(z)$ can be describe by the Schrödinger equation, whose time independent form is, in one dimension [109], [110]:

$$-\frac{\hbar^2}{2m}\frac{d^2}{dz^2}\psi(z) + U(z)\psi(z) = E\psi. \tag{50}$$

Considering $U(z)$ as:

$$U(z) = \begin{cases} 0, & z \leq 0 \\ U_0 > 0, & 0 \leq z \leq a \\ 0, & z \geq 0 \end{cases} . \tag{51}$$

The solution of equation 50 for each region will be:

$$\psi(z) = \begin{cases} A_1 e^{ikz} + B_1 e^{-ikz}, & z \leq 0 \\ Ce^{\kappa z} + De^{\kappa z}, & 0 \leq z \leq a \\ A_2 e^{ikz} + B_2 e^{-ikz}, & z \geq 0 \end{cases} , \tag{52}$$

for $E < U_0$, $k = \frac{\sqrt{2mE}}{\hbar}$ and $\kappa = \frac{\sqrt{2m(U_0-E)}}{\hbar}$. For $z \leq 0$ and $\geq a$ the solutions described above correspond to an electron moving with $p = \hbar k$. On the other hand, the great difference between classical and quantum theories lies on the region $0 \leq z \leq a$. Since the electron wavefunction has a finite value near the potential barrier, there is a certain probability that the electron tunnels through the barrier, figure 14. This quantum mechanical phenomenon is known as tunneling.

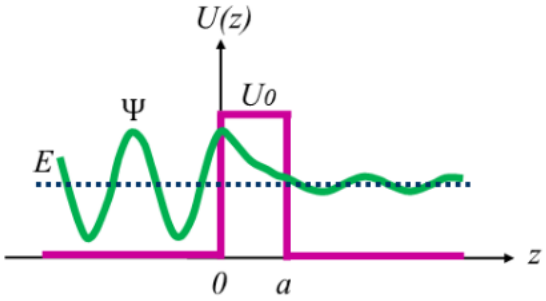

Figure 14: Representation of the wavefunction in quantum tunneling.

The constants A_1, A_2, B_1 and B_2 of the wavefunction in equations 52 can be determined by the continuity conditions of $\psi(z)$ and $\frac{d\psi(z)}{dz}$ for $z = 0$ and $z = a$. These constants give us information about the reflection and transmission coefficients, R and T, respectively. In the matricial form, the realation among these constants for $z = 0$ is [110]:

$$\begin{bmatrix} 1 & 1 \\ ik & -ik \end{bmatrix} \begin{bmatrix} A_1 \\ B_1 \end{bmatrix} = \begin{bmatrix} 1 & 1 \\ \kappa & -\kappa \end{bmatrix} \begin{bmatrix} C \\ D \end{bmatrix}, \tag{53}$$

and for $z = a$:

$$\begin{bmatrix} e^{\kappa a} & e^{-\kappa a} \\ \kappa e^{\kappa a} & \kappa e^{-\kappa a} \end{bmatrix} \begin{bmatrix} C \\ D \end{bmatrix} = \begin{bmatrix} e^{ika} & e^{-ika} \\ ike^{ika} & ike^{-ika} \end{bmatrix} \begin{bmatrix} A_2 \\ B_2 \end{bmatrix}. \tag{54}$$

The coefficients R and T can be obtained through the transference matrix P, which is defined as [110]:

$$\begin{bmatrix} A_1 \\ B_1 \end{bmatrix} = P \begin{bmatrix} A_2 \\ B_2 \end{bmatrix}. \tag{55}$$

Thus, the reflection and transmission coefficients are:

$$R = \left|\frac{B_1}{A_1}\right|^2 = \left|\frac{P_{21}}{P_{11}}\right|^2, \tag{56}$$

$$T = \left|\frac{A_2}{A_1}\right|^2 = \left|\frac{P_{22}}{P_{11}}\right|^2, \tag{57}$$

respectively, satisfying the condition $R + T = 1$. Explicitly, T can be written as:

$$T = \left[1 + \frac{U_0(sin^2\,\kappa a)}{4E(U_0 - E)}\right]^{-1}. \tag{58}$$

If $\kappa a \gg 1$, then T can be simplified as:

$$T = \left[\frac{4E(U_0 - E)}{U_0^2}\right] e^{-2\kappa a}. \tag{59}$$

Analyzing this expression, one sees that the transmission depends exponentially on the width of the potential barrier a. This was experimentally observed by Binng et all [111] and is what makes possible imaging the surface of different materials with high resolution.

4.1.2 Scanning Tunneling Microscope

The scanning tunneling microscope was the first microscope to be developed in the family of Scanning Probe Microscope (SPM) types. G. Binning and H. Roher got the first image in 1981 at IBM Zurich [108], [111]. In 1986, these researchers received the Nobel Prize in Physics for this invention. One of the most fundamental problems in surface physics is the determination of its structure and the STM operating mode allows the determination of the real lattice of the material in three demensions, including non-periodic systems. This technique is the one with the best resolution in the SPM, properly allowing the acquisition images with atomic scale resolution.

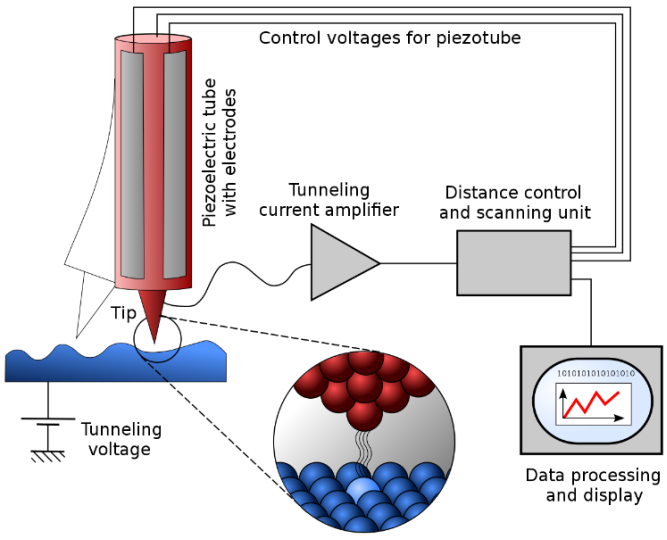

Figure 15: Schematic view of a STM microscope.

The STM basically works like this, an atomically thin conducting tip, usually made of W or $Pt-Ir$, is connected to piezoelectric motors in the x, y and z directions. These motors are made of piezoelectric materials, which can contract or expand depending on the application of a positive or negative bias voltage. This property makes this system able to scan the sample surface along the x and y directions, and also varies its z position, figure 15.

Once the tip and the sample are sufficiently close, but not in ohmic contact, i.e., in tunneling condition, it is applied a bias voltage between these two objects, so that a tunneling current will flow through the system. Assuming that the STM tip is grounded, V will be, therefore, the voltage applied to the sample. This means that if $V > 0$, for instance, the electron will tunnel from the occupied states of the tip to the unoccupied states of the sample. The tunneling current will be amplified and through a feedback system, it will control the distance between the tip and the sample surface in order to maintain the tunneling current fixed (constant current operation mode). If a tunneling current greater than the reference value is detected, the feedback system, connected to the piezoelectric motors, will drive the tip away from the sample surface, decreasing the tunneling current (remember that the transmission coefficient depends exponentially to the potential barrier width, which, in this case, is the tip-sample distance).

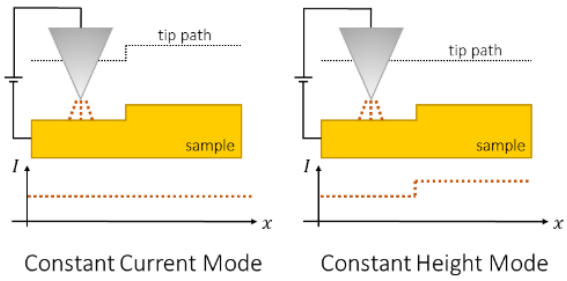

Figure 16: Operation modes of a STM. On the left panel one sees a constant current mode in which the tunneling current is kept constant and the distance between the tip and the sample varies. On the right panel the constant height mode is presented. In this mode of operation, the distance between the tip and the sample is kept constant, and the tunneling current varies.

The other option is when the tunneling current is smaller than the reference value, the piezoelectric motor will approach the STM tip towards the sample, increasing the tunneling current in order to keep it constant, see figure 16 on left panel. Because of this process, it will map the sample surface into topography images shown in a color-code that represents a combination between height and electronic variations, since the tunneling current also depends

on the sample density of states, as will be shown in the following section. In the constant height operation mode, it will fix the tip path during the entire sample surface scan. As a result, the tunneling current will vary according to the structure of the sample, figure 16 on right panel.

4.2 Scanning Tunneling Spectroscopy (STS)

We can construct the STM, as described in the article by J. Tersoff and D. R. Haman [112]. We are interested in the relationship between the tunneling current with the elements we know from theoretical simulations. The first order tunneling current in Bardeen formalism [113] is given by the equation:

$$I = \frac{2\pi e}{\hbar}\sum_{\mu\nu} f(E_\mu)[1 - f(E_\nu + eV)]\left|P_{\mu\nu}\right|^2 \delta(E_\mu - E_\nu), \tag{60}$$

where $f(E)$ is the Fermi Dirac function, V is the bias voltage applied, $P_{\mu\nu}$ is the tunneling matrix between the states ϕ_ν of the tip and ϕ_μ of the surface. We realize that ϕ_ν and ϕ_μ are not eigenstates of the same Hamiltonian. At the limit of low voltages and low temperatures, we can assume:

$$f(E_\mu)[1 - f(E_\nu + eV)] = C\delta(E_\mu - E_F), \tag{61}$$

where C is an unkown constant. Integrating over all energies, we have:

$$I = \frac{2\pi e^2 V}{\hbar}\sum_{\mu\nu}\left|P_{\mu\nu}\right|^2 \delta(E_\mu - E_F)\delta(E_\nu - E_F). \tag{62}$$

If we make the limit where the tip is replaced by a point of spherical potential (non-intrusive measure of the surface) the elements of the matrix have the form:

$$I \propto \sum_{\mu}\left|\psi_\mu(\vec{r}_0)\right|^2 \delta(E_\mu - E_F) = \rho(\vec{r}_0, E_F), \tag{63}$$

where $\vec{r}_0$ is the tip position (point). We see the current is proportional to the Local Density of States (LDOS) on the Fermi energy, and also on the tip position. Qualitatively, these concepts can be understood as follows: once a bias voltage, a negative one, for instance, is applied between the STM tip and the sample, the electrons will flow from the occupied states of the sample to the unoccupied states of the tip (considering that the tip is grounded). As can be seen in the scheme shown in figure 17, the density of sates of the sample, differently from that of the

tip, which can be taken as approximately constant, in general may have specific states for well-defined energies, which appaer as peaks, having different complex strucures that vary from sample to sample. Thus, the tunneling current will be mainly influenced by the sample DOS.

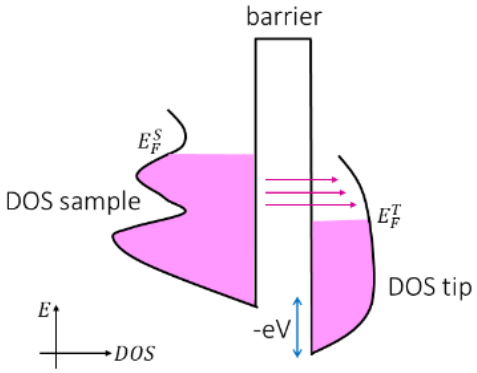

Figure 17: Schematic view of the tunneling between the STM tip and the sample. A negative bias voltage is applied to the sample and consequently the electrons will tunnel from the occupied states of the sample to the unoccupied states of the tip.

The STS technique basically consists on measuring the tunneling current at a single point of the sample defined by the STM tip position, which is atomically sharp, as a function of the electron energy. Therefore, the tunneling current can be rewritten as:

$$I \propto \int_0^{eV} LDOS_{tip}(E_F^T + \epsilon)\, LDOS_{sample}(E_F^S - eV + \epsilon) d\epsilon, \tag{64}$$

where the DOS of the tip and the sample is replaced by the LDOS. The derivative of the tunneling current as a function of the bias voltage will be [109]:

$$\frac{dI}{dV} \propto LDOS_{TIP}(E_F^T + eV) LDOS_{sample}(E_F^S). \tag{65}$$

Analyzing this expression, with the electrons tunneling from the occupied states of the sample to the unoccupied states of the tip at the energy $E_F^T + eV$ and to the local density of states of the sample at the Fermi level E_F^S.

Whether one can guarantee that the tip LDOS is approximally constant, then one can infer the sample LDOS (in fact, the tip LDOS, which depends on its material and its terminaton is not a constant, but in general it is a reasonable approximation). For a positibe bias, on the other hand, the derivative of the tunneling sample will be:

$$\frac{dI}{dV} \propto LDOS_{TIP}(E_F^T) LDOS_{sample}(E_F^S + eV). \tag{66}$$

Thus, one sees from the expressions 65 and 66 that depeding on the signal of the bias voltage, the occupied or unoccupied states of the sample may be highlighted in the tunneling spectrum. Therefore, the tunneling spectrum, $\frac{dI}{dV}$ or STS, give us information about the sample LDOS allowing the study of the electronic properties of different systems.

4.3 Angle Resolved PhotoEmission Spectroscopy (ARPES)

Angle-resolved photoemission spectroscopy (ARPES) stands as a major experimental technique in condensed matter physics, designed to unveil the intricate interplay of energies and momenta governing electrons within crystalline solids. Rooted in the principles of the photoelectric effect, ARPES involves the incidence of photons on a material's surface, liberating electrons in the process.

Through the analysis of energy and momentum profiles of emitted electrons, ARPES reveals the shape and dispersion of energy bands, alongside the locations of band gaps and Fermi surfaces. This information yields insights into fundamental physical properties of materials, including electronic conductivity, surface effects, optical properties and magnetic properties of materials (using Spin-ARPES). Analyzing measured energy bands permits the investigation of band renormalization and effective mass relation. Lineshape analysis allows for the extraction of single-particle self-energy related to each band. ARPES is extensively employed in materials science and condensed matter physics, contributing to the development of novel materials for electronic and optoelectronic devices. Additionally, it finds utility in surface chemistry studies, enabling the exploration of molecular interactions with surfaces and the electronic structure of thin films and interfaces.

4.3.1 Fundamentals

In an ARPES experiment, electrons undergo detection through an electron analyzer, a device capable of focusing an incoming electron beam onto a slit. Subsequently, employing the potential lens effect, the beam is deflected in a semi-circle and directed towards a detector. This detector captures the electrons at various positions upon their kinetic energies. This initial

setup closely follows the principles of Photoemission Spectroscopy (PES), a technique utilized for determining the binding energies of electrons within a material through the measurement of photoelectric effect intensity.

The distinct aspect of ARPES arises from the incorporation of an analyzer with angular acceptance in the slit and an area detector. This configuration enables the generation of an image representing the intensity of detected electrons as a function of both energy and angle. The angular component is intricately linked to the momentum of the electrons. However, it is imperative for the sample to be a single crystal with its alignment pre-determined through other methods. In ARPES, the detected intensity becomes associable with the electronic band structure of the material. Remarkably, the Fermi surface (FS) can be reconstructed through these measurements, shedding light on electronic properties of the studied material.

Following photoemission, the generation of a hole within the solid occurs. Theoretically, the formation of this photohole and its association with ARPES can be elucidated through the spectral function, alternatively termed the one-electron removal function. Nonetheless, merely measuring the electronic spectral function and Fermi surface of the sample by ARPES may prove insufficient. To comprehend the origins and mechanisms governing diverse ground states in quantum materials requires a theoretical modeling as well. Such materials often exhibit strong electron correlations, electron-phonon coupling, and various complex phenomena. In this context, the full potential of ARPES necessitates the integration of theoretical models and calculations.

4.3.1.1 The photoemission processes

ARPES operates as a photon-in, electron-out technique, rooted in the principles of the photoelectric effect. Monochromatized light, characterized by energy $h\nu$ and falling within the vaccum ultraviolet spectrum, impinges upon the sample. An electron within the material absorbs this incident light. When the energy surpasses a work function ϕ, the electron is emitted, and its kinetic energy can be expressed as in equation 67. This equation manifest the behavior of the photoelectric effect,

$$E_k = h\nu - \phi. \tag{67}$$

A more sophisticated theoretical description of the ARPES process incorporates the intricate many-body effects within the sample, which can be challenging to describe. Nonetheless, a comprehensive framework can be attained by employing quantum-mechanical perturbation theory to delineate the transition rate. In this regard, we contemplate a Hamiltonian that characterizes the electron within the solid along with the photon field, treating the latter as a weak time-dependent perturbation,

$$H = H_0 + V_{int}e^{-i\omega t}, \tag{68}$$

where H_0 is the unperturbed Hamiltonian with known eigein states and eigenvalues, and V_{int} is the photon field factor, given by:

$$V_{int} = -\frac{e}{mc}\boldsymbol{A}\cdot\boldsymbol{p}, \tag{69}$$

By introducing $\boldsymbol{A}$ as the potential vector and $\boldsymbol{p} = i\hbar\boldsymbol{\nabla}$ as the momentum operator, the expression for the photon field is derived under the consideration of a weak radiation field. This allows the elimination of the two-photon process term proportional to $\boldsymbol{A^2}$, and a specific gauge choice is adopted to remove the scalar potential φ: $\boldsymbol{\nabla}\cdot\boldsymbol{A} = 0$.

The assessment of the transition rate from an initial state with N electrons to a final state with N electrons can be conducted using Fermi's Golden Rule for a first-order perturbation, as delineated in equation 70 [114]. Here, Ψ_i^N represents the initial state, and Ψ_f^N the final N electron states. The first term captures the transition matrix elements from the initial to the final state, while the last term embodies the principle of energy conservation. In this context, the final state energy E_f^N equals the initial state energy E_i^N summed with the absorbed photon energy,

$$\omega_{i\to f} = \frac{2\pi}{\hbar}\left|\left\langle\Psi_f^N\middle|V_{int}\middle|\Psi_I^N\right\rangle\right|^2\delta\left(E_f^N - E_i^N - h\nu\right). \tag{70}$$

To incorporate surface properties, which differ fundamentally from bulk properties, the crystal Hamiltonian H_0 can become notably complex. Conceptualizing the photoemission process in this manner is referred to as the one-step model. An alternative model frequently employed to depict this process is the three-step model, as developed by Berglund and Spicer [115]. This model describes the photoemission process into three distinct and independent stages: bulk electron excitation through photon energy absorption, electron transport from bulk

to surface, and the release of the electron into the vacuum. The photoemission intensity is determined by the product of the probabilities of these three processes.

The second term can be characterized phenomenologically by the mean free path of the electron based on internal scattering. It is linked to the penetration depth of the ARPES technique, as bulk electrons beyond the mean free path will struggle to reach the sample surface. The third term can be described by the material surface energy barrier known as the inner potential V_0, comprising the work function ϕ and the difference E_0 between the kinetic energy of an electron inside the crystal and in the vacuum. Therefore, all information concerning the electronic structure is embedded in the first term.

Looking into the first step, ARPES intensity can be described by the transition rate from an initial to a final state, both with *N* electrons. However, the creation of the photohole introduces different Hamiltonians and eigenstates in the final state. To circumvent these complexities, the *sudden approximation* is employed. It involves considering that the electron departs from the surface immediately after excitation, allowing no time window for the relaxation process to interfere with the electron wavefunction. Consequently, instead of having an *N*-electron final state at the end of the first step, it will possess $N-1$ electron and a free electron with a wavefunction characterized by momentum $\boldsymbol{k}$. The approximation is represented by equations 71,

$$\begin{aligned} |\Psi_i^N\rangle &\approx \phi_i^{\boldsymbol{k}} |\Psi_i^{N-1}\rangle \\ |\Psi_f^N\rangle &\approx \phi_f^{\boldsymbol{k}} |\Psi_m^{N-1}\rangle \end{aligned} . \tag{71}$$

The final state, with $N-1$ electrons, can be excited to different eigenfunctions $|\Psi_m^{N-1}\rangle$, where m represents a set of quantum numbers encompassing all potential excitations of the final state [116]. This occurs after the electron is removed and returns to the initial electronic state. Consequently, the total transmission probability is expressed as the sum over m, considering all feasible excited states.

The initial state can be represented using the sudden approximation when contemplated within the Hartree-Fock framework. In this context, the total wave function can be articulated as a product of each electron wave function, signifying that, prior to absorbing the photon energy, the state can be factorized from the overall wave function. With this in mind, the transition matrix elements can be written as:

$$\begin{aligned}\langle \Psi_f^N | V_{int} | \Psi_i^N \rangle &= \sum_m \langle \phi_f^{\boldsymbol{k}} \Psi_m^{N-1} | V_{int} | \phi_i^{\boldsymbol{k}} \Psi_i^{N-1} \rangle, \\ &= \sum_m \langle \phi_f^{\boldsymbol{k}} | V_{int} | \phi_i^{\boldsymbol{k}} \rangle \langle \Psi_m^{N-1} | \Psi_i^{N-1} \rangle, \\ &= \sum_m M_{i,f}^{\boldsymbol{k}} C_{m,i}, \end{aligned} \tag{72}$$

where $M_{i,f}^{\boldsymbol{k}}$ is the one-electron transition matrix element and $C_{m,i}$ is the $N-1$ electron state overlap integral. To calculate the total ARPES intensity, we need to integrate $\omega_{i\to f}$ for all i,j and it will be a function of the detected kinetic energy and momentum according to equation 73,

$$I(\boldsymbol{k}, E_k) = \frac{2\pi}{\hbar} \sum_m \sum_{i,f} \left| M_{i,f}^{\boldsymbol{k}} \right|^2 \left| C_{m,i} \right|^2 \delta(E_k + E_m^{N-1} - E_i^N - h\nu). \tag{73}$$

E_k is the energy for a specific k-point. In the absence of electron-electron interactions, the removal of one electron would have no impact on the initial state, resulting in a $C_{m,i}$ coefficient equal to 1 for $m = i$ and zero otherwise. However, when considering electron interaction, the $C_{m,i}$ coefficient encompasses a spectrum of weights influencing the photoemission intensity. Consequently, the *one-electron spectral function* can be precisely defined by equation 74. This term encompasses all pertinent information regarding the electronic structure of the sample, representing the initial phase of the three-step model,

$$A(\boldsymbol{k}, E_k) = \sum_m \left| C_{m,i} \right|^2 \delta(E_k + E_m^{N-1} - E_i^N - h\nu). \tag{74}$$

However, the consideration of temperature effects is absent in equation 73 for the ARPES intensity. A streamlined approach to incorporate these effects is to introduce a Fermi-Dirac distribution function, denoted as $f(E,t) = \left(e^{\frac{E}{k_b T}} + 1\right)^{-1}$, thereby yielding the prevalent expression for ARPES intensity:

$$I(\boldsymbol{k}, E) = I_0(\boldsymbol{k}, \boldsymbol{A}) A(\boldsymbol{k}, E) f(E, T), \tag{75}$$

with E as the electron energy with respect to the Fermi level E_f and $I_0(\boldsymbol{k}, \boldsymbol{A}) \propto \sum_{i,f} \left| M_{i,f}^{\boldsymbol{k}} \right|^2$ as the transition matrix elements, which can be considered constant for a given geometry, but also affected by the polarization and orbital spatial dependencies.

It is imperative to emphasize that equation 75, representing the ARPES intensity, does not encompass experimental nuances such as finite energy and momentum resolution. While the model relies on the three-step model and sudden approximation of Fermi's golden rule for the transition probabilities, its scope is somewhat constrained by necessary simplifications. Nevertheless, this model serves as a foundation for interpreting the significance of the resultant ARPES spectra. For a rigorous quantitative analysis, beyond phenomenological models, calculations grounded in the one-step model may be imperative to facilitate a precise comparison between theoretical predictions and experimental observations

4.3.1.2 One-particle spectral function and self-energy

The expression given by equation 74 for the spectral function implies that in a non-interacting scenario ($C_{m,i} = 1$ for $m = i$ and 0 otherwise), the ARPES bands would manifest as perfectly sharp delta functions with no width. However, due to electron interactions, the actual ARPES spectra consistently exhibit characteristic broadening of the lines. In accordance to our formalism and under our approximation, addressing this broadening of band lines is best accomplished through the utilization of the Green function [117].

The spectral function defined in equation 74 is connected to the single-particle Green function by:

$$A(\boldsymbol{k}, E) = -\frac{1}{\pi} Im\big(G(\boldsymbol{k}, E)\big). \tag{76}$$

Mathematically, the Green function is formally defined as the solution to an inhomogeneous linear differential equation, resulting in a δ-type function. In a physical context, it serves to characterize the time-retarded response or propagation of an operator. The Green function can be expressed through an expansion of the operator eigenvalues. In the specific case of photoemission, the pertinent Green function is determined by the one-electron removal operator within the *N*-electron system previously elucidated. This Green function can be utilized to deduce the spectral function through an alternative method. Furthermore, to incorporate the effects of electron correlation, the Green function can be expressed in terms of the electron *self-energy* $\sum(\boldsymbol{k}, E)$:

$$G(\boldsymbol{k}, E) = \frac{1}{E - \epsilon_{\boldsymbol{k}} - \sum(\boldsymbol{k}, E)}, \tag{77}$$

where $\sum(\boldsymbol{k}, E)$ is defined as having a real part $\sum'(\boldsymbol{k}, E)$, related to the energy renormalization when compared with a non-interacting system, and an imaginary part $\sum''(\boldsymbol{k}, E)$, related to the photoemission lifetime [114]. $\epsilon_{\boldsymbol{k}}$ is the electron band energy at a given $\boldsymbol{k}$. From this, we can write the spectral function as:

$$A(\boldsymbol{k}, E) = -\frac{1}{\pi} \frac{\Sigma''}{(E - \epsilon_{\boldsymbol{k}} - \Sigma')^2 - \Sigma''^2}\,. \tag{78}$$

In accordance with the principle of energy conservation, a detected photoelectron will possess energy equivalent to its band energy augmented by a self-energy factor, particularly when considering electron correlations. Furthermore, assuming that self-energy components remain constant, the spectral function will adopt the shape of a Lorentzian distribution, characterized by a full width at half maximum (FWHM) related to $2\Sigma''$ and a center at $\epsilon_{\boldsymbol{k}} + \Sigma'$. The analytical derivation of these self-energy components is intricate, and under certain experimental conditions, an estimation may be practical. However, the complexity of these components underscores the significance of the energy and momentum resolutions, which, though overlooked thus far, are paramount as the resolution capability for line width is inherently bound by the constraints of experimental resolution.

To accommodate these factors and address temperature effects, it is imperative to multiply the spectral function by the Fermi-Dirac distribution, as per equation 73, and it convolves with a 2D Gaussian incorporating widths associated with energy and momentum resolutions. In experimental settings, obtaining the scattering rate Γ, linked to the imaginary part of the self-energy Σ'', requires the consideration of a renormalization factor Z [118], [119]:

$$\Gamma = -2Z\Sigma''. \tag{79}$$

With this in mind, we can rewrite the spectral function in terms of Γ, which is directly associated to the experimental FWHM:

$$A(\boldsymbol{k}, E) = \frac{1}{\pi} Z(\boldsymbol{k}, E) \frac{\frac{\Gamma(\boldsymbol{k},E)}{2}}{(E - \epsilon^*_{\boldsymbol{k}})^2 + \left(\frac{\Gamma(\boldsymbol{k},E)}{2}\right)^2}, \tag{80}$$

where $\epsilon^*_{\boldsymbol{k}}$ is the renormalized particle dispersion. However, the experimental scattering rate may encompass contributions beyond those originating from single particles, including electron-

phonon interactions and elastic scattering [118]. Elastic scattering by defects can be considered a constant background [120] within a semiclassical approximation. Alternatively, the elastic term dependence on E can be estimated in relation to the band velocity, given by $\Gamma_{el}(E) = \frac{\Gamma(0)v(E)}{v(0)}$, where $E = 0$ denotes the Fermi energy.

4.3.1.3 Angle and momentum dependencies of photoemission processes

The ARPES spectrum serves as an intensity map delineating momentum and binding energy concerning a specific sample orientation. Binding energy, denoted as E_B, is characterized by a shift in detected kinetic energy, aligning with the condition where Fermi energy (E_F) coincides with E_B equal to zero, as outlined in equation 81. In this conceptualization, E_B represents the minimum energy requisite for extracting an electron from the material.

$$E_k = h\nu - \phi - |E_B|. \tag{81}$$

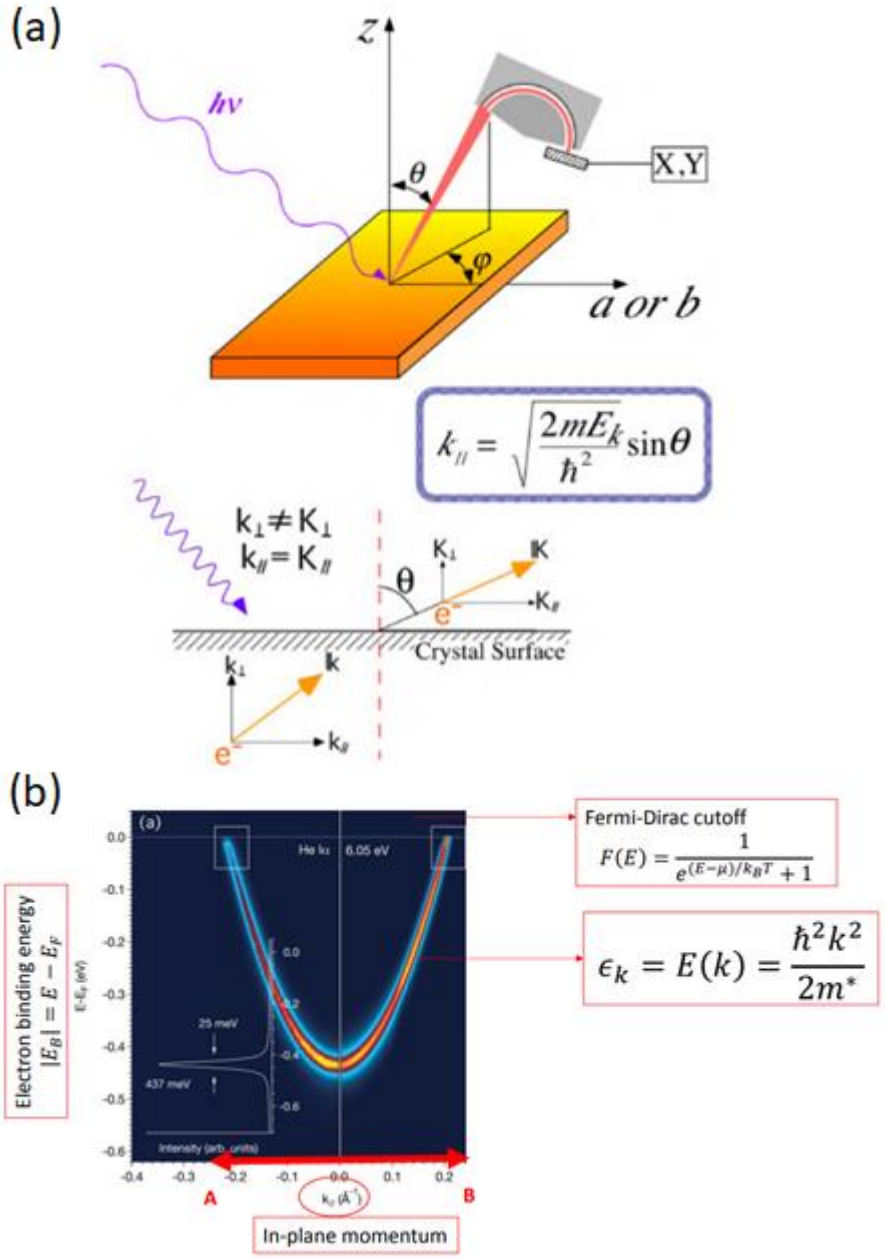

Figure 18: (a) A schematic representation of an ARPES experiment with incident light of energy $h\nu$. The detector is positioned at a polar angle θ and azimuthal angle φ. The electron momentum parallel to the sample surface projection is shown in the blue box. $\boldsymbol{k}$ is the electron momentum inside the material, while $\boldsymbol{K}$ is the electron momentum in the vaccum [121]. (b) ARPES measurement of Cu (111) showing the energy dispersion with respect to the electron momentum [122].

The momentum of an electron within the sample can be decomposed into parallel and perpendicular components, denoted as $\boldsymbol{k} = \boldsymbol{k}_\perp + \boldsymbol{k}_\parallel$, where $\boldsymbol{k}_\perp = \boldsymbol{k}_z$ and $\boldsymbol{k}_\parallel = \boldsymbol{k}_x + \boldsymbol{k}_y$.

Momentum dependency is intricately linked to the detection angle. The momentum parallel to the sample surface remains conserved, facilitating the mapping of photoemission intensity concerning parallel momentum and the binding energy of the photoelectron. However, due to the discontinuity in the perpendicular direction within the medium, momentum conservation in that axis is not upheld. This can be observed in figure 18-(a).

Utilizing the electronic dispersion equation for a free electron, $E_{k\prime} = \frac{\hbar^2 k'^2}{2m}$, which correlates kinetic energy with momentum in a vacuum, allows for the decomposition of electron momentum in vacuum, denoted as **K**, as expressed in equations 82, where k = |**K**|.

$$K_x = k_x = \sqrt{\frac{2mE_k}{\hbar}}\, sin\,\theta\, cos\,\varphi$$
$$K_y = k_y = \sqrt{\frac{2mE_k}{\hbar}}\, sin\,\theta\, sin\,\varphi\,. \tag{82}$$
$$K_z = k_z = \sqrt{\frac{2mE_k}{\hbar}}\, cos\,\theta$$

Here, θ represents the polar angle, and φ corresponds to the azimuthal angle, as illustrated in figure 18-(a). The analyzer slit covers a θ interval, so when$\varphi = 0$, the k_y value remains constant, and the measurement is conducted along k_x. While the in-plane components are preserved, the perpendicular out-of-plane component is not conserved. The k_z component can be inferred from energy conservation, as demonstrated in equation 83: the inner potential V_0 must be considered for the electron departing the material and being detected.

$$E_k + V_0 = \frac{\hbar^2}{2m}\left(k_\perp^2 + k_\parallel^2\right)$$
$$k_\perp^2 = (E_k + V_0)\frac{2m}{\hbar^2} - \frac{2m}{\hbar^2}E_k \sin^2\theta$$
$$k_\perp^2 = \frac{\sqrt{2m(E_k\, cos^2\,\theta + V_0)}}{\hbar}. \tag{83}$$

In figure 18-(b) it is showed the energy dispersion of Cu (111) measured by ARPES. Knowing the angle and the kinect energy of the photoemmited electron, it is possible to obtained the binding energy and the momentum, seen in equations 81 and 82. As a result, the band structure of the material is built, as observed in figure 18-(b). These results matched with

the theoretical prediction of the energy dispersion for Cu (111) (free electrons in a 2D electron gas).

To characterize the entire 3D Brillouin zone, an ARPES experiment involves scanning at different angles to access varying k_x, k_y and k_z values, as described in equation 82 and illustrated in figure 19. By adjusting the tilt angle ϕ, a range of k_x values can be probed for $k_y \neq 0$. For measurements along distinct high-symmetry directions, the azimuthal angle φ is altered. In the case of a sample with 4-fold rotational symmetry, each 90° rotation theoretically results in no discernible difference. Therefore, the only other high-symmetry rotation different from 0° would be 45°. Additionally, scans may be required with changes in the incoming energy hν to estimate the V_0 value needed to identify k_z for high-symmetry points in reciprocal space.

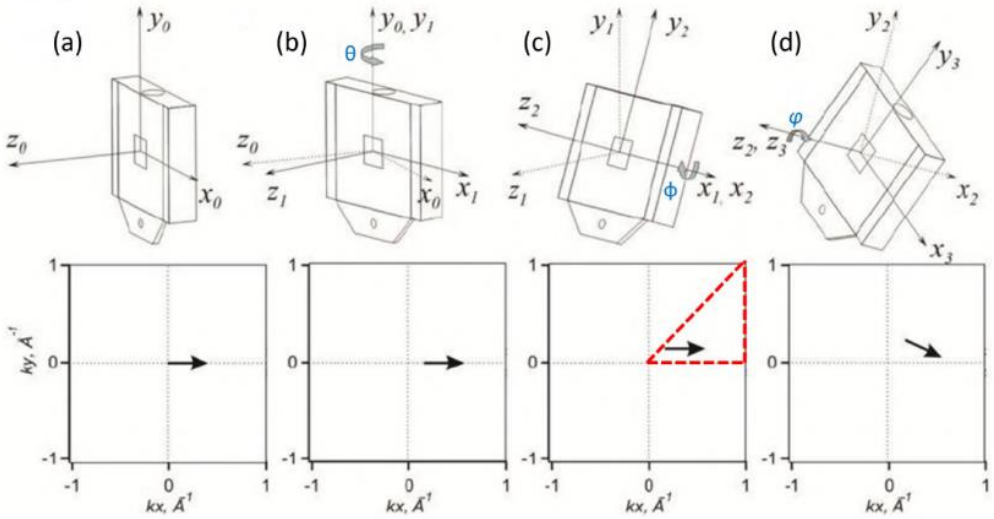

Figure 19: The rotation degrees of freedom polar, tilt and azimuthal which are accessible with an IFW-cryo manipulator. The upper (lower) schematics show sequential rotations in real (for a horizontal slit in k) space. Adapted from [123].

4.3.2 Instrumentation

The instrumentation required for ARPES measurements encompasses the X-ray source, the ultra-high vacuum environment housing the sample, and the electron analyzer, all of which will be explained further. Beyond the environment, the sample holder must possess positional and angular degrees of freedom to align the sample with respect to the photon beam and scan different k-space points. X-ray sources like helium lamp or a laser emit photons with energies

in the range of a few electron volts and this limits its use to the initial characterization of samples. On the other hand, the utilization of a synchrotron expands the experimental possibilities to conditions inaccessible to a conventional table-top ARPES setup.

The energy tunability inherent in a synchrotron source allows for the exploration of different values of k_z in the measured spectra. This feature is particularly valuable for elucidating the out-of-plane dispersion of the electronic structure. Precise identification of high-symmetry points in reciprocal space necessitates some tuning. Moreover, higher energies are imperative to reach more distant points in reciprocal space, given that the absolute value of k is proportional to the square root of the photoelectron kinetic energy.

Another advantage of employing a synchrotron facility lies in its high photon count, small beam as well as the possibility to control the photon polarization. This becomes crucial to dicern between bulk and surface states on the electronic band structure and for that we have used the Bloch beamline from MAX IV synchrotron (Lund, Swedeen) in this thesis.

4.3.2.1 Vaccum and cryogenics

In the realm of soft X-rays, maintaining ultra-high vacuum (UHV) conditions becomes imperative, as the presence of air can lead to the absorption and scattering of low-energy photons and chemical reactions with the sample. Consequently, in an ARPES configuration, all optical components, the sample, and the detection environment must operate under vacuum better than 5×10^{-10} mtorr. The manipulation of samples within the vacuum chamber requires a cryomanipulator for the sample holder. This device facilitates rotation and precise positioning of the sample within the cooling environment. For experiments conducted at low temperatures, many beamlines are equipped with liquid helium cryogenic systems, although liquid nitrogen can also be employed for achieving moderately low temperatures, 78K.

Given the surface-sensitive nature of the photoemission process, due to its shallow penetration depth of a few angstroms, the sample must be cleaved inside the vacuum chamber to ensure high-quality measurements. This practice prevents oxidation and contamination of the measured surface. Cleaving methods vary; for certain Van der Waals materials, a simple scotch tape may suffice, breaking out-of-plane bonds and removing an entire layer of the sample to expose a fresh surface in the UHV environment.

Alternatively, crystal growth can occur within a preparation vacuum chamber from the outset, utilizing evaporation or sputtering techniques. Subsequently, the sample is transferred to the measurement chamber through an UHV transfer line. This sophisticated approach involves separated components with their vacuum pumps. While not universally supported by all facilities or setups, it is feasible in modern synchrotron beamlines. Maintenance of all vacuum components is paramount to ensure cleanliness and freedom from contaminants. Therefore, meticulous ARPES setup maintenance is critical for achieving and sustaining optimal operating conditions.

4.3.2.2 Electron analyzer

The electron analyzer, or spectrometer, takes the form of a hemispherical device with the capability to deflect incoming electrons in a curved trajectory, positioning them at different detection points based on their kinetic energies, see figure 20-(a). This deflection relies on the potential lens effect, where an electrostatic potential can focus the electron beam, akin to how a photon beam is influenced by an optical lens system. The operation of the electron analyzer unfolds in several steps: initially, an electrostatic lens system decelerates and focuses the electron beam onto the analyzer entrance slit. Subsequently, electrons passing through the entrance slit are deflected by the electric field in between two spherical hemispheres. Finally, the electrons pass through the exit slit and are detected, figure 20-(b). The spectrometer components are enclosed within UHV environment to prevent scattering and absorption from air particles. Moreover, the potential lens system is sensitive to magnetic field effects on electron trajectories, necessitating an ARPES environment ideally shielded from magnetic field influence. Following their emission from the sample, photoelectrons scatter in various directions. The acceptance angle for the spectrometer, defining the maximum k range for the measured spectra, is determined by the slit width at the entrance of the electrostatic lens system and its distance from the sample. The electron lens system focuses the electron beam at the detector entrance, resolving the electrons by their angle around a certain θ about the sample normal.

This system also accelerates and decelerates the electrons, concentrating their kinetic energy around a designated value known as Pass Energy (E_P), ultimately linked to the energy resolution. Additionally, slits are strategically placed between the potential lens to prevent vertical angular dispersion, ensuring that the angular dispersion occurs along the entrance slit direction (horizontal). This design ensures that all electrons enter the hemispherical analyzer at approximately the same vertical position, later to be separated by energy in this direction.

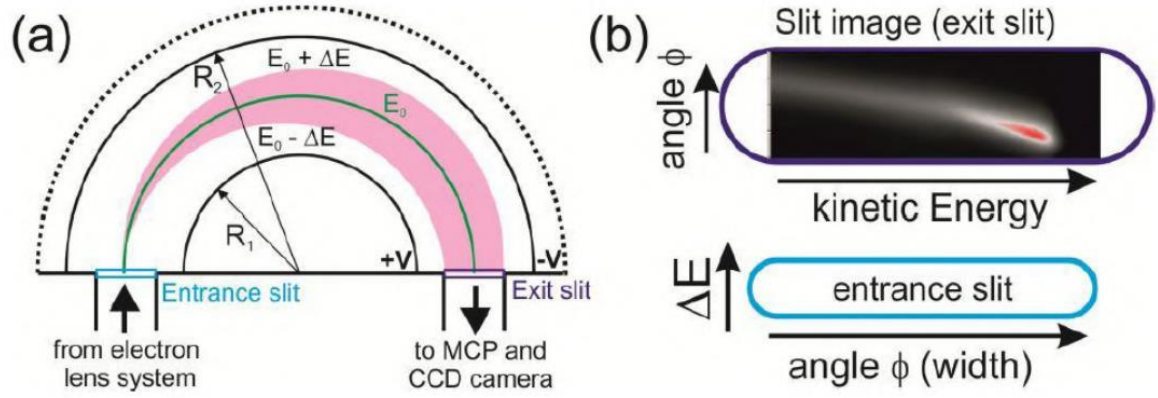

Figure 20: (a) A schematic representation of a spherical electron analyzer with internal radius R_1 and external radius R_2. (b) An example of spectral function measured at the exit slit for graphene as a function of angle and energy is shown in the entrance slit image. From ref [123].

The hemispherical analyzer comprises two half-spheres with radius R_1 and R_2, maintained at a potential difference V. As the electron beam enters the space between both half-spheres, electrons with lower kinetic energy experience more deflection due to the potential, while those with greater kinetic energy describe a trajectory with a larger radius, hitting the exit slit closer to the outer sphere. In contrast, slower electrons hit the exit slit closer to the inner sphere. This process creates energy dispersion, as depicted in figure 20-(a). To achieve resolution in both angle and energy for electron detection, electrons with different angles but the same kinetic energy must travel along a plane perpendicular to the one resolving energy, as illustrated in figure 20-(b). After passing through the exit slit, electrons have their positions determined by their respective kinetic energy, striking a set of microchannel plates (MCP). Each MCP functions as an electron multiplier through secondary emission processes triggered by an electric field. Subsequently, the electrons strike a fluorescent phosphor screen, generating an equivalent photon beam that is detected by a charge-coupled device (CCD).

The electrons exhibit linear energy dispersion around the pass energy E_P; consequently, a higher E_P results in increased final intensities, albeit with reduced energy resolution. This relationship is succinctly expressed in equation 84, where ω represents the entrance slit width, $R_0 = \frac{(R_1+R_2)}{2}$ denotes the mean radius between both spheres, and α represents the acceptance angle.

$$\Delta E = E_P\left(\frac{\omega}{R_0} + \frac{\alpha^2}{4}\right). \tag{84}$$

The momentum resolution is intricately linked to the number of angle channels at the MCP and the acceptance angle. Opting for lower acceptance angles and a greater number of channels contributes to enhanced angle resolution in the final spectra, albeit at the expense of intensity. Therefore, continual technical advancements in electron analyzers are imperative to enhance the resolution, intensity, and overall feasibility of ARPES experiments. In this context, a pivotal characteristic of an electron analyzer is its intrinsic work function. Lowering the analyzer work function proves advantageous for investigating ARPES spectra at lower binding energies and facilitates efficient operation with laser sources, typically in the ultraviolet range.

At the Bloch beamline, the DA30 electron analyzer from Scienta Omicron is employed. This analyzer utilizes deflecting lenses to capture electrons in an area perpendicular to the slit direction. This configuration allows for probing Fermi surface maps without any sample movement, mitigating issues such as prolonged collection times, intensity inconsistencies, and alignment challenges. However, it is worth noting that the probed Fermi surface exhibits a circular shape, in contrast to the square shape typically obtained when acquiring maps by adjusting the tilt angle. Consequently, certain features at higher momenta may be overlooked. The DA30 offers discrete options for pass energy (Ep) at 1, 2, 5, 10, 20, 50, 100, and 200 eV. Although this limits the tuning flexibility for energy resolution, electron counting, and binding energy range, it stands out as one of the analyzers with superior resolution.

5 Evidence of Thickness-dependent Surface Induced Ferroelectricity in Few-layer Germanium Sulfide obtained via Scanning Tunneling Spectroscopy

In this section we will discuss the first project of this thesis, the observation of a thickness-depedent tunneling current up reducing the number of layers of Germanium Sulfide (GeS) nano flakes. Vapor-phase deposition was used to synthesize ultrathin germanium sulfide nano-flakes on a highly oriented pyrolytic graphite substrate. Nanostructures of variable thicknesses were characterized using scanning tunneling microscopy and spectroscopy. Tunneling currents under forward and backward biases were measured as a function of the nano-flake thickness. Remarkably, we clearly observe a hysteresis pattern, which we attribute to surface ferroelectric behavior, consistent with screening conditions of polarization charges. The effect increases as the number of layers is reduced. This experimental result may be directly applicable to miniaturized memory devices, given the two-dimensional nature of this effect.

5.1 Introduction

Ferroelectric materials have received significant attention due to the fundamental aspects of the physics involved in their behavior, as well as to their switchable properties, which make them attractive in a variety of applications, including non-volatile memories and neuromorphic computing [124], [125], [126], [127], [128]. For these reasons, achieving stable ferroelectricity in ultrathin films is particularly important, with technological applications in the miniaturization of sensors, memories and optoelectronic devices [129], [130]. However, the investigation of polarization effects in the surface structure and the detailed description of the hysteretic behavior are still a challenge. In this context, the recent discovery of ferroelectricity

in two-dimensional 2D van der Waals (vdW) materials represents a unique opportunity to unveil this phenomenon in the ultrathin limit [131], [132], [133].

A possible material to be used in novel devices is GeS, a group IV-VI layered monochalcogenide, whose ferroelectric behavior has been the subject of numerous studies, especially by means of electric response measurements. Scanning tunneling spectroscopy, when combined with tunneling microscopy, may be a powerful technique to assess the hysteretic electronic behavior correlated with the film structure [134], [135], [136], [137].

In the present work, we focus on this technique, and we demonstrate the observation of a thickness-dependent phenomenon of ferroelectricity. Germanium sulfide nanoflakes were deposited on highly-oriented pyrolytic graphite (HOPG). We characterized the GeS/HOPG heterostructure by STM and STS measurements. STS spectra exhibit a pattern consistent which semiconductor such as GeS. These were compared with first-principles calculations based on the density functional theory. Remarkably, we observed hysterical loops in the tunnelling curves when forward and backward biases were applied.

We ascribe this observation to thickness-dependent surface induced ferroelectricity of germanium sulfide flakes. The STM tip creates a strong local electric field, which is able to switch the polarization of the topmost GeS layer. This effect results in a hysteretic behavior, which increases monotonically as the film thickness decreases.

5.1 Germanium Sulfite (GeS)

Germanium Sulfide is a p-type semiconductor with orthorhombic layered crystalline structure. It has strong covalent bonding within the layer and weak van der Walls interactions between adjacent layers. This facilitates the growth of 2D nanostructures in these systems. The band gap for GeS has been reported to be in range of 1.55-1.65eV [138]. These values match the desired absortion range for an efficient photovoltaic material. Besides optoeletronic applications, GeS nanosctrucutures also exhibited excellent lithium storage properties [139]. However, only limited studies have been published on GeS nanostrucutures compared to others IV-VI semiconductiors such as lead or tin-based chalcogenides.

The GeS unit cell is composed by 8 atoms, 4 Germanium (Ge) atoms and 4 Sulfur (S) atoms. These atoms form a A-B stacking composed by two layers, see figure 21-(a). Due the

in-plane distribution of G and S atoms in each layer, a non-zero polarization vector along b-direction is founded in this material. Each of these two layers have this polarization vectors in the opposite direction, figure 21-(b). This fact makes the bulk an antiferroeletric material, but as we approach to the 2D limit, the residual polarization vector from the top most layer becomes more evident making this material a ferroeletric.

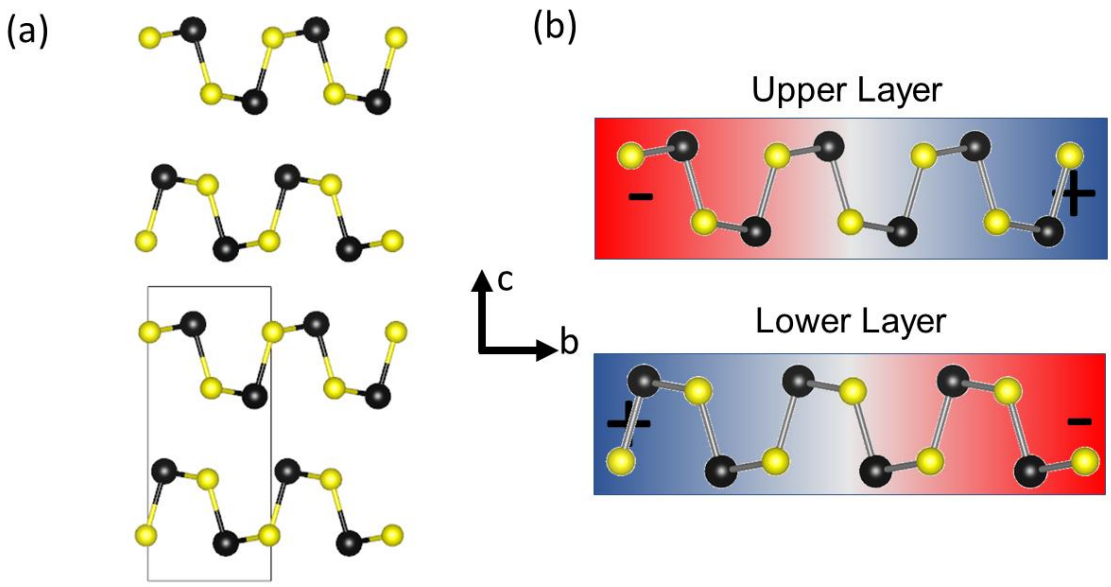

Figure 21: (a) Orthorombic structure of Germanium sulfide. Ge and S atoms are represented by black and yellow atoms, respectively. (b) The charge distribution from upper and lower layers that compose the unit cell. Both have a non-zero polarization vector in opposite b-direction.

5.2 Growth and Characterization

In our experiment, we obtained GeS crystals by mixing the two elements in a stoichiometric ratio, using 0.3g of 99.999% pure germanium powder and 0.14g of 99.99% pure sulfur powder. Both materials were put into a quartz tube. The tube was evacuated, sealed and heated to 1000°C for four days. The characterization of GeS crystals was achieved by X-ray powder diffraction (XRPD) and energy dispersive electron spectroscopy (EDS). For the X-ray diffraction analysis, a focused monochromatic sub-millimeter beam (λ = 0.154nm, Cu K-alpha1) was employed. Powder diffraction analysis was performed by using the MAUD [140]

software which was used to analyse the phases of the GeS sample. Fitting results confirmed the desired Pnma phase of GeS, see figure 22 left pannel. XRPD measurements were carried out in a Panalytical Empyrean system, equipped with a two-dimensional detector and a Cu K-alpha source (LabCri-UFMG). Samples were finely grinded and measured in the range from 4° to 150°. The region with strongest peaks was then analyzed throughout the Maud Rietveld package using reference crystallographic data for GeS crystal.

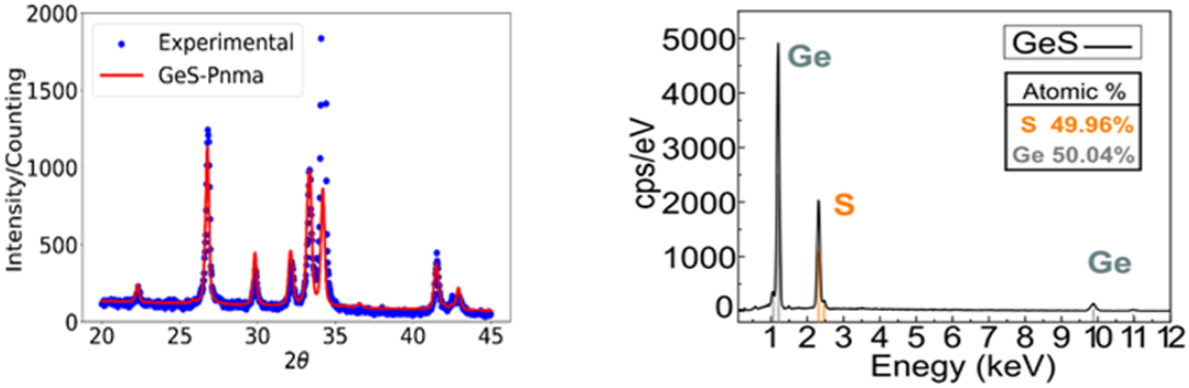

Figure 22: Left panel - X-ray power diffraction pattern of GeS sample. The blue dots are the experimental data and the red line is the fit using MAUD software for GeS Pnma phase. Right panel - Energy dispersive spectroscopy of GeS crystal.

EDS was performed on several spots of the sample surface and the result showed an atomic ratio between S and Ge of approximately (49.96±0.01)% and (50.04±0.02)%, see figure 22 right pannel. The spectrum aquired in different regions is shown in table2.

Element	Region 1	Region 2	Region 3	Region 4	Region 5	Region 6
S	48.88 (%)	49.18 (%)	49.40 (%)	49.46 (%)	51.88 (%)	48.32 (%)
Ge	50.95 (%)	49.49 (%)	50.18 (%)	50.54 (%)	49.04 (%)	49.68 (%)

Table 2: Atomic ratio of Germanium and Sulfur at different regions of the crystal, as obtained by EDS.

To obtain GeS nano-flakes, we used physical vapor deposition (PVD) to transport a small portion of the powder material onto a few highly oriented pyrolytic graphite substrates (see figure 23-(a)). The process involved the use of a quartz tube (internal diameter of 400 mm), connected to a roughing pump, with a temperature gradient from 500°C down to 250°C. A total of 28.2 mg of GeS material was placed at the frontal part of the furnace at 430°C and HOPG substrates were placed 7-12 cm from the GeS source, at approximately 320°C. We used a carrier gas mixture of argon (20 sccm) and hydrogen (H2, 10 sccm). Pressure was maintained at

2×10^{-1} mbar. After the PVD procedure, orthorhombically-shaped GeS flakes were successfully obtained as we expected for the Pnma phase (see figure 23-(b)).

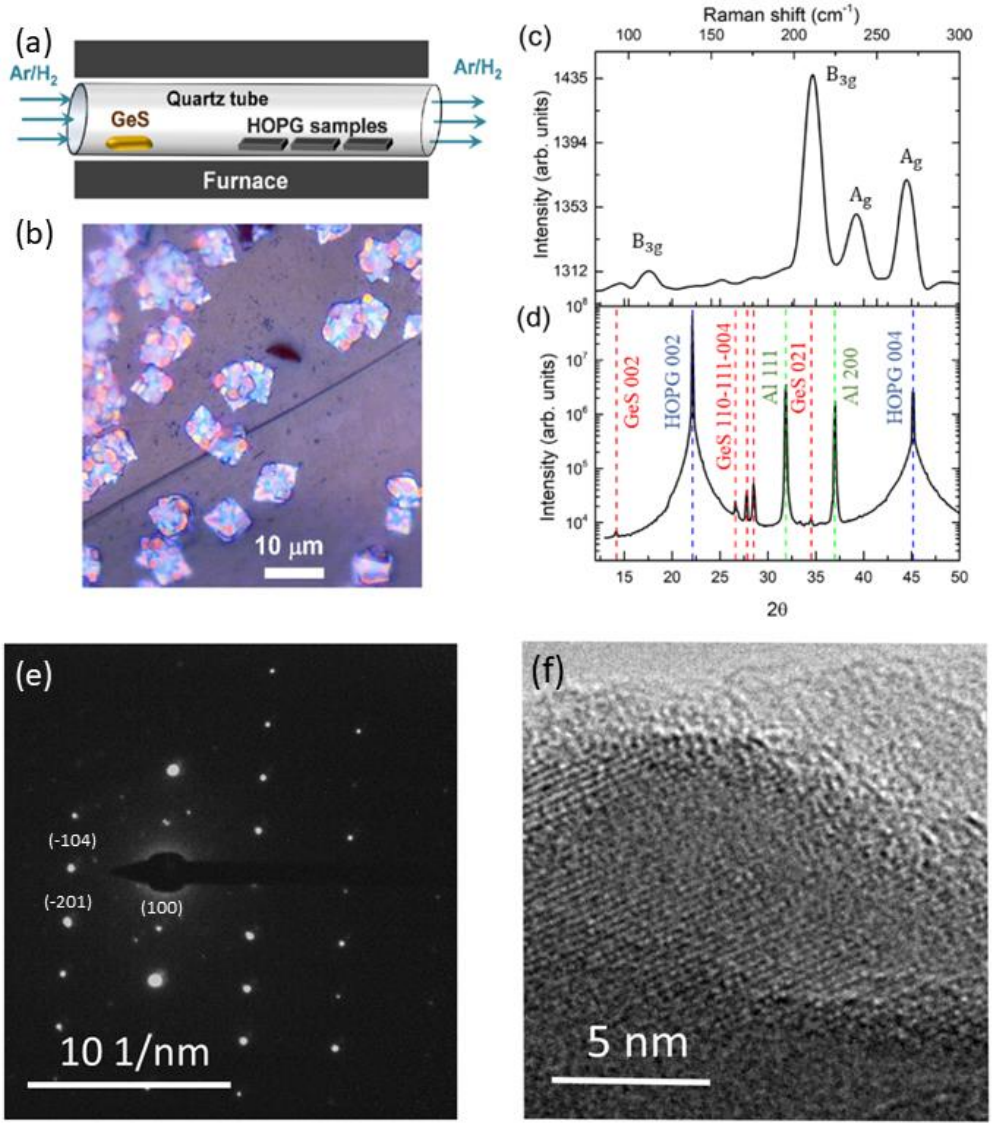

Figure 23: (a) Schematic image of PVD process. (b) Optical microscopy image of GeS flakes on HOPG. (c) Micro Raman spectrum from GeS flakes. (d) Micro X-Ray diffraction pattern from GeS flakes, blue dashed lines correspond to 00L HOPG X-ray peaks and red dashed lines to GeS Pnma ones. (e) SAED pattern of a GeS nanoflake indicating the orthorhombic Pnma phase. (f) HRTEM showing the atomic displacement of GeS nanoflake.

In order to confirm that the phase of the material after deposition remained the same, Raman spectroscopy was employed to confirm the purity of the germanium sulfide flakes. Raman measurements were performed using a Witec alpha300 RA instrument with a

wavelength of $\lambda_{laser} = 532\text{nm}$. A 1800g/mm grating was used, and the laser power was maintained at 100μW. Characteristic peaks for germanium sulfide, consistent with those reported in the literature, were obtained (figure 23-(c)) [141].

We conducted micro-X-ray diffraction measurements at the EMA Beamline of the Brazilian Synchrotron Light Source (Sirius). A Huber 6-circle diffractometer was used with a 20x20 micrometer beam and a wavelength of 0.13041 nm (see figure 23-(d)). The diffraction pattern revealed the presence of GeS, HOPG and aluminium (sample holder) peaks, these peaks values is depicted in table 3. Since the X-ray transmission throughout 100nm of GeS and 500nm of HOPG is of 98% and 75%, respectively, two peaks from the aluminium sample holder were also observed [142].

Structure	Phase	hkl	Position (2θ)	Relativity Intensity	Structure Factor
GeS	Pnma	002	14.1	9.4	20.7
GeS	Pnma	110	26.65	35.5	78.8
GeS	Pnma	111	27.74	40.4	87
GeS	Pnma	004	28.52	100	139.5
GeS	Pnma	021	34.56	15	68.1
HOPG	P63mc	002	22.15	100	17.3
HOPG	P63mc	004	45.19	7.2	10
Al	Fm-3m	111	31.86	35.8	100
Al	Fm-3m	200	37.02	49	34

Table 3: X-Ray experimental peaks relating the information of structure, phase, HKL indices, relative intensity and structure factor for GeS, HOPG and Aluminum. The relative intensities and structure factors for each structure were calculated individually.

In order to investigate the local crystal structure of the material, Transmission Electron Microscopy (TEM) and Selected Area Electron Diffraction (SAED) measurements were carried out on a 200 kV LaB_6 -Tecnai G2-20 microscope (FEI-Thermofischer Scientifics). The TEM sample was prepared by gently scraping the surface of the GeS film deposited onto HOPG substrates. The resulting residue was dispersed in isopropyl alcohol and dipped onto a 300-

mesh holey carbon TEM Copper grid (2SPI Suplies). The low magnification image of the edge of a small flake of the GeS film fixed onto the carbon film of the TEM grid is presented in figure 24-(b). An optical image of a GeS flake is depicted in figure 24-(a).

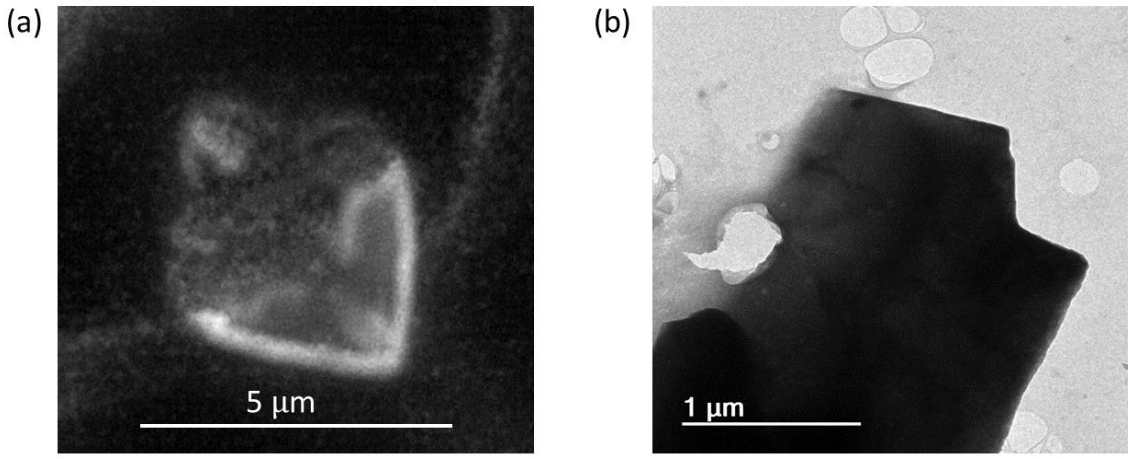

Figure 24: (a) Optical image of a GeS flake. (b) The low magnification image of the edge of a small flake of the GeS film fixed onto the carbon film of the TEM grid.

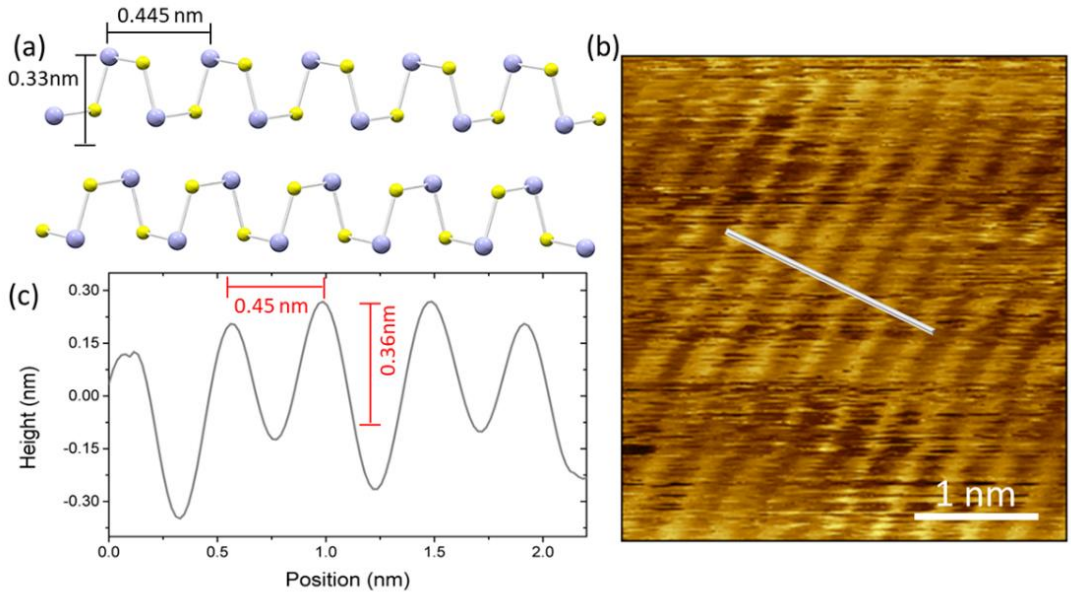

Figure 25: (a) Atomic structure of the GeS Pnma phase. (b) STM atomic resolution of our GeS sample. STM image with sensitivity to atomic stripes was taken using $I_T = 500pA$ and $V + 2V$,with a measurement field of view of 4nm x 4nm. (c) Surface topography profile obtained in (b).

Figure 23-(e) show the SAED for the GeS nano flake shown in panel (f). This diffraction pattern is related to an orthorhombic crystal structure. In the HRTEM of Figure 23-(f), acquired for one GeS nanoflake, it is possible to observe the atomic arrangement of different layers. In order to identify the crystallographic structure, the electron diffraction pattern was indexed using the Diftools Script Package[143] for Gatan Digital Micrograph™ software. Lattice spacings in HRTEM images were also determined using Gatan Digital Micrograph software. The experimental electron diffraction patterns and HRTEM analyses are consistent with the GeS orthorhombic phase (a = 0.363 nm, b=0.429 nm e c= 1.042 nm).

Atomically-resolved STM measurements were performed to confirm that our GeS flakes are in the Pnma phase. The experimental lattice parameters found using the STM aligns with the expected for GeS, see figure 25.

5.3 Scanning Tunneling Microscopy/Spectroscopy Study

To investigate our GeS ultra-thin flakes, we employed an Omicron VT-STM scanning tunneling microscope/spectroscope operating at $1.7 \times 10^{-10} mbar$ at room temperature. Since GeS is a semiconductor with a bandgap of approximately 1.6eV, HOPG played a dual role in our experimental setup. It both enabled the creation of an electrically closed circuit, necessary to measure the tunneling current, and also modified the DoS of thin layers of GeS inside the band gap, allowing us to analyze the behavior of electrons within the gap.

In figure 26-(a), an STM image reveals two stacked flakes, both greater than 50 nm in height (approximately 50-unit cells), exhibiting bulk behavior. We performed several scanning tunneling spectroscopy measurements to investigate the electronic behavior of bulk GeS. To obtain a typical STS curve, 30 STS measurements were taken into consideration to better ensure the reliability of our results. STS measurements were performed using a lock-in amplifier Stanford Research Systems SR-810, operating at 2904Hz. STS spectra were extracted from the amplifier which was set with an amplitude of 100mV, phase 154,78°, time constant of 30mV and 24dB.

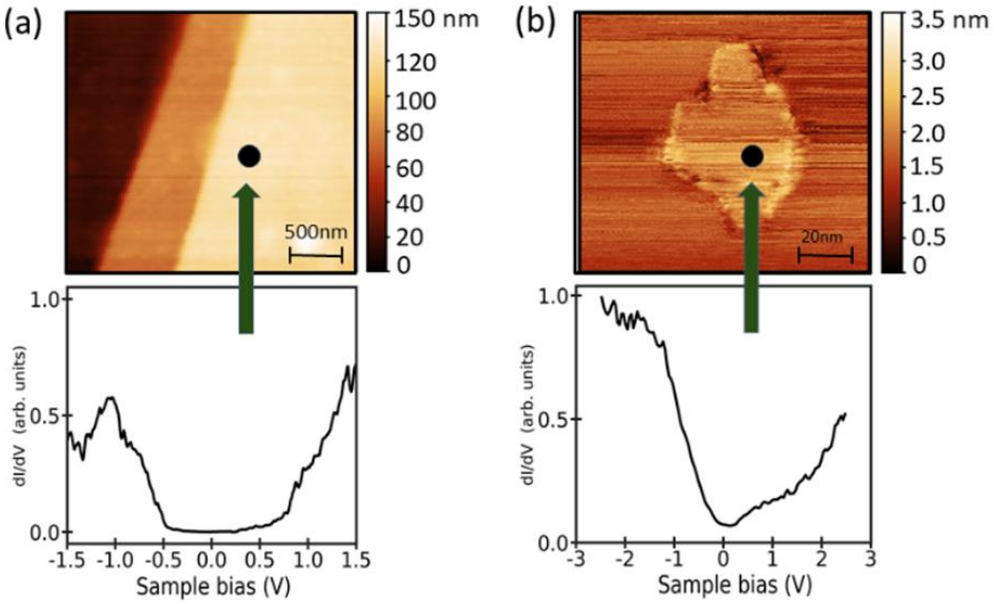

Figure 26: (a) Upper - STM image of stacked GeS flakes (area of $2.5 \times 2.5\mu m^2$, $I_T = 800pA$ and $V_{Tip} = -2V$); Lower - average STS measurement. (b) Upper - STM image of a GeS nanoflake (area of $80 \times 80nm^2$, $I_T = 500pA$ and $V_{Tip} = -1V$); Lower - average STS measurement, showing the electronic behavior a GeS nanoflake.

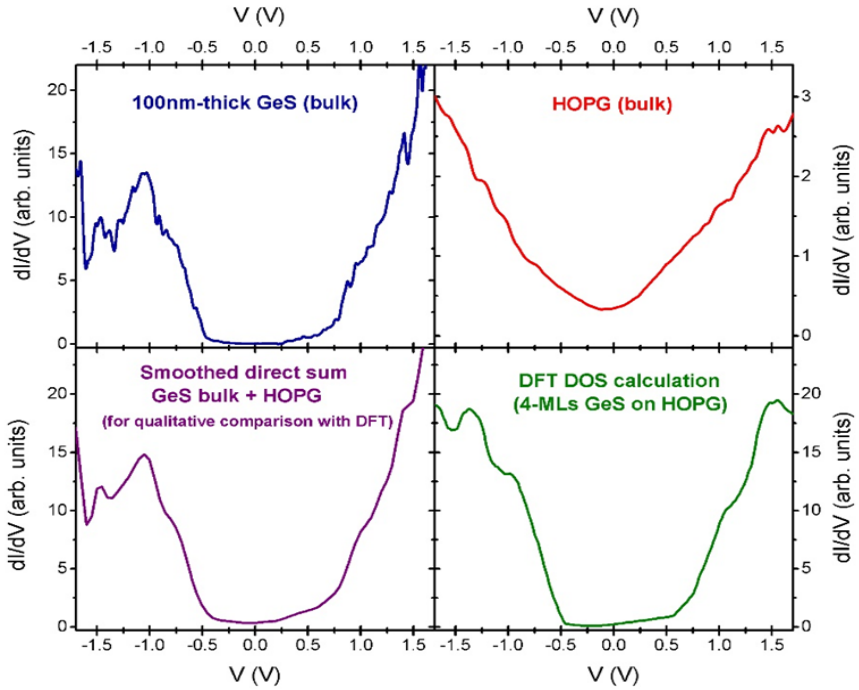

Figure 27: Comparison of scanning tunneling spectroscopy measurements of GeS (upper left), HOPG (upper right), the sum of both (lower left) and GeS flake on HOPG with a calculated density of states of 4 monolayers of GeS on HOPG (lower right).

To investigate the density of states of few-layer flakes, we performed several STS measurements on each flake. The STM image of figure 26-(b) displays a 2nm thick nanoflake. The dI/dV curve nearly matches the predicted shape of a GeS/HOPG system (figure 28). The comparison between GeS and HOPG STS spectra with DFT DoS is shown in figure 27.

5.4 DFT Calculations

For a better understanding of the properties of GeS nano-flakes, we performed DFT calculations. Firstly, we calculated the bulk properties of GeS using DFT to compare them with STS spectra. We then investigated how the low dimensionality changes the electronic behavior of atomically thin GeS flakes. Additionally, we modeled the GeS/HOPG junction to observe changes in the electronic density of states that correspond to our STS measurements. Our DFT implementation is based on the SIESTA program. It makes use of a numerical basis set formed by pseudoatomic orbitals, which includes, in our calculations, two functions for each valence state plus polarization orbitals, the so-called DZP scheme. The exchange-correlation functional is built within the Generalized Gradient Approximation (GGA) in the Perdew–Burke–Ernzerhof (PBE) parametrization [100]. The PBE scheme rendered lattice constants for GeS (a=4.32 Å, b=3.73 Å and c= 10.64 Å) in good agreement with the experimental results (4.299, 3.646, 10.481 Å for a, b and c, respectively). Test calculations with a van der Waals functional (in the DRSLL parametrization introduced by Dion et al) showed a very close agreement with the PBE result for the DOS in the heterostructure calculation. However, we found larger in-plane lattice parameters for the GeS structure (a=4.58 Å and b=3.77 Å).

Other important parameters are the mesh cutoff, which defines the real-space grid, and the k-grid mesh, which gives the sampling of Brillouin zone. The former was set to 350 Ry, and, for the latter, we employed the Monkhorst-Pack scheme defining grids of 20x20x20 and 20x20x1 for bulk and slab calculations, respectively. We imposed periodic boundary conditions, with vacuum regions large enough (~15 Å) to prevent interactions between periodic images in the slab cases. The geometries were considered relaxed when the maximum force component in any atom was less than 10 meV $Å^{-1}$. The crystal structure of GeS is defined by

a primitive cell comprising four Ge and four S atoms, arranged in two distinct layers which interact through van der Waals forces.

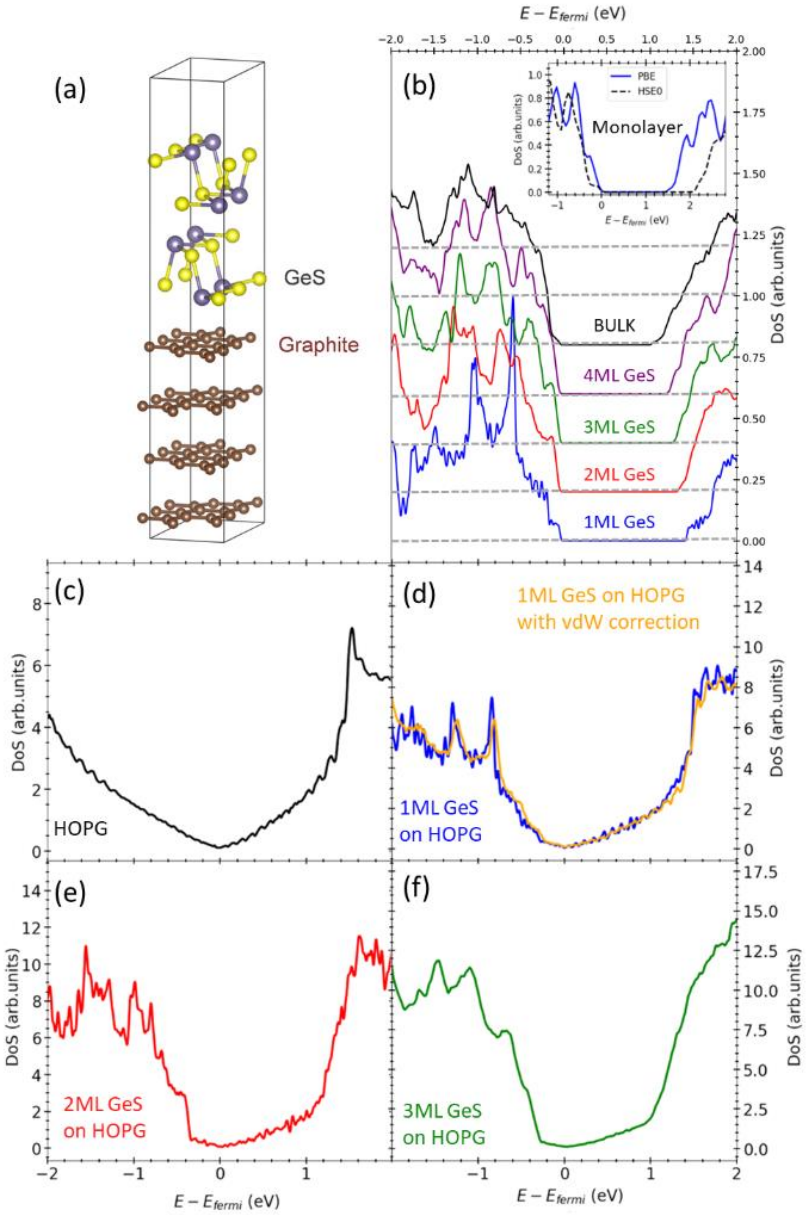

Figure 28: Geometric model of a GeS/HOPG junction used in our calculations for the case of a bilayer GeS. The HOPG is represented in our model with a four-layer graphene in an AB stacking. (b) The density of states for stacked GeS with the number of layers ranging from one to four. Bulk calculation is shown as reference. In the insert figure, the blue solid and black dashed curves are the PBE and HSE0 calculations for monolayer, respectively. (c)-(f): Electronic density of states DoS of (c) HOPG and its junction with (d) a monolayer of GeS, (e) a bilayer and (f) a trilayer.

The bulk bandgap is direct and located at the Γ point. Its value, within our PBE scheme, is 1.18 eV. As a model to theoretically characterize this system, we considered a GeS orthorhombic 2x1 supercell with one to four GeS layers placed on top of a four-layer graphene in a Bernal (AB) stacking comprising a total of 48 carbon atoms, as shown in figure 28-(a). We determined the evolution of the electronic structure of GeS with the number of layers varying from one to four.

The result is depicted in figure 28-(b) in a sequence of DOS plots, along with the bulk case that is reproduced as a reference. The bandgap clearly decreases with the number of layers, going from 1.90 eV (one layer) to 1.35 eV (four layers). These values, as well-known in GGA-PBE calculations, underestimate the bandgaps. The inset in Fig. 28-(b) shows the comparison of the DOS for a monolayer GeS when evaluated with the PBE (blue solid curve) and hybrid functionals (HSE0) (black dashed curve). Both calculations were conducted with the VASP package [144], [145]. The bandgad increases to 2.23 eV in the HSE approach, as expected. Our work focuses on few-layer GeS deposited onto a HOPG substrate. The HOPG DOS, shown in figure 28-(c), features the expected V-shape close to Fermi level. When the two systems are brought together, forming the heterostructure, there is a small charge transfer from graphite to the closest GeS layer, resulting in the DOS curves presented in figures 28-(d)-(f) for one to three GeS layers, respectively. We shall directly compare these curves with the results of our STS measurements

5.5 Nanoflake Electronic Stability

In figures 29-(a) and 29-(b), the lower panels depict topographic STM measurements of both bulk and a nano-flake of GeS, respectively. Each topographic image contains a marked area in which STS measurements were carried out. A qualitative comparison of the topography and the corresponding electronic response of bulk and few-layer GeS is shown in figure 4. First, we present STM images showing the topography of GeS bulk (29-a-i) and a nanoflake (29-b-i). To better understanding the electronic response for each sample, a scan of a zoomed-in area was also performed (figures 29-a-ii and 29-b-ii). From these images, it is possible to observe a difference in the surface topography. The bulk exhibits an irregular surface, whereas the nano-

flake is more uniform, probably due to the deposition procedure. Using STS scans, these zoomed-in regions can reveal their local density of states stability and doping behavior.

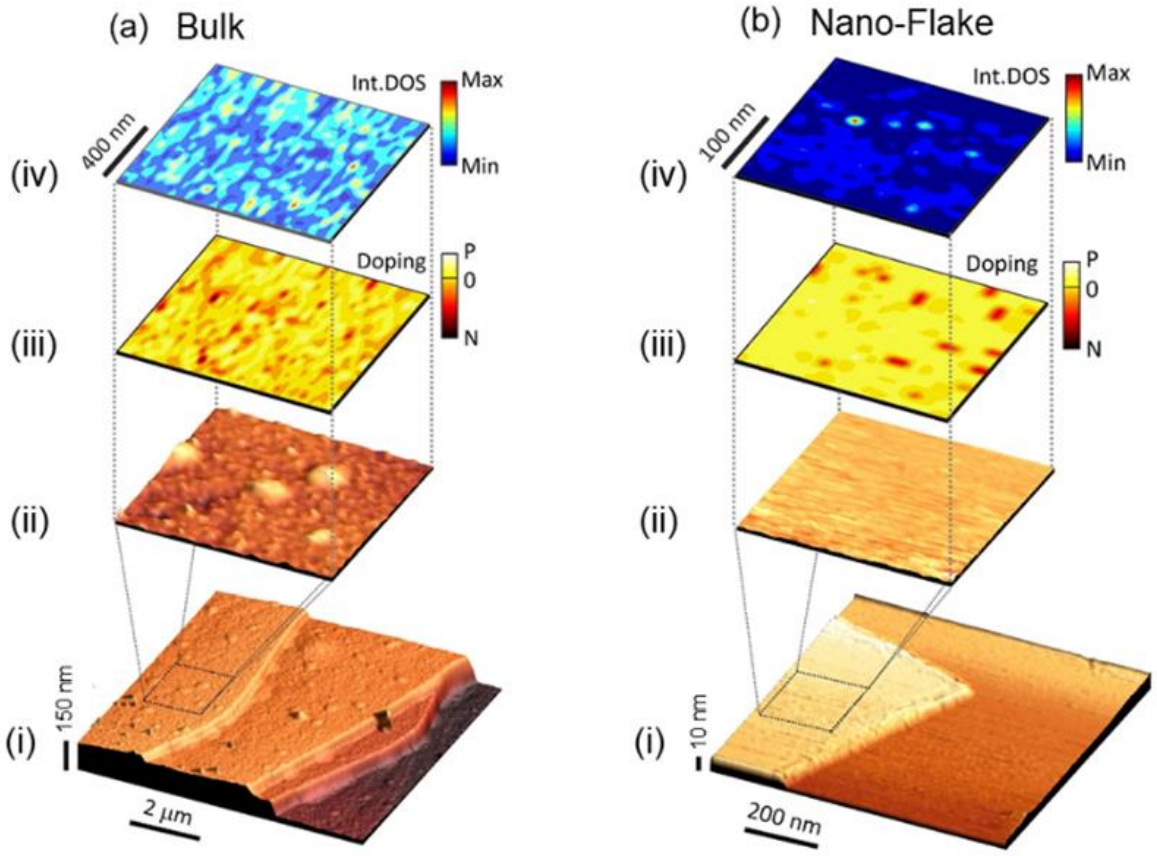

Figure 29: (a) From bottom to top: STM image of the surface of bulk GeS in a 6μm x 6 μm scans ($I_T = 800pA$ and $V_{Tip} = -2V$); STM image of a zoom-in are indicated in the lower STM image; Doping map obtained from a series of STS spectra; Map of the integral of the experimental dI-dV curve from -1.0V to 1.0V (see text) (b) Identical sequence of maps for a nanoflake of 800nm x 800nm, ($I_T = 500pA$ and $V_{Tip} = -1V$). For Nano-Flake, notice the more uniform surface also with fewer fluctuations in the electronic density of states.

The maps, shown in figures 29-a-iii and 29-b-iii, were produced from STS measurements at each sample position. They are related to the doping for bulk and nano-flake, respectively. The doping type was calculated using the difference between the conduction band energy and valence band energy values. P-type (n-type) behavior was ascribed to regions where this difference is positive (negative). Our results show that the doping of few-layer nano-flakes is more uniform, with a dominant p-type doping and a reduced surface fraction with n-type

behavior. It is known that GeS has intrinsic p-type doping, which is also the case for most of the nano-flake surface [146].

The second type of map (shown in figures 29-a-iv and 29-b-iv) is the integral of the dI/dV curves from -1.0V to 1.0V for each scanned surface point. This map reveals how the local density of states changes at the surface of the flakes. Higher values indicate the presence of a larger number of electronic states within this voltage range, pointing to a semi-metallic behavior. Lower values indicate a reduced number of electronic states, i.e., a more semiconducting behavior, typical of GeS. Interestingly, we observed that the few-layer nanoflake presents improved LDOS stability when compared to the bulk, possibly due to stacking flaws introduced during the growth of the material. In such lamellar stacking, GeS bulk is more susceptible to defects as growth proceeds, as evidenced by the color variation.

To investigate the electronic response, for each case, dI/dV curves in these surfaces were acquired using automatic grid scans with 64 x 64 points over areas previously measured with STM. Particularly for the STS maps a minimum of 4 STM images were previously recorded with identical results to avoid tip or surface changes before STS measurements. Finally, the STM microscope collected 20 STS spectra per point and average values were plotted.

5.6 Thickness-dependent Tunneling Current

Figure 30 shows STM images of several flakes with varying thicknesses ranging from 5 to 20 nm with the dI/dV curve for each flake. For each flake we performed a series of STS spectra and take the average to observe the electronic behaviour for different thickness over the HOPG subtract. Such averages are shown in the lower panels of figure 5. Comparing with the DFT calculations in figure 28-(c)-(e) it is possible to observe that the HOPG influences the GeS gap measurement, inducing a non-zero slope for positive bias values in reduced GeS flake thickness.

Through STS measurements at distinct locations on a nanoflake, we identified differences in the current-voltage (I-V) curve when the bias was cycled in a negative to positive or a positive to negative sequence. By varying the voltage from negative to positive values and,

after a 1s interval, a positive to negative current scan, the graph exhibits a different result. This phenomenon was more noticeable for flakes with reduced thicknesses.

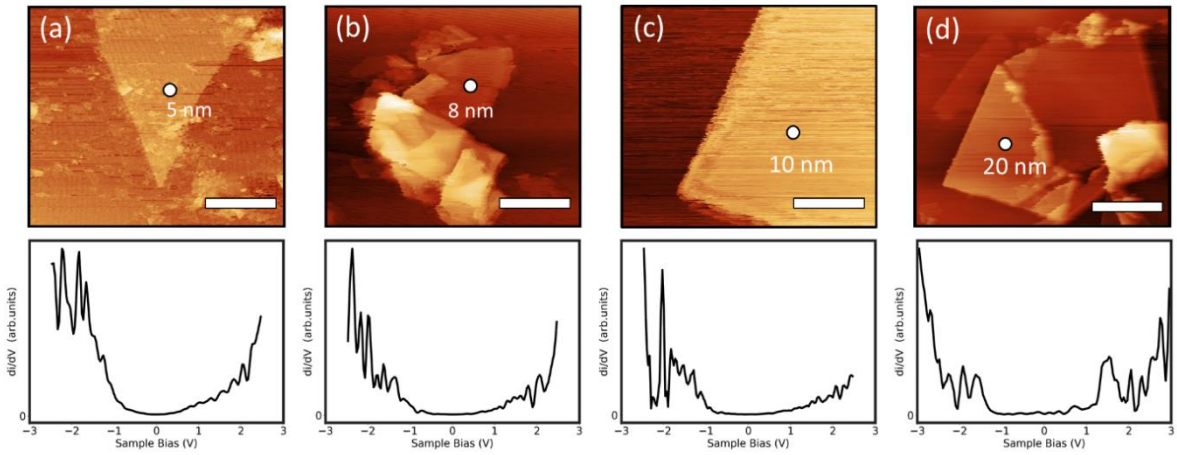

Figure 30: STM images of GeS flakes (upper panels), with the corresponding dI-dV curves (lower panels) at the same location (white dot). All STM images were obtained with $I_T = 500pA$ and $V_{Tip} = -1V$. This series of STM and STS results was measured in flakes with different thicknesses of (a) 5nm; (b) 8nm; (c) 10 nm; (d) 20nm. The scale bar is respectively: 100nm ,100nm, 200nm and 200nm.

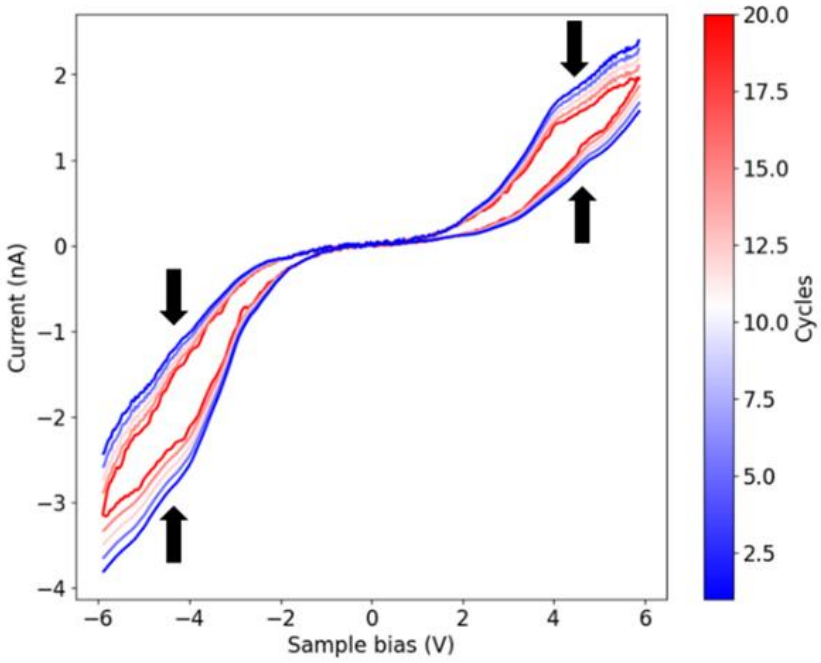

Figure 31: Germanium sulfide I-V curves for different cycles in the same spot at 2-nm thicker nanoflake. The color map is related to the number of cycles.

We have observed that for a series of measurements cycling between these bias values (usually from 20 to 100 cycles), closed loops are clearly observed, see figure 31. This suggests that the observed closed loops are the result of ferroelectric ordering at the surface.

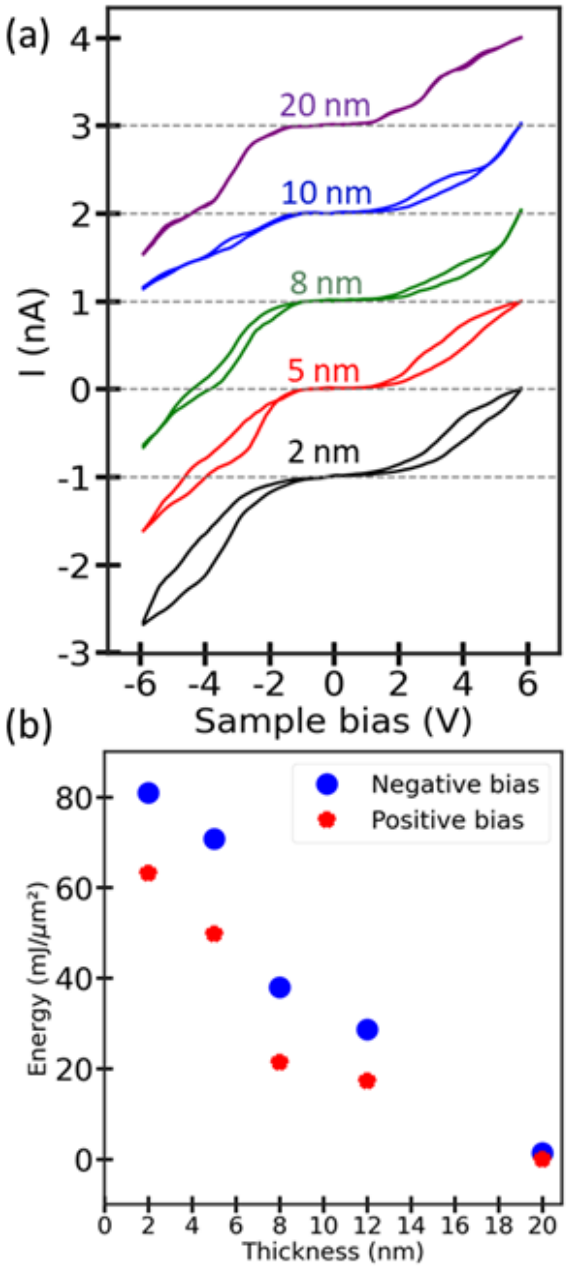

Figure 32: (a) A sequence of I-V curves measured for different GeS flakes. In this graph, forward and backward currents for each thickness are combined at the same curve (with the same color). (b) The energy associated with the inner area for negative and positive bias values in (a).

In figure 32-(a) we present STS measurements for flakes of different thicknesses in a larger voltage range. One observes that, for -6V to +6V back to -6V loops, a pure hysteretic behavior can be identified, and the effect is, again, more pronounced for thinner flakes. These curves in fig. 32-(a) may be used to calculate a lower limit for the electric field energy in GeS flakes. The STS spectra were obtained using 200 points with T-raster of 200ms. The time between the end of forward and begin of backward current was set to be 1s. This energy density can be experimentally estimated from our STS measurements using the relation:

$$u = \frac{U}{A} = \frac{\Delta t}{A}\int_0^V (I_F - I_B)dV', \tag{85}$$

where Δt is the sweeping time of the I-V curve (usually a few seconds), I_F is the forward current and I_B is the backward current. This result is expressed in $\frac{mJ}{\mu m^2}$ units and it is depicted in fig. 32-(b). One observes that the energy density decreases monotonically, starting with a 2 nm-thick flake and reaching a minimum value for 20nm-thick flakes.

In order to exclude the possibility of charge accumulation, which would induce a response with different currents along forward and backward STS scans, we have conducted additional Kelvin Probe Force Microscopy (KPFM) measurements on our flakes using a Nanosurf Flex-AFM with the Nanosurf C3000 controller. Such charging effect is unexpected in our case for thin layers (thin GeS flakes) on top of a conductive substrate under applied bias, since charge leaking through the HOPG substrate is probably dominant.

Nevertheless, if a given flake has misoriented regions (out of crystalline stacking registry) or surface oxide, a minor effect of charge accumulation may take place and must be investigated. In KPFM, both the second derivative of the local capacitance and the surface potential can be monitored, providing images in which distinct contrasts in the same flake would point out to charge trapping. We have then measured KPFM in single-pass mode using a Multi75E-G tip, image-size of $1 \times 1\ \mu m^2$ and fast axis scanning time of 5s. Applied biases from -8V to 8V were used and the specific range of 2V to 6V is depicted in fig. 33.

The in-phase tip potential variation for distinct applied bias values is shown in figures 33-(a) -(c), whereas figures 33-(d)-(f) show the out-of-phase (lock-in filtered) bias. In all panels a thin GeS flake 12 nm thick is observed at the center of each image. These signals are a measure of the second derivative of the local capacitance and the electric surface potential force,

respectively. For the sake of comparison, monolayers of planar molecules in HOPG exhibit potential (color code) scales ranging up to hundreds of mV for applied biases of the order of 2V [147]. Hence, in both KPFM channels one observes variations of tip potential that are 100 times lower than the bias applied to the AFM tip (similar results are retrieved for negative bias values). In figures 33-(a)-(c), the observed potential at the flake is nearly zero, whereas the potential in figures 33-(d)-(f) remains in the order of 1mV. These results indicate that this flake is not charged due to tip potential.

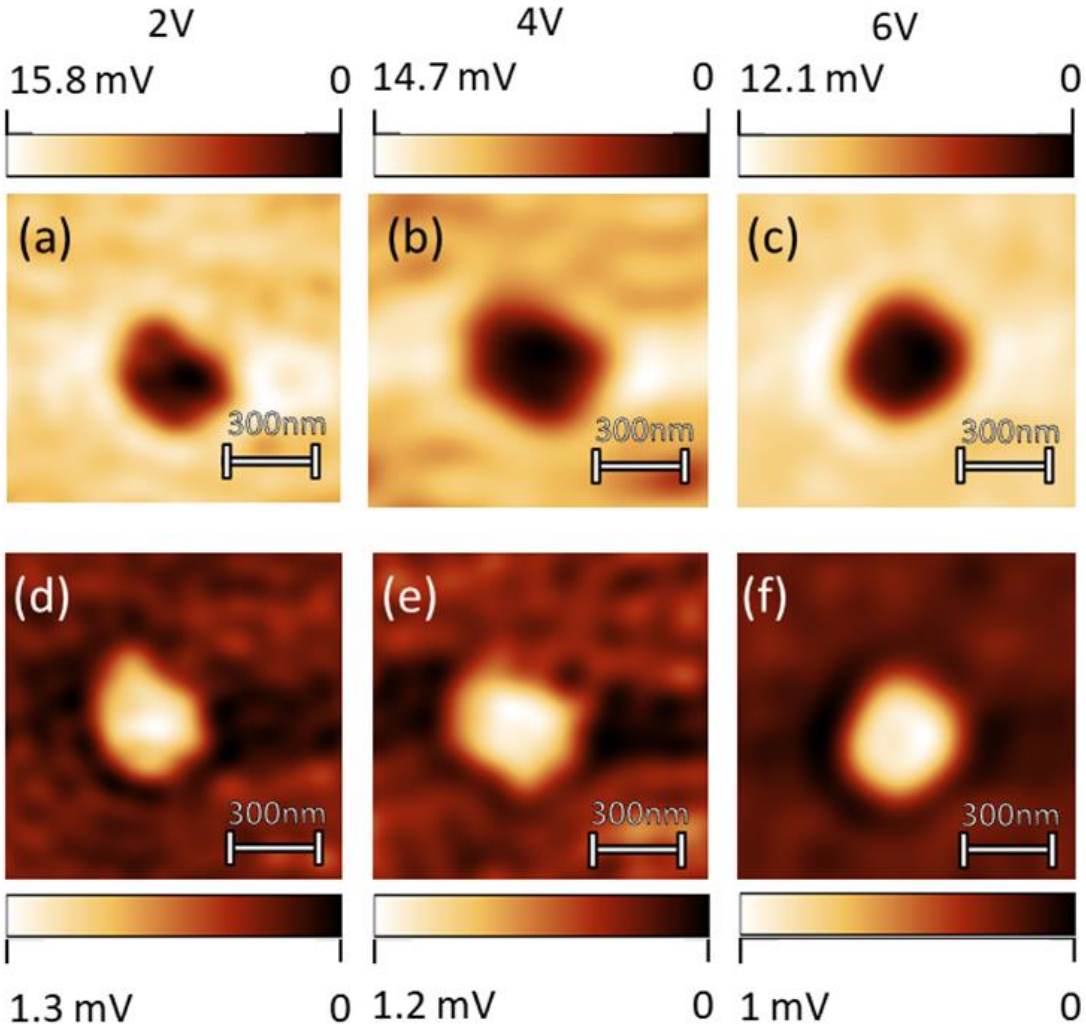

Figure 33: KPFM measurements of a nanoflake with 12nm height. (a)-(c) shows the tip voltage variation for different tip voltage values. (d)-(f) shows the surface potential for different tip voltage values

Considering that STS results are dominated by surface effects, we proceed to a phenomenological description of ferroelectric surface domains in GeS flakes. The integral of the tunneling current curves varies for forward and backward biases. The difference between the integrals is directly proportional to the energy employed to maintain the polarization against the electric field of the tip. Therefore, a physical model can be sketched to explain the behavior of our STS spectra with respect to the polarization field within GeS nanoflakes [148].

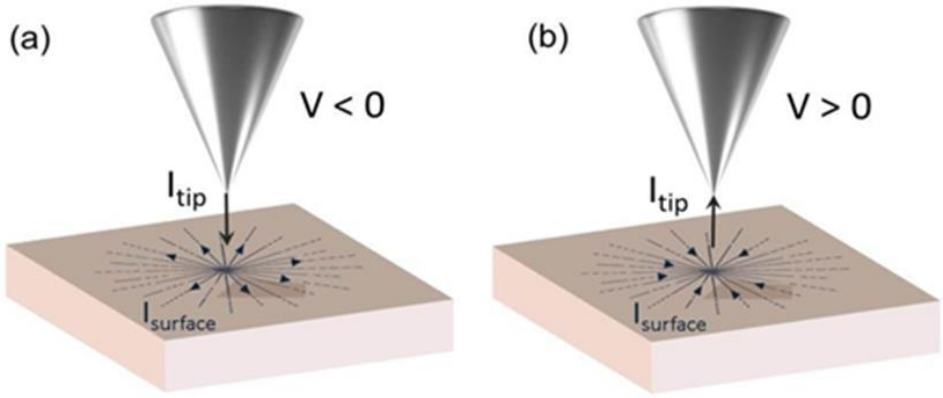

Figure 34: A schematic representation of the experiment, the resulting tunnelling and surface currents are shown in panels (a) for negative tip bias and (b) positive bias.

A representation of the experiment is shown in figure 34. Whereas STS measurements directly impose a tunneling current from the tip to the surface, inducing an out-of-plane electric field, in-plane currents are also induced, as shown in STM works in the literature [149]. However, the measurement is sensitive to changes in surface polarization along the in-plane direction.

The tunneling current is composed by electrons, which tunnel from tip to sample or vice-versa. Each of these configurations depends on the sign of the tip potential. When applying a bias to the tip, an electric field with two components, parallel and perpendicular to the material surface, appears.

The parallel component plays a major role in our system, changing the in-plane polarization. We now discuss the possible mechanism behind the observed in-plane ferroelectricity in GeS. This problem has been addressed in recent reports [148], [150], [151], and the general idea is that the phenomenology may arise from atomic distortions induced by the external field. To recap, the difference in electronegativities between Ge and Se is responsible for a net polarization in a single GeS layer, as suggested by the dipole orientations

indicated in figure 35-(a). For an even number of layers (or in the bulk), centrosymmetric implies antiferroelectricity. This situation is depicted schematically in figure 35-(b). The situation changes upon application of an electric field, which may induce atomic displacements, as indicated in figure 35-(c).

The resulting restructuring has the effect of reorienting the dipoles in the upper layer - the surface becomes polarized, retaining its polarization even when the field is decreased to zero. By reversing the electric field, the mechanism acts again in the upper layers, reversing the polarization through similar atomic distortions. The net result is the surface in-plane ferroelectricity observed in our experiments.

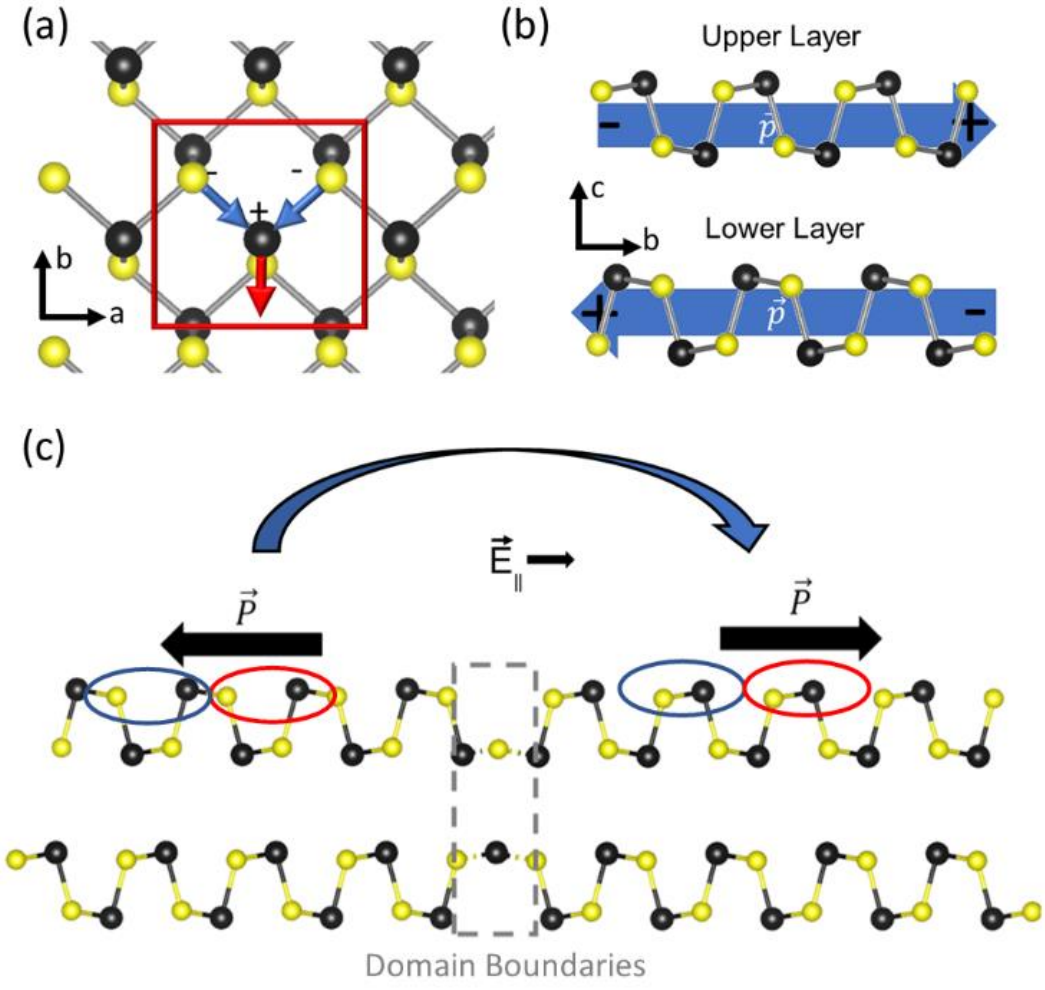

Figure 35: (a) Schematic figure of the electric dipole for the lower layer in the a-b plane. The blue arrows represent the electric dipole formed by Ge (black spheres) and S (yellow spheres)

atoms. The red arrow represents the vectorial sum of blue arrows. In (b) the two layers (lower and upper) that compose the GeS unit cell are shown. Each of these layers has an opposite polarization vector along the b direction. In (c) the scheme of a structural transition induced by parallel electric fields of the STM tip is shown. Blue and red ellipses indicate the change of the bound configuration. A sketched representation of the domain boundaries for different polarization domains induced by the STM tip.

5.7 Conclusions

In summary, we have successfully synthesized and characterized few-nanometer-thick germanium sulfide deposited on a HOPG substrate. Our main result is the description of a surface-induced polarization effect through scanning tunneling spectroscopy at room temperature, which is interpreted in terms of a ferroelectric behavior. The observed hysteretic phenomenology is consistent with a physical mechanism based on in-plane atomic displacements induced by the external electric field.

6 Co-existence of surface electronic confinement and topological signatures in Sb_4Te_3

The second project of this thesis is dedicated to study the electronic properies of the topological layered material Sb_4Te_3. This material consists of a composite stacking of two distinct topological materials: the 3D topological insulator Sb_2Te_3 and the 2D topological insulator Sb_2. Our Angle-Resolved Photoemission Spectroscopy measurements combined with density functional theory reveal that the topological behavior exhibited by Sb_2Te_3 and Sb_2 persists, characterized by electronic states emerging from spin-orbit coupling, hexagonal warping associated with time reversal symmetry and photon-energy independence in these surface states. By comparing results with the complete bulk and surface bands, we observe parabolic states associated with the existence of stacking faults. The photon-energy independence of this state indicates confinement along the stacking direction. Our findings shed light on the unique electronic states and topological properties emerging in Sb_4Te_3.

6.1 Introduction

In recent years, materials exhibiting van der Waals interactions in their stacking configurations have attracted significant attention from the scientific community due to their novel electronic properties and future technological applications [152], [153], [154], [155]. These materials manifest diverse properties, such as enhanced surface electrical conductivity, quantum well states, charge storage capabilities and ferroelectricity [156], [157], [158], [159], [160], [161]. Some of these properties may arise (or be modulated) from alterations in their stacking patterns, holding the promise of novel developments in device technologies [162], [163].

Our focus in this study is the Antimony Tellurite family, specifically Sb_4Te_3, which exhibits a stacking arrangement comprising two quintuple-layers (QL) of Sb_2Te_3 and two bi-layers of Sb_2 [164]. Notably, Sb_4Te_3 consists of both a 3D topological insulator material (Sb_2Te_3) and a 2D topological insulator (Sb_2), rendering it an intriguing subject for investigation

[165], [166]. Despite its potential, Sb_4Te_3 has remained relatively unexplored. The structure of Sb_4Te_3 comprises a complex stacking arrangement denoted as AA'B'ABB'C'BCC'A'C, where ABC and A'B'C' correspond to the stacking sequences of Sb_2 bilayers (BL) and Sb_2Te_3 quintuple layers (QL) respectively. This stacking configuration is illustrated in figure 36, with the conventional unit cell outlined within the black rectangle.

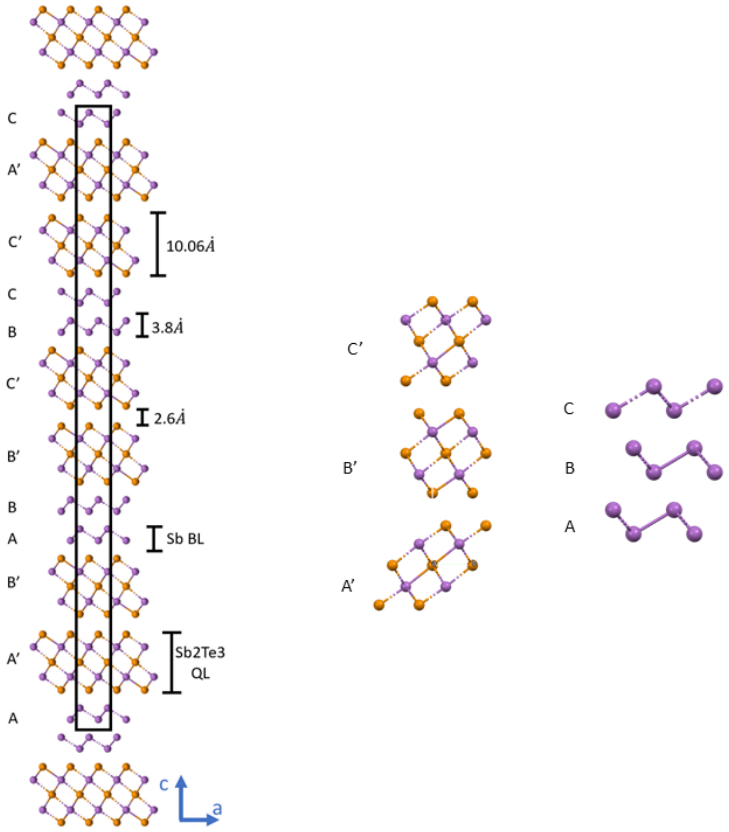

Figure 36: Left: Atomic structure of Sb_4Te_3, illustrating the stacking configuration along with the respective heights of each layer and Van der Waals distances. Center: Stacking of Sb_2Te_3. Right: Stacking of Sb_2.

Utilizing X-ray powder diffraction and crystal truncation rod (CTR) scattering, we determined the occupancy of each phase in surface termination, respectively. Combining these results with STM allowed us to confirm the presence of all possible surfaces.

We conducted ARPES measurements to explore the electronic band properties. Firstly, we conducted ARPES measurements using a helium lamp to characterize the sample and further we performed high-resolution (HR-ARPES) measurements using synchrotron radiation with a micrometer-sized spot and low temperature. Remarkably, our ARPES observations revealed clear signatures that are fingerprints of topological behavior. The presence of surface states, as

confirmed through DFT calculations, displaying hexagonal warping indicates the persistence of time-reversal symmetry. Moreover, the absence of photon-energy dependence in these states confirms their surface nature.

The HR-ARPES results revealed two additional electronic bands distinct from the bulk and surface states. These bands exhibited the same energy dispersion along the Γ-M direction as reported for Sb2 quantum wells [167], [168], [169]. We attributed these bands to an electronically confined state situated in additional Sb_2 surface [170]. This localization behavior was further examined by varying the photon energy, revealing a localized in-plane behavior, as evidenced by the photon-energy independence.

6.2 Growth and Characterization

We have synthesized Sb_4Te_3 using the Bridgman technique, following an established procedure outlined in the literature [164]. The Sb_4Te_3 crystal was obtained using Bridgman technique by mixing the Sb and Te elements in a stoichiometric ratio, using 0.55g of 99.999% pure antimony powder and 0.44g of 99.99% pure tellurium powder. Both materials were put into a quartz tube. The tube was evacuated, sealed and heated to 800°C for four days and then cooled to 500ºC for 36hrs. Sb_4Te_3 crystals were freshly cleaved in-situ before the ARPES and STM measurements presented in this work.

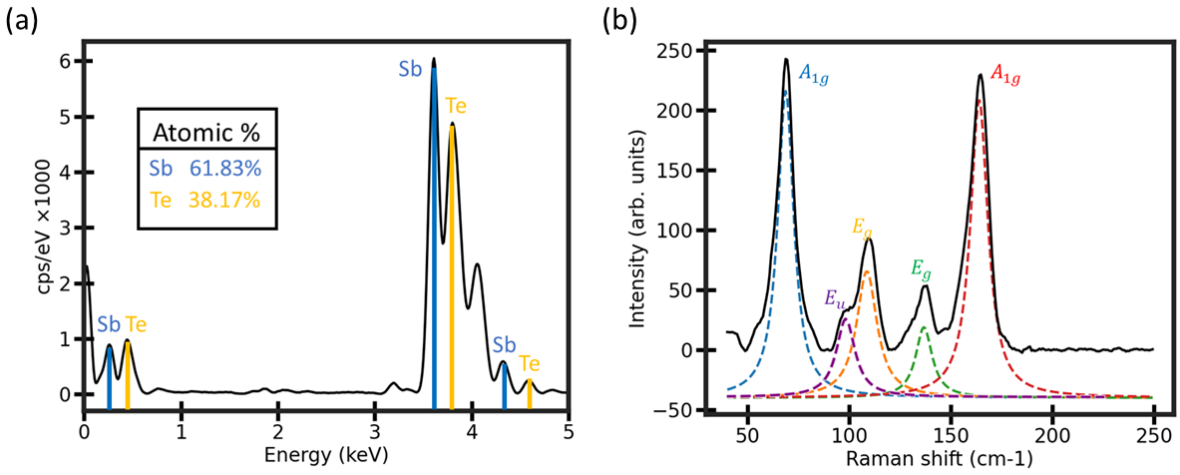

Figure 37: (a) Energy dispersive spectra and (b) Raman spectroscopy of our Sb_4Te_3 sample.

Upon successful synthesis, we characterized the material using EDS to verify the Sb/Te atomic ratio, figure 37-(a). Raman spectroscopy was employed to confirm the structural phase,

figure37-(b). Both Raman and EDS measurements were taken on the same equipment of the first project.

6.2.1 Scanning Tunelling Microscopy

To investigate the surface morphology resulting from these various terminations, we conducted STM measurements. In the STM images, as shown in Figure 38-(a-b), we observe the material surface with distinct steps, which arise from different regions of Sb_4Te_3 and Sb_2.

For both images, a topographic profile was extracted along the white line. In Figures 38-(c-d), the profiles for Figures 38-(a-b) are respectively depicted. It is possible to discern all terminations: Sb_2 with 0.38 nm, Sb_2-Sb_2 with 0.77 nm, Sb_2Te_3 with 1.06 nm, and Sb_2Te_3-Sb_2Te_3 with 2.12 nm. In Figure 38-(d), the profile taken from Figure 38-(b) reveals several steps with the same height value. For this condition, a Sb_2 domain was identified as depicted below.

For a more comprehensive analysis of the surface, we checked step heights from several STM measurements. A histogram was constructed to evaluate the relative percentage of each termination and is shown in Figure 38-(e). For all four terminations, height values within ±0.2 nm of the main value for a specific termination were considered. The histogram reveals that the majority of the surface is terminated with Sb_2, which could be expected given the coexistence of Sb_4Te_3 and Sb_2 phases.

The distribution of terminations obtained is as follows: 18.7% Sb_2, 58.0% Sb_2- Sb_2, 17.0% Sb_2Te_3, and 6.3% Sb_2Te_3-Sb_2Te_3. The observed domain sizes range from approximately 50-200 nm. This information is crucial, as it allows us to anticipate the convolution of the ARPES beam spot across different terminations. A thorough understanding of these surface features is pivotal for a comprehensive characterization of the material's electronic properties. In figure 38-(f) a scheme of the possible surface terminations for Sb_4Te_3 is depicted. STM measurements was collected on Omicron VT-STM scanning tunneling microscope/spectroscope operating at 1.7×10^{-10} mbar at room temperature.

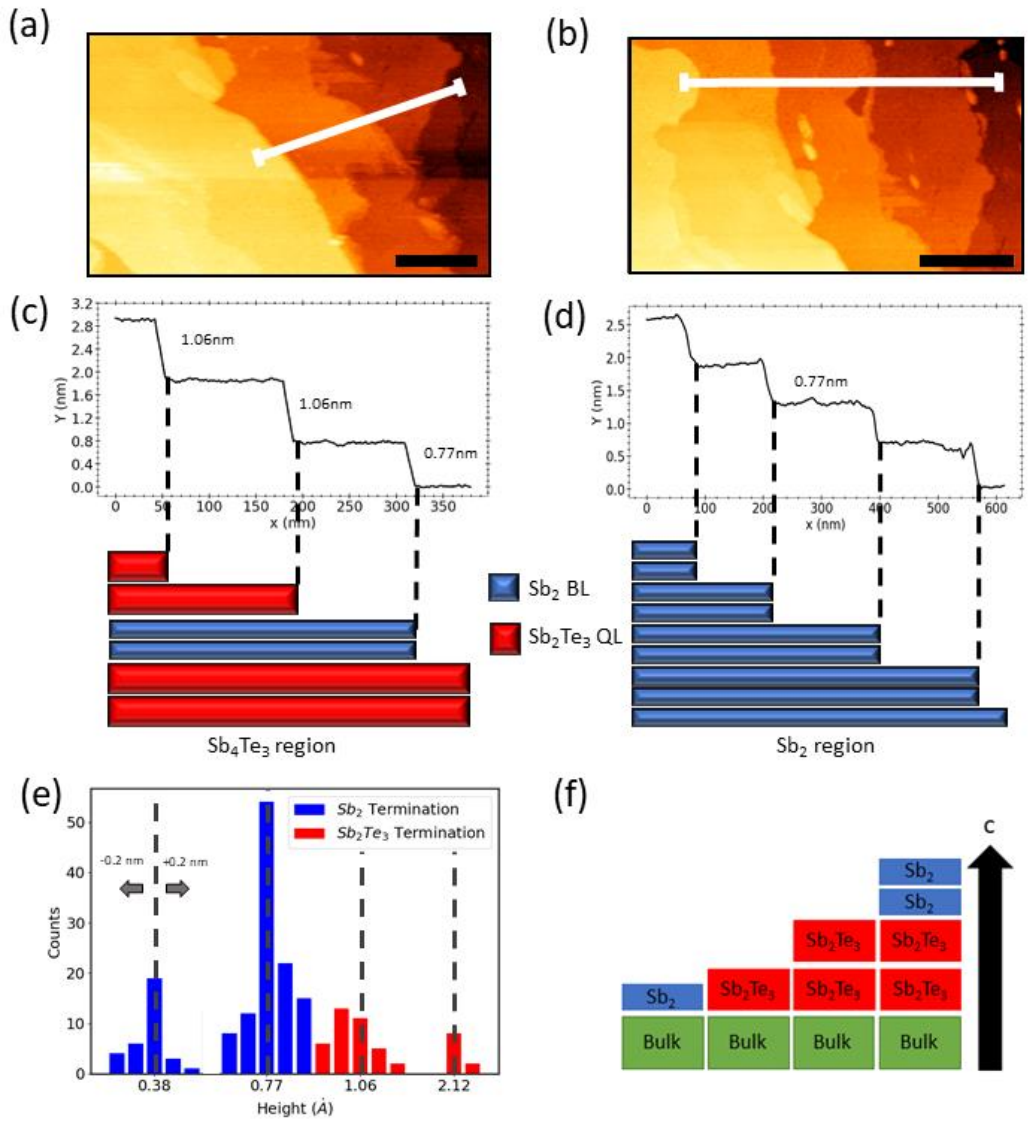

Figure 38: STM images of different regions on our sample. In (a) Sb_4Te_3 region and (b) Sb_2 region. Distinct steps created by different terminations are observed. Both images were acquired with a tunneling current of 500 pA and a tip bias of 1V. The black scale bars measure 150 and 200 nm, respectively. (c) The topography profile along the white line in (a) reveals height values in agreement with the Sb_4Te_3 possible terminations. A comparison with these terminations is depicted below. The blue rectangles represent the Sb_2 BL termination, and the red rectangles the Sb_2Te_3 QL termination. (d) The topography profile along the white line in (b). (e) A histogram of all height values found in different regions of our sample. The blue bars are associated with Sb_2 termination, and the red bars with Sb_2Te_3 terminations. (f) Schematic of Sb_4Te_3 stacking configuration showing the possible surface terminations.

6.2.2 Crystal Truncation Rod

A correlation between surface and bulk composition can be drawn by measuring powder X-ray diffraction (bulk sensitive) and Crystal Truncation Rod (CTR) scattering (surface sensitive). Fig.39-(a) shows XPD measurements and fits associated to crystal phases from crystallographic databases while Fig.39-(b) shows a CTR acquired along the (00L) direction and fits changing the surface composition.

One observes in Fig.38-(a) that the XPD profile is easily described as a combination of Sb_4Te_3 (71%) and Sb_2 (29%) obtained using MAUD software [140]. This measurement is representative of the bulk composition and phases in the sample. The two major phases needed to fit the data are displayed (red and blue curves for Sb_4Te_3 and Sb_2, respectively). Additional phases (Pure Te and other Sb_nTe_m-type phases), which correspond to less than 1%, were not included in the fit. Peak intensity differences arise from sample texture and cannot be fitted by any additional phase.

In order to access the most relevant surface terminations, CTR measurements were performed at EMA beamline of the Brazilian Synchrotron Light Laboratory Sirius (Campinas). We looked for possible surface stabilization in which the composition differs from the bulk XPD result. CTR measurements were simulated using the formalism introduced by Robinson et. al [171]. In this model, the CTR intensity is related to the roughness (σ), absorption (β) and out-of-plane lattice parameter (c) and expressed as a function of the momentum transfer vector q along the (00L) direction as:

$$A_{CTR} = \frac{A_0}{1 - e^{iqc}e^{\beta}}\left[\frac{(1-\sigma)^2}{1+\sigma^2 - 2\sigma\, cos\, qc}\right]^{\frac{1}{2}}. \quad (86)$$

The sample studied here was modeled as bulk Sb_4Te_3. Surface layers, which can be Sb_2 BL or Sb_2Te_3 QL, exhibit distinct electronic density profiles, giving rise to asymmetries in the diffuse diffraction signal in the measured CTR range. Combinations of these surface layers were modeled separately, with their atomic stack described as a list of atoms and coordinates, interfering with the diffraction intensity due to modified scattering amplitudes. Such effect is expressed in equation (87), where N is the number of atomic layers along the surface normal direction at the simulated surface, Z_j is the atomic number for each atom stacked above the bulk Sb_4Te_3, $f_j(q)$ is the atomic scattering factor of the atomic layer j and r_j is the atomic layer

position with respect to the first crystalline layer above the bulk crystal termination (fixed at $r = 0$ here),

$$A_{layers} = A_1 \sum_{j=1}^{N} Z_j f_j(q) e^{i\mathbf{q}\cdot\mathbf{r}_j}. \quad (87)$$

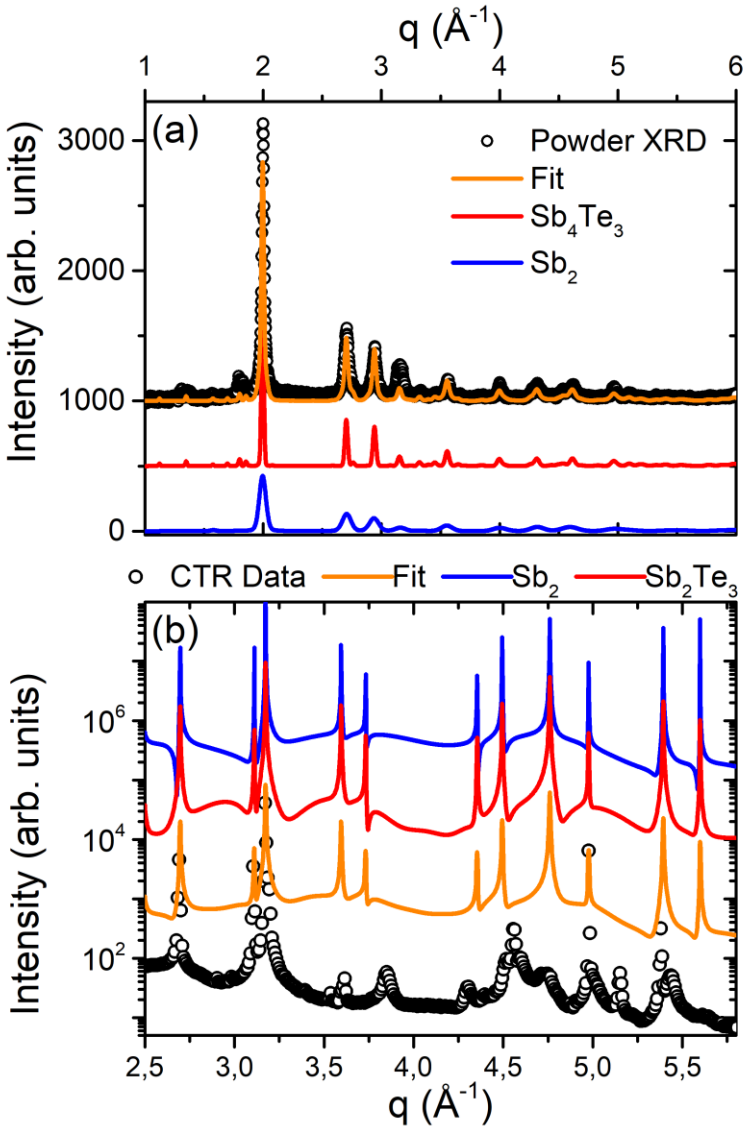

Figure 39: (a) X-ray powder diffraction measurements (dots) and fits (lines) obtained from Rietveld refinement of our bulk (ground to powder) crystal, showing major contributions from Sb_4Te_3 and Sb_2 phases (71% and 29%, respectively). (b) X-ray crystal truncation rod scattering measurements (dots) and simulations (lines) for the two most relevant surface terminations: a double Sb_2 surface layer (blue) and a single Sb_4Te_3 layer (red). The best combination of four surface terminations (discussed in the text) lead to the orange curve.

Finally, the measured intensity is obtained as the square of the sum of the intensities of equations (86) and (87), as depicted in equation (88),

$$I = \left|A_{CTR} + A_{layers}\right|^2, \tag{88}$$

where A_{CTR} accounts for the bulk Sb_4Te_3 crystal and A_{layers} represents the surface atomic stack.

XPD measurements were carried out in a Panalytical Empyrean system, equipped with a two-dimensional detector and a Cu K-alpha source (LabCri-UFMG). Samples were finely grinded and measured in the range from 4° to 150°. The region with strongest peaks was then analyzed throughout the Maud Rietveld package using reference crystallographic data for Sb_2 and Sb_4Te_3 crystals. CTR measurements along the (00L) direction were carried out at the EMA beamline of the Sirius synchrotron (Campinas, Brazil). The beamline is equipped with a 6-circle diffractometer and a Pilatus 300K detector. We have used a 9.6 keV monochromatic beam focused by KB mirrors to a 20 x 20 μm^2 spot at the sample position. Sb_4Te_3 crystals with a well determined surface, with a plane facet perpendicular to the (001) direction was freshly cleaved and aligned with the X-ray beam. The beam was moved laterally by hundreds of microns and the (00L) CTR was measured 4 times, yielding similar results.

Surface layers are modified using distinct stackings of Sb_2Te_3 and Sb_2. In particular, the CTR data has been fitted with a combination of four distinct surface terminations: (i) Sb_2 - Sb_2, with 2 Sb_2 BL at the surface; (ii) Sb_2 - Sb_2 - Sb_2Te_3 with a single Sb_2Te_3 QL at the surface; (iii) Sb_2Te_3 - Sb_2Te_3 - Sb_2 with a single Sb_2 BL at the surface and; (iv) Sb_2 - Sb_2Te_3 - Sb_2Te_3 with a double QL at the surface. The list provided above is ordered as a function of the layer stack relevance to the CTR fit. Fig. 39-(b) shows the simulated CTR profile for terminations (i) and (ii). In order to obtain the fit depicted by the orange curve (the closest to the characteristics of our measured profile) we combined the following surface fractions: 43% of Sb_2 double BL termination, 26% of single Sb_2Te_3 QL termination, and 17.5% and 13.5% of the surface terminate in Sb_2 BL and Sb_2Te_3 double QL, respectively. It is important to state that all out-of-plane (c-axis) lattice parameters used for surface simulations were increased by 1% with respect to bulk values. Such amount holds for both Sb_2 and Sb_2Te_3 surface layers.

A closer look to the results discussed above indicates that 60% of the surface is occupied with an Sb_2 BL termination (1 or 2 bilayers) while 40% ends up in Sb_2Te_3 quintuple layers. Since the synchrotron X-ray CTR spot illuminates an area similar to the ARPES spot size, we

believe these numbers are representative to what is observed using the latter technique. STM/STS data are clearly more local and may present some deviation from these values.

6.3 ARPES Measurements of Sb_4Te_3

We conducted a series of HR-ARPES measurements at the Bloch beamline of MAX-IV Laboratory to explore in more details the electronic band structure of Sb_4Te_3. First, measurements were carried out using a photon beam size of 16×9 μm², with photon energy of 73 eV at a temperature of 19 K.

The bulk structure of Sb_4Te_3 calculated using DFT is depicted in Figure 40-(a). The bulk has a trigonal unit cell with the stacking along the (111) direction. We can observe 3 relative gaps at the Γ point below the Fermi level ranging from -0.1 eV to -0.2 8eV, -0.3 eV to -0.55 eV and -0.6 eV to -0.95 eV. Looking at the energy range from 0 eV to -1 eV of the bulk band structure, it is possible to observe an electronic state at the L point, but no electronic states at the S_0 point. By projecting the bulk reciprocal space at the surface, the bulk L position corresponds to the M point in the surface reciprocal space. Correspondingly, the bulk S_0 point corresponds to the surface K point.

Comparing the ARPES spectra with the band structure, we can identify the spectrum in the momentum direction along M-Γ-M (Figure 40-(b)) and the corresponding spectrum along the K-Γ-K (Figure 40-(c)). In both cases, comparing the spectra with the theoretical band structure, it is possible to observe two V-shaped bulk bands at the Γ point, with binding energies of 0.3eV and 0.8 eV.

ARPES measurements were collected at two synchrotron beamlines. The characterization was performed at the SAPE end-station at SIRIUS (Campinas, Brazil) on a SPECS PHOIBOS 150 spectrometer. The sample was kept at 80 K in an ultra-high vacuum chamber with pressure better than 2×10^{-10} mbar.

The high-resolution ARPES data were acquired at the HR-ARPES end-station of the Bloch beamline, at MAX IV Laboratory (Lund, Sweden). The end-stsation is equipped with a Scienta DA30-L analyzer and a 6-axis cryo-manipulator. The sample was kept at 18 K using a He cryostat coupled to a low-vibration closed-cycle cooling engine, Stinger from Coldedge.

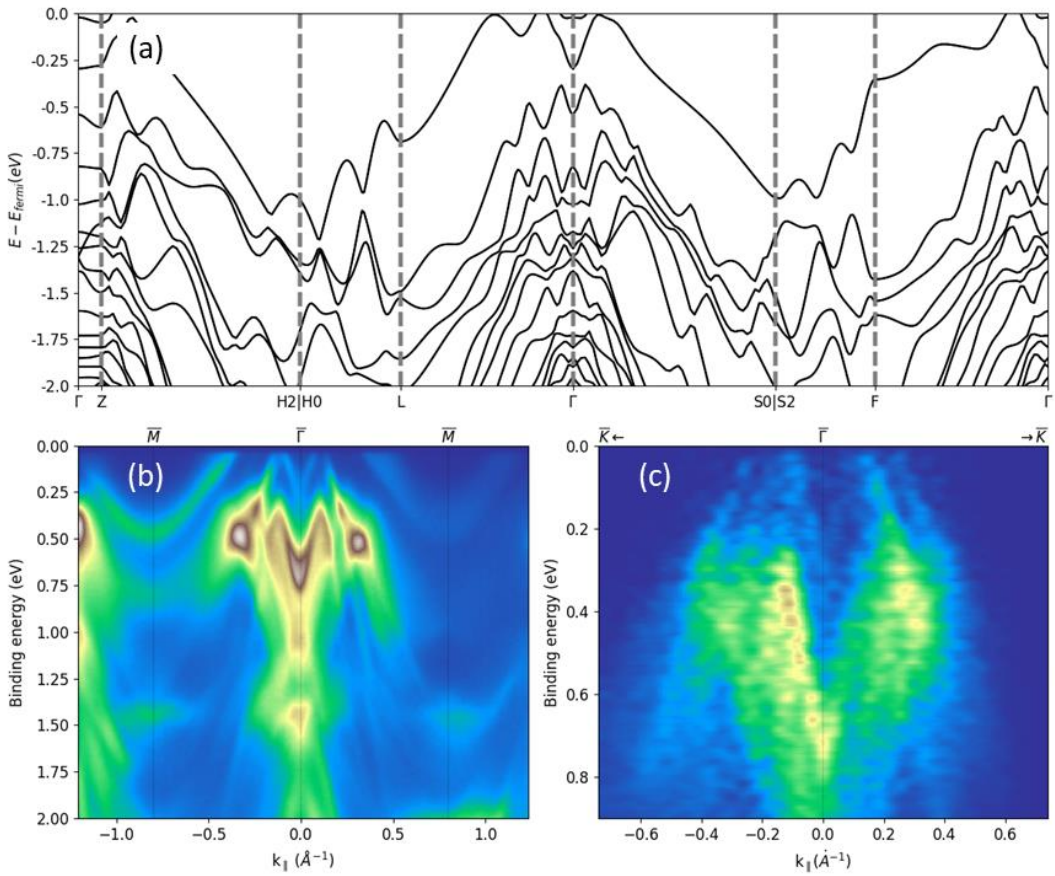

Figure 40: (a) Calculated bulk electronic band structure of Sb_4Te_3. By projecting the bulk reciprocal space at the surface, the bulk L position corresponds to the M point in the surface reciprocal space. Correspondingly, the bulk S_0 point corresponds to the surface K point. ARPES measurements of Sb_4Te_3 at 19 K with a photon energy of 73 eV at (b) M-Γ-M direction and (c) K-Γ-K direction.

6.3.1 Topological Signatures from Surface States

The fact that Sb_4Te_3 consists of a stack of two different topological insulators suggests that it can exhibit complex topological properties. Other materials with similar structures possessing topological order have been reported in the literature [172], [173], [174]. Topological materials exhibit specific features such as hexagonal warping (due to the preservation of time reversal symmetry) and surface states originating from spin-orbit coupling

which leads to a lack of dependence of the surface bands on photon energy and the creation of topological surface states (TSS) [88], [166], [175]. These signatures are observed in Sb_4Te_3.

The electronic structure of Sb_4Te_3 for Sb_2 terminations is then calculated. Figure 41-(a) illustrates the two possible configurations of the surface termination with Sb_2. We first performed DFT calculations to determine the band structure of Sb_4Te_3 with the Sb_2Te_3-Sb_2 termination. The computational details will be at the end of this chapter. To elucidate the role of spin-orbit coupling, we computed this band structure both without spin-orbit coupling, shown in Figure 41-(b), and with spin-orbit coupling, depicted in Figure 41-(c).

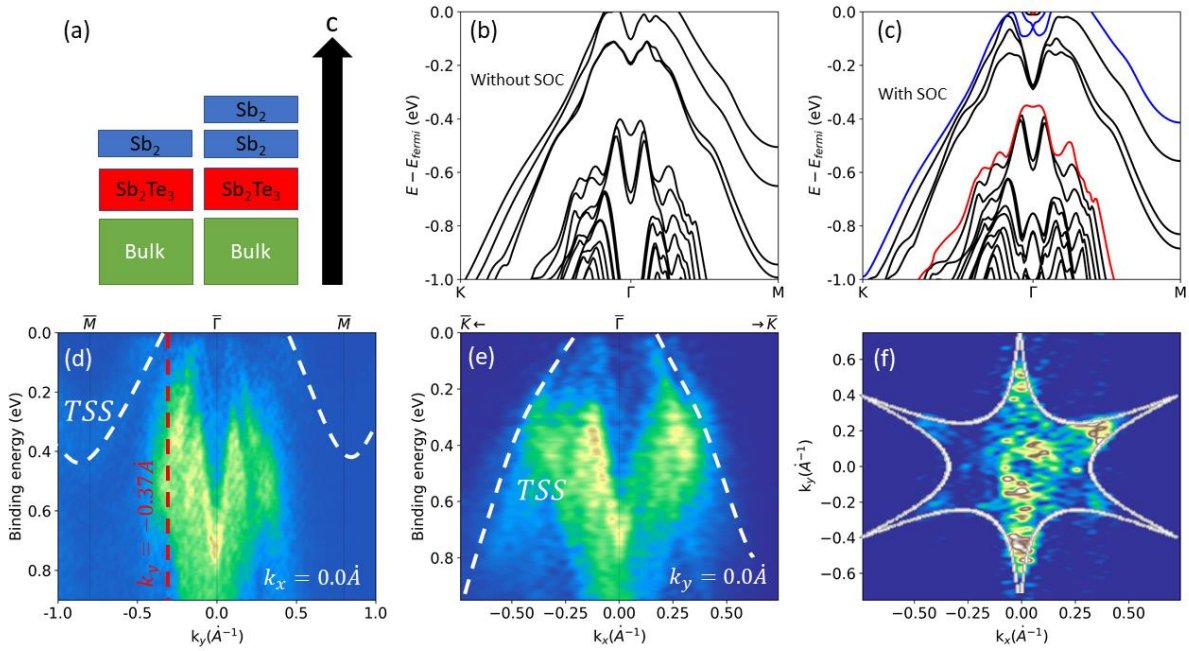

Figure 41: (a) Schematics of the two different Sb_2 terminations of Sb_4Te_3. The electronic band structure for the Sb_2 BL termination is presented without (b) and with spin-orbit coupling (c). The blue line is a surface state that emerges from the spin orbit coupling, where a Dirac cone is evident at -0.1 eV. The red lines are other surfaces states. These ARPES measurements were conducted at 73 eV. In (d), a cut at $k_x = 0.0\ \dot{A}^{-1}$ is depicted, revealing the topological surface state indicated by the white dashed line. The red dashed line represents the value of $k_x = -0.37\ \dot{A}^{-1}$ where this TSS intersects the Fermi level. In (e), a cut at $k_y = 0.0\ \dot{A}^{-1}$ is presented. In (f), the Fermi surface exhibits a snowflake pattern for the TSS.

In Figure 41-(c), we present both the bulk bands (in black) as well as the topological surface state (blue lines), and other surface states (red lines). Although through ARPES we do not have direct access to the Γ point for this band, DFT calculations allow us to discern its

topological nature. It is apparent that a state with a Dirac cone appears at 0.1 eV below the Fermi level, illustrated as the blue line in Figure 41-(c). Such behavior is commonly observed in topological systems. By comparing this band structure with the bulk one, we note that this state arises due to the disruption of periodicity at the surface and the SOC interaction.

Now, we compare DFT calculations with our ARPES measurements. The first observation is that the calculated Fermi level is slightly higher than observed in the data. Consequently, the Dirac cone predicted in Figure 41-(c) is not evident in the ARPES data, as shown in Figures 41-(d-e). However, a remaining feature of the Dirac band is observed. In Figure 41-(d), we present a cut at $k_x = 0.0\ \dot{A}^{-1}$ representing the M-Γ-M path. By comparing the band dispersion along this path with the calculations, we clearly observe the topological surface state originating from the Fermi level, touching the M point at around 0.42 eV.

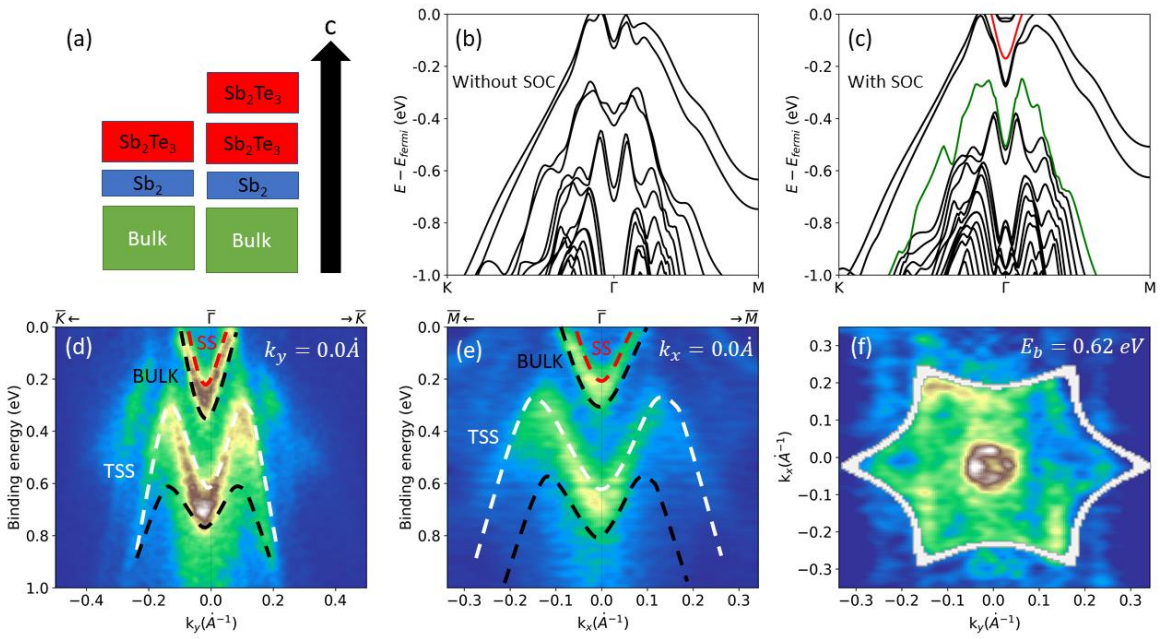

Figure 42: (a) Schematic representation of the two different Sb_4Te_3 terminations in Sb_2Te_3. The electronic band structure for the Sb_2-Sb_2Te_3 termination is presented without (b) and with (c) spin-orbit coupling. The red and green lines are surface states that emerge from the spin-orbit coupling. Two Dirac cones appear at the Γ point. ARPES measurements conducted at 18.8 eV. In (d), a cut for $k_y = 0.0\ \dot{A}^{-1}$ is depicted, revealing the topological surface state indicated by the white dashed line. In (e), a cut for $k_x = 0.0\ \dot{A}^{-1}$ is presented. In (f), the constant energy contours for $E_B = 0.62$ eV exhibits a snowflake pattern for the TSS as well.

Topological surface states emerge from spin-orbit coupling, requiring the preservation of time reversal symmetry. This preservation, together with the reduced surface symmetry of the crystal, results in a sixfold symmetrical pattern, giving rise to a snowflake shape [88]. This is called hexagonal warping, indicating the strength of the spin-orbit coupling. The observed TSS band intersects the Fermi level, indeed creating a snowflake-like pattern on the Fermi surface, as illustrated in Figure 41-(f). Using the equation 17 for a fixed energy, we fitted these data using the model described in equation 89,

$$1 = A\sqrt{k^2 + \lambda^2 k^6 cos^2(3\theta)}, \quad (89)$$

where A is a measure of the $k_x - k_y$ plane size, k is the electron crystalline momentum in modulus, λ is a hexagonal warping parameter, and θ is the azimuth angle with respect to the Γ-K direction. Using equation 89 to fit the free parameters, we obtained $\lambda = 38.23\ \dot{A}^2$ and $A = 1.74\ \dot{A}$ for the topological surface states in Figure 41-(f).

A different scenario emerges when Sb_4Te_3 terminates in Sb_2Te_3, as depicted in Figure 42-(a). We calculated the band structure for both possibilities and surface states appear in similar regions. For short, we discuss the case involving the Sb_2-Sb_2Te_3 termination. Upon comparing the calculations without spin-orbit coupling, shown in Figure 42-(b), and with spin-orbit coupling, which is depicted in Figure 42-(c), surface states become evident. These states are represented in the figure by green and red lines. The TSS exhibits a Dirac cone at the Γ point, located at -0.56 eV. It is crucial to note that, for Sb_4Te_3 bulk, there exists a relative gap at the Γ point ranging from -0.38 eV to -0.58 eV.

The TSS band manifests within this relative band gap, establishing a connection between the upper and lower bulk bands. This can be observed in the ARPES data collected with a photon energy of 18.8 eV, as shown in Figure 42-(d-e). A distinctive Dirac cone emerges at binding energy of 0.60 eV, delineated by the dashed white line. Upon comparison with the band structure, this observed cone aligns precisely with the energy level (0.32 eV) where the upper bulk bands reach their lower energy values, as indicated by dashed black lines. This alignment demonstrates excellent agreement with the band structure from DFT calculations. Despite the presence of mixed bulk bands and TSS, this distinctive behavior effectively each band.

To confirm the correlation of this band with a strong spin-orbit coupling, a cut at a binding energy of 0.62 eV is depicted in Figure 42-(f). We observe both a snowflake pattern as

well as a circular pattern at the Γ point. Both the snowflake and circular patterns stem from the same TSS state. Using equation 89 to fit this pattern, we found $\lambda = 32.63\ \dot{A}^2$ and $A = 4.22\dot{A}$ for the topological surface states in Figure 42-(f).

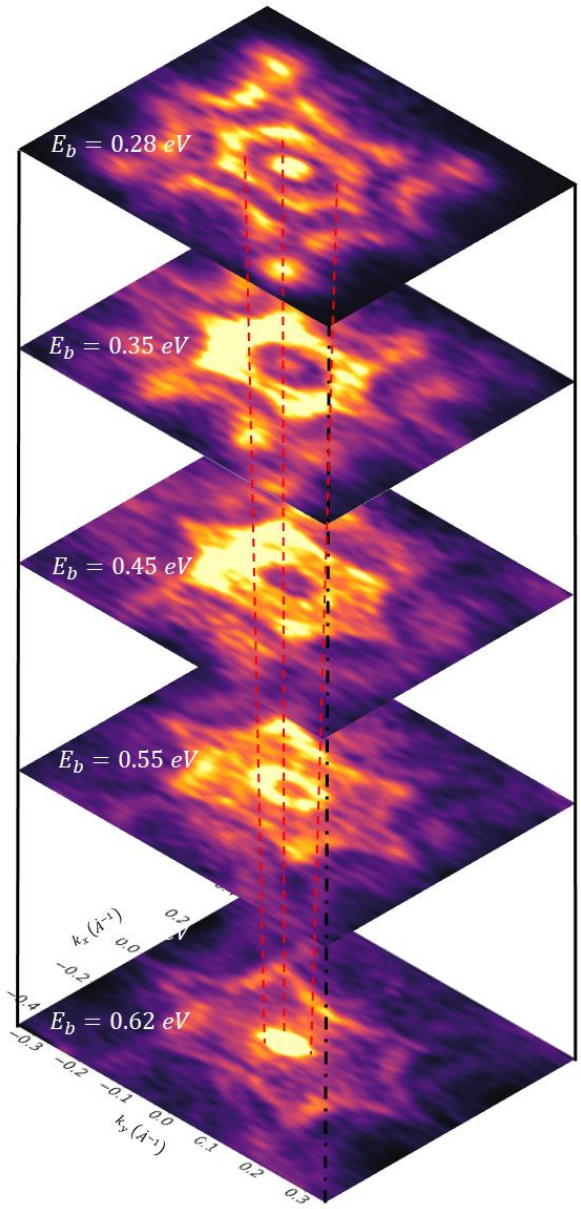

Figure 43: Constant energy contours at different binding energies showing the transformation of the circular pattern from the Dirac cone to a snowflake pattern. The cuts in energy are: 0.62 eV, 0.55 eV, 0.45 eV, 0.35 eV and 0.28 eV. The HR-ARPES photon energy is 18.8 eV

This snowflake pattern is a result of the hexagonal warping, signifying a strong spin-orbit coupling. The circular pattern corresponds to the Dirac cone. To track the evolution of this

band in the Brillouin zone, we performed multiple constant energy contours (CEC), observing the transformation from the circular pattern of the Dirac cone to the snowflake pattern, as shown in Figure 43.

From an energy level of 0.62 eV, the circular pattern at the Γ point, indicative of the Dirac cone, becomes discernible. With a decrease in energy, this circular pattern progressively moves away from the Γ point, as observed in the CEC at 0.45 eV. Upon reaching its lower energy values, $E_b = 0.28$ eV, the circular shape transforms into a hexagonal pattern.

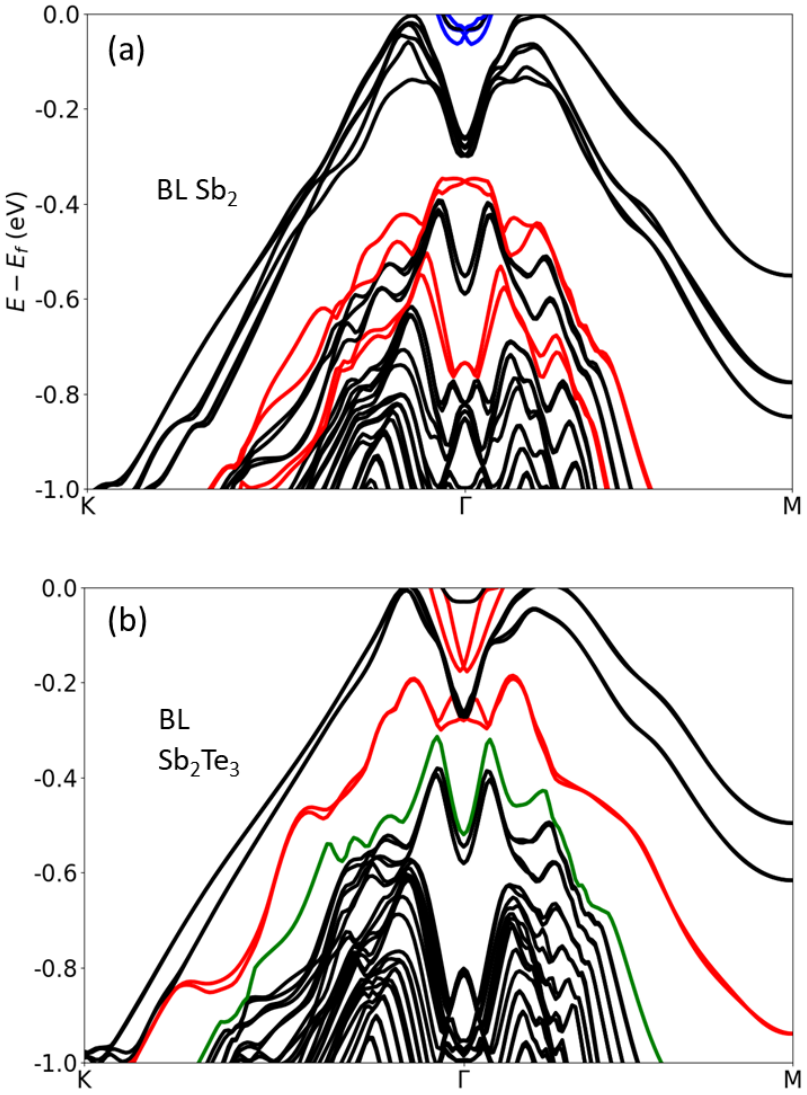

Figure 44: Band structure of Sb_4Te_3 terminated in (a) Sb_2-Sb_2 and (b) Sb_2Te_3-Sb_2Te_3. The red lines are surface states in both cases. The blue and green lines are topological surface states.

For higher binding energy values, the persistence of the hexagonal shape is noticed. An examination of the band structure derived from both DFT and ARPES measurements reveals the presence of both Dirac cone and the remaining band for these energy values. The Dirac cone is modified into a circular shape (near the Γ point), while the residual band adopts a hexagonal one (further away from the Γ point).

The calculated band structure of the termination with two Sb_2 BL's and two Sb_2Te_3 QL's is shown in figure 44. In this case, the same TSS's appears, but with additional surface states that are not associated with topological order.

Through ARPES measurements, the distinction between localized states, such as surface or confined states, and delocalized states (bulk states) can be drawn. This determination is carried out by varying the photon energy to access the perpendicular component of the electron momentum. For states localized in the c-axis direction, the perpendicular component remains delocalized, indicating its independence from photon energy. ARPES measurements were systematically conducted using different photon energies. In Figure 45 we show measurements for 67 eV, 71 eV and 76 eV. Analysis of these measurements reveals that the topological surface states stemming from both Sb_2 and Sb_2Te_3 terminations, denoted by white dashed lines, exhibit no variation in momentum and binding energy with photon energy. Such behavior indicates that these are topological surface states.

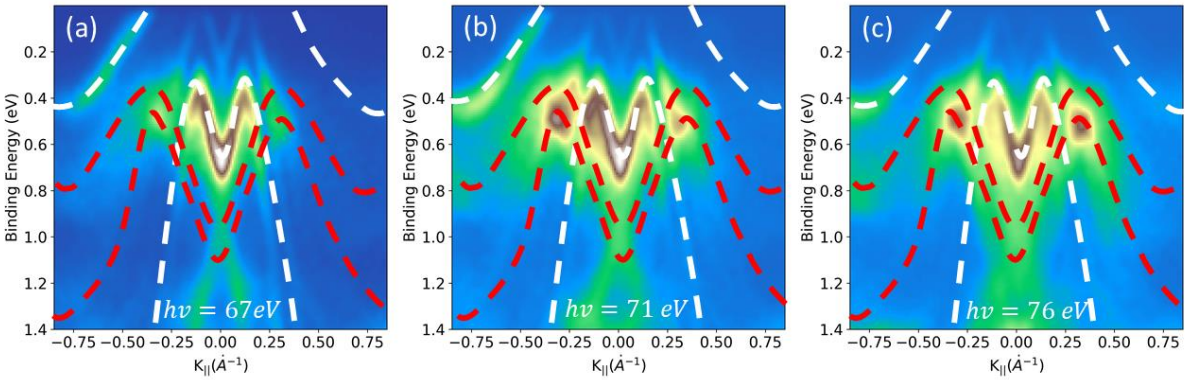

Figure 45: ARPES measurements for differents photon energy values: (a) 67 eV, (b) 71 eV and (c) 76 eV. The white dashed lines are topological surface states and the red dashed lines are quantum well states.

An additional observation from Figure 45 can be drawn from two bands, marked by red dashed lines, which exhibit minimal variation across different photon energies. This behavior implies that these states are localized in the c-direction. It is noteworthy that they are not

observed in DFT calculations across all four terminations of Sb_4Te_3. The next section is dedicated to elucidate their origin.

6.3.2 Confined Electronic States

In Figure 40-(b), two distinct bands emerge at the M point at approximately 0.8 eV and 1.4 eV. Remarkably, as shown in Figure 45, the positions of these bands remain unaffected upon photon energy changes, indicating a localized behavior along the c-direction (the stacking direction of Sb_4Te_3). Our X-ray and STM results reveal the existence of domains comprising both Sb_4Te_3 and Sb_2 within the sample. The ARPES beam spot size is sufficiently large to encompass these distinct domains, rendering ARPES measurements a sum of signals from these domains.

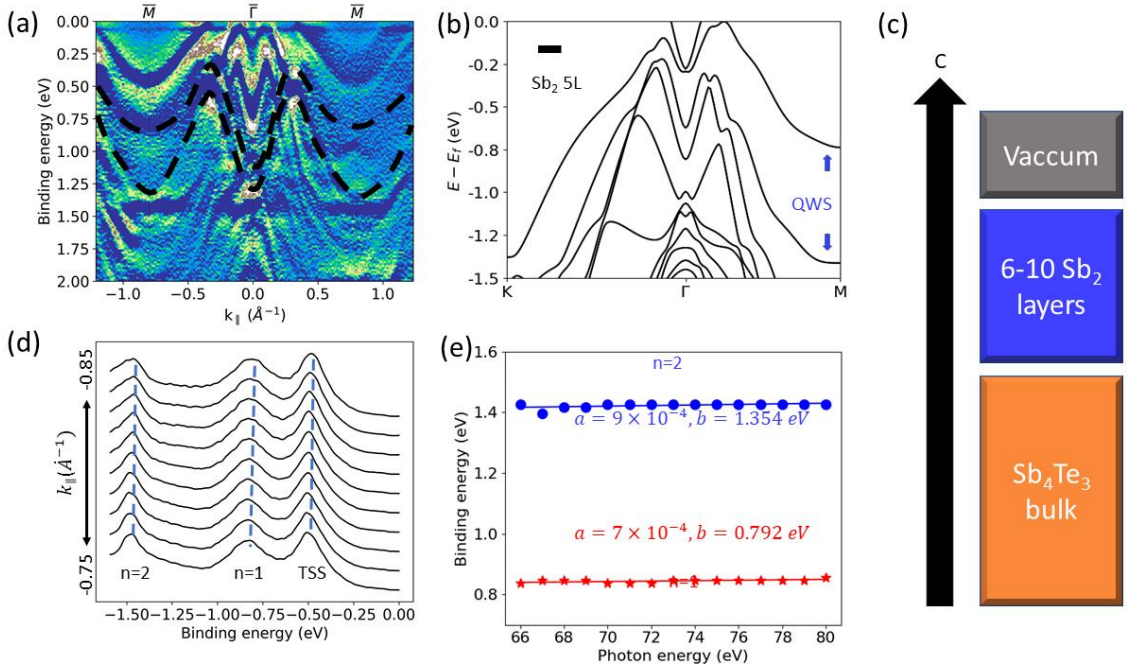

Figure 46: (a) ARPES data treated by the curvature method for the M-Γ-M direction, with two black dashed lines representing quantum well states. (b) Calculated band structure of 5 layers of Sb_2 showing the quantum well states. (c) Model to explain the quantum well formed by Sb_4Te_3, Sb_2 and vaccum. (d) Energy dispersion around the M point showing the surface state and two quantum well states (for n =1 and n=2). (e) Photon energy dependence of these states for n=1 and n=2 from (d).

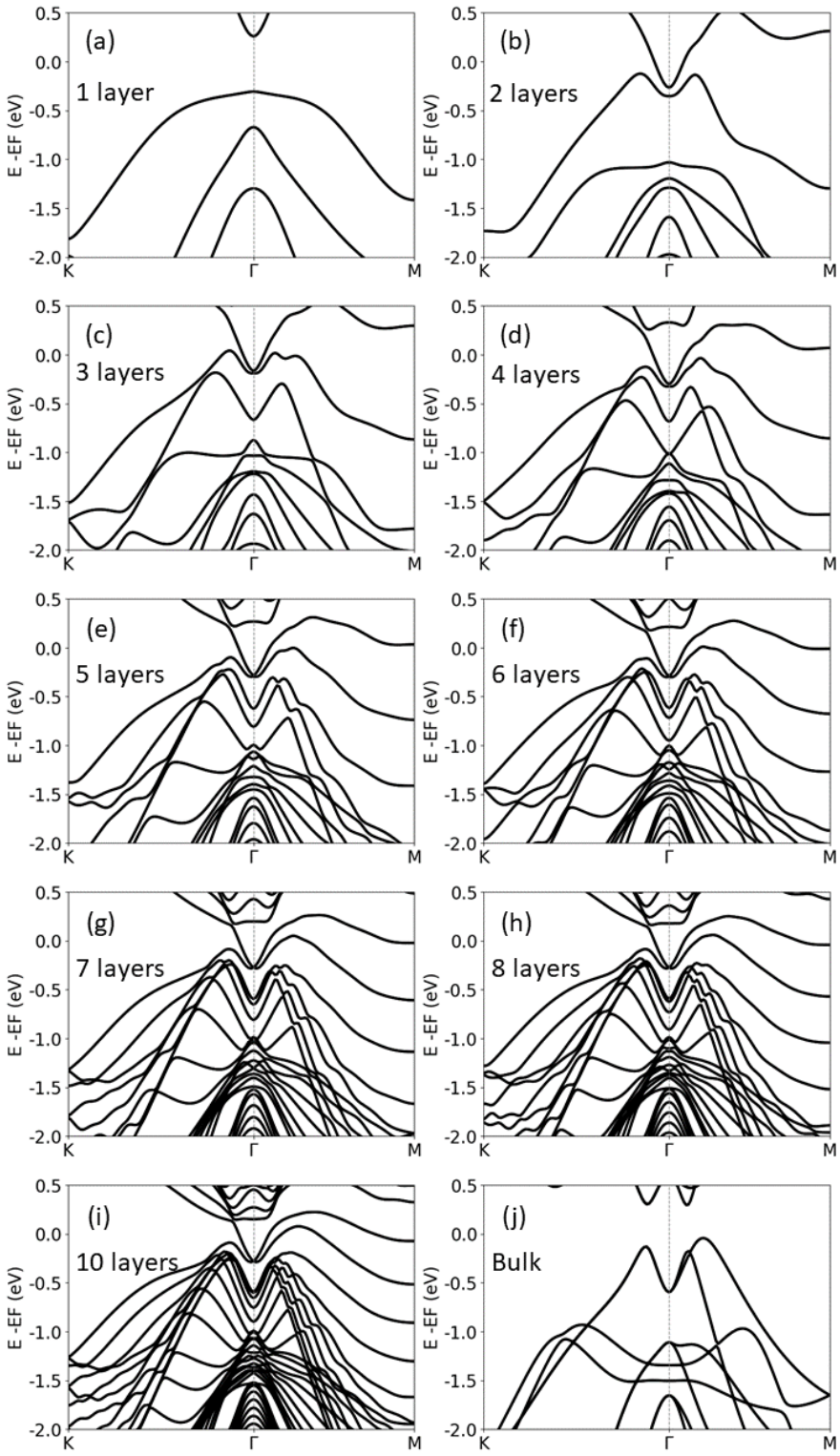

Figure 47: Band strucure of diferent staking configuratios of Sb_2: (a) 1 layer, (b) 2 layers, (c) 3 layers, (d) 4 layers, (e) 5 layers, (f) 6 layers, (g) 7 layers, (h) 8 layers, (i) 10 layers and (j) bulk.

Upon closer inspection of the ARPES data along the Γ–M direction, and employing the curvature method for enhanced visualization [176], the two bands (depicted by black dashed lines in Figure 46-(a)) become apparent. Notably, these bands exhibit an energy dispersion similar to that reported in the literature for Sb_2 quantum wells [167], [168], [169], [177].

In fact, the parabolic dispersion at M point is characteristic of few-layer Sb_2 for over five layers, as shown in the the band structure presented in Figure 46-(b) for the five-layer case. Also, this can be clearly verified in the results of a series of calculations presented in Figure 47, in which we show the evolution of the parabolic bands with the number of Sb_2 layers. This indicates that, most probably, our sample contains stacking faults produced during the growth process, which allows us to ascribe these two electronic states to confined electrons in a few-layer antimony system that may exist above Sb_4Te_3.

A refined analysis at the M point allows the distinction of the surface state arising from the Sb_2 termination and the two states emanating from the quantum well, as shown in Figure 46-(d). The intensity of the quantum well band is notably enhanced at $k_{\parallel} = \pm 0.37 \dot{A}^{-1}$ and at a binding energy of 0.35 eV. Several factors, such as matrix elements or higher electron concentration at this specific energy and momentum could account for this phenomenon. It is well-known that antimony has an anisotropic spin-orbit coupling which leads to a difference for positive and negative electronic momenta [178].

To explore the localized behavior of the confined state, a series of HR-ARPES measurements was conducted varying the photon energy from 66 to 80 eV. Given that this quantum well is confined within the $k_x - k_y$ plane, the parallel momentum component must remain constant. Consequently, a broad range of perpendicular momentum component values can satisfy this condition. In real space, the quantum well state is confined along the c direction. This property leads to a non-dependence on photon energy of this electronic band. Specifically focusing on the states corresponding to quantum numbers n=1 and n=2, their response to variations in photon energy is shown in Figure 46-(e). Notably, minimal variations of these states with respect to photon energy are seen, confirming the localized nature of these electronic states.

We use the Quantum ESPRESSO software package to perform DFT calculations [179]. The calculationsutilize the Perdew-Burke-Ernzerhof (PBE) generalized gradient approximation

(GGA) of the exchange-correlation potential [180], with fully-relativistic effects included in the pseudopotential to account for spin-orbit coupling effects. A plane wave cutoff of 50 Ry was used for wavefunctions, and a 5-mRy of smearing (using the Marzari and Vanderbilt's scheme) was employed to numerically smooth out the metallicoccupation of the electronic states [181]. For Sb_4Te_3, thhe k-grid used for the bulk primitive unit cell is 18x18x18, while thesurface calculations employ a 14x14x1 k-grid using a slab supercell geometry and increasing the c component with 18 $\dot{A}$ to simulate the vaccum [182]. We studied the Sb_2-termination using a slab with 42 atoms of bulk Sb_4Te_3 plus 2 atoms of Sb_2 layer and 4 atoms for BL Sb_2, while the Sb_2Te_3-termination using a slab with 42 atoms of bulk Sb_4Te_3 plus 5 atoms of one QL and 10 atoms for two QL. For Sb_2, thhe k-grid used for the bulk primitive unit cell is 16x16x16, while the calculations with different staking employ a 12x12x1 k-grid and increasing the c component with 18 $\dot{A}$ to simulate the vaccum. We relaxed the structures with spin-orbit effects included.

6.4 Conclusion

In summary, we have carried out an ARPES experiment to study the topological material Sb_4Te_3. Due to its layered structure and composition of two distinct topological insulator materials, it exhibits several topological bands which depend on the surface termination. Despite being a metal, it exhibits topological signatures due to the stacking of two distinct topological insulators. We identified two topological surface states associated with the Sb_2 termination and the Sb_2Te_3 termination, respectively. Although only one of these states is visible as it lies below the Fermi level, both possess a Dirac cone. To confirm their topological nature, we observed a snowflake pattern arising from hexagonal warping, indicating the preservation of time reversal symmetry. This phenomenon suggests a strong spin-orbit coupling, which is the key to the topological nature of Sb_4Te_3. Series of ARPES measurements revealed an invariance upon photon energy change, confirming the surface state nature of these topological surface states.

Using HR-ARPES measurements, we observed two additional electronic bands associated to confined states within a quantum well. Prior studies have indicated that layers of antimony (111) can host quantum well states with specific in-plane band dispersion, a

characteristic we also observed in our measurements. The presence of an Sb_2 termination at the surface indicates the formation of a quantum well in the stacking direction. This configuration results in the parabolic electronic states, as observed in our ARPES measurements.

7. Summary and Outlooks

In this thesis, a combination of different experiental techniques combined with density functional theory were used to investigate the structural and electronic properties of two layered materials: GeS and Sb_4Te_3.

In summary, the first project presented focused on unveiling the surface in-plane ferroelectricity of ultrathin germanium sulfide nano-flakes. Utilizing vapor-phase deposition, we synthesized nano-flakes with varying thicknesses on a highly oriented pyrolytic graphite substrate. A comprehensive investigation employing scanning tunneling microscopy and spectroscopy, complemented by density functional theory calculations, revealed a compelling thickness-dependent tunneling current phenomenon at room temperature. A distinctive hysteresis pattern emerged, indicative of two-dimensional ferroelectric behavior associated with the screening conditions of polarization charges. Notably, this effect becomes more pronounced as the number of layers decreases. The observed behavior holds great promise for applications in miniaturized memory devices, highlighting the unique two-dimensional nature of this phenomenon.

The second project involves the study of the electronic structure of the topological material Sb_4Te_3. High-resolution angle-resolved photoemission spectroscopy combined with density functional theory calculations was employed to investigate the topological behavior of Sb_4Te_3. The study uncovered electronic states arising from spin-orbit coupling, hexagonal warping associated with time reversal symmetry, and no dependency upon photon-energy variation which is characteristic of surface states. Through a comparison with complete bulk and surface bands, we identified a confined electronic state between bulk Sb_4Te_3 and the Sb_2 termination, exhibiting photon-energy independence indicative of confinement along the stacking direction. Additionally, our findings revealed parabolic states associated with stacking faults, enhancing our comprehension of the unique electronic states and topological properties of Sb_4Te_3.

Looking ahead, these projects open avenues for future research. For Project 1, further exploration could involve practical applications of GeS's ferroelectric behavior in memory devices and taking advantage of its two-dimensional character. In Project 2, potential research directions include investigating the tunability of electronic states in Sb_4Te_3 for applications in

quantum computing and emerging technologies. The insights gained from these projects underscore the importance of continued exploration in the field of advanced materials and their transformative impact on diverse technological domains.

8. List of publications

Barreto, R. R.; Ribeiro, T. C.; Miquita, D. R.; Soares, G. H. R.; Pereira, E.; Safar, G. A. M.; Mazzoni, M. S. C.; Malachias, A. and Magalhaes-Paniago, R. Evidence of Thickness-dependent Surface Induced Ferroelectricity in Few-layer Germanium Sulfide obtained via Scanning Tunneling Spectroscopy. *Nanoscale*. (2024) Accepted.

Barreto, R. R.; Rodrigues-Fontenele, G.; Freitas, L. V.; Marçal, L. A. B.; Silva, W. S.; Rodrigues-Junior, G.; Mazzoni, M. S. C.; Malachias, A.; Magalhaes-Paniago, R. and Carbone, D. Co-existence of surface electronic confinement and topological signatures in Sb4Te3. (Submited to ACS Aplied Eletronic Materials)

Ribeiro, T. C.; Fonseca, D. H. S.; **Barreto, R. R**.; Pereira-Andrade, E.; Miquita, D. R.; Malachias, A.; Magalhaes-Paniago, R. Scanning Tunneling Spectroscopy Method for the Prediction of Semiconductor Heterojunction Performance as a Prequel for Device Development. *ACS Applied Materials & Interfaces*, 2024, v. 16, p. 1650-1658. https://doi.org/10.1021/acsami.3c11876

Rodrigues-Junior, G; Chagas, T.; **Reis, R.**; Sciammarella, P. V.; Fornari, C. I; Rappl, P. H. O.; Abramof, E.; Magalhaes-Paniago, R. and Malachias, A. Local surface electronic response of Bi2Te3 topological insulator upon europium doping. *Physical Review B*, 2023, v. 108, p. 035408-1-035408-11. https://doi.org/10.1103/PhysRevB.108.035408

Ribeiro, T. C.; **Reis, R.**; Ferreira, D. C.; Miquita, D. R.; Ribeiro, G. A. S.; Mazzoni, M. S. C.; Malachias, A.; Chagas, T. and Magalhaes-Paniago, R. Electronic gap stability of two-dimensional tin monosulfide phases: Towards optimal structures for electronic device applications. *Applied Surface Science*, 2022, v. 591, p. 153153. https://doi.org/10.1016/j.apsusc.2022.153153

Chagas, T.; Ribeiro, G. A. S.; Rosa, B. L. T.; Bahrami, D.; Davtyan, A.; **Barreto, R. R.**; Gonzales, J. C.; Magalhaes-Paniago, R. and Malachias, A. Mg-Doped GaAs Nanowires with Enhanced Surface Alloying for Use as Ohmic Contacts in Nanoelectronic Devices. *Acs Applied Nano Materials*, 2021, v. 4, p. 12640-12649. https://doi.org/10.1021/acsanm.1c03192

During my PhD, I develop different libraries to treat data for DFT, STM/STS and ARPES. Following contains a list with all libraires developed. All libraries can be found in my Github, https://github.com/rafinhareis.

pyQE -Library for data treatment of QUANTUM EXPRESSO files

ststools - Library for visualization and data treatment of STM images and STS curves of OMICRON and NANOSURF microscopes.

vads – Visualization ARPES data for Sirius. Library for data treatment of ARPES from SIRIUS Syncrothon Light Souce.

References

[1] A. R. P. Montblanch, M. Barbone, I. Aharonovich, M. Atatüre, and A. C. Ferrari, “Layered materials as a platform for quantum technologies,” *Nature Nanotechnology*, vol. 18, no. 6. Nature Research, pp. 555–571, Jun. 01, 2023. doi: 10.1038/s41565-023-01354-x.

[2] H. O. Pastore and L. Marchese, “Themed issue: Layered materials: Structure and properties,” *Journal of Materials Chemistry*, vol. 19, no. 17. pp. 2453–2456, 2009. doi: 10.1039/b904902a.

[3] H. R. Gutiérrez, “Two-Dimensional Layered Materials Offering Expanded Applications in Flatland,” *ACS Applied Nano Materials*, vol. 3, no. 7. American Chemical Society, pp. 6134–6139, Jul. 24, 2020. doi: 10.1021/acsanm.0c01763.

[4] D. Johnson, S. Clarke, J. Wiley, and K. Koumoto, “Layered materials,” *Semiconductor Science and Technology*, vol. 29, no. 6. Institute of Physics Publishing, 2014. doi: 10.1088/0268-1242/29/6/060301.

[5] D. G. Cahill *et al.*, “Nanoscale thermal transport. II. 2003-2012,” *Applied Physics Reviews*, vol. 1, no. 1. American Institute of Physics Inc., 2014. doi: 10.1063/1.4832615.

[6] Z. Guan *et al.*, “Recent Progress in Two-Dimensional Ferroelectric Materials,” *Advanced Electronic Materials*, vol. 6, no. 1. Blackwell Publishing Ltd, Jan. 01, 2020. doi: 10.1002/aelm.201900818.

[7] Z. Zhai *et al.*, “Multi-dimensional materials with layered structures for supercapacitors: Advanced synthesis, supercapacitor performance and functional mechanism,” *Nano Energy*, vol. 78. Elsevier Ltd, Dec. 01, 2020. doi: 10.1016/j.nanoen.2020.105193.

[8] Z. Luo *et al.*, “Anisotropic in-plane thermal conductivity observed in few-layer black phosphorus,” *Nat Commun*, vol. 6, 2015, doi: 10.1038/ncomms9572.

[9] S. Feng *et al.*, “The thermal and electrical transport properties of layered LaCuOSe under high pressure,” *J Alloys Compd*, vol. 861, Apr. 2021, doi: 10.1016/j.jallcom.2020.157984.

[10] P. Zhao *et al.*, “2D layered materials: From materials properties to device applications,” in *Technical Digest - International Electron Devices Meeting, IEDM*, Institute of Electrical and Electronics Engineers Inc., Feb. 2015, pp. 27.3.1-27.3.4. doi: 10.1109/IEDM.2015.7409780.

[11] J. D. Wiley, A. Breitschwerdt, and E. Schönherr, “Optical absorption band edge in single-crystal GeS,” *Solid State Commun*, vol. 17, no. 3, pp. 355–359, Aug. 1975, doi: 10.1016/0038-1098(75)90311-7.

[12] E. Sutter, B. Zhang, M. Sun, and P. Sutter, “Few-Layer to Multilayer Germanium(II) Sulfide: Synthesis, Structure, Stability, and Optoelectronics,” *ACS Nano*, vol. 13, no. 8, pp. 9352–9362, Aug. 2019, doi: 10.1021/acsnano.9b03986.

[13] D. Ma *et al.*, “Ultrathin GeSe Nanosheets: From Systematic Synthesis to Studies of Carrier Dynamics and Applications for a High-Performance UV–Vis Photodetector,” *ACS Appl Mater Interfaces*, vol. 11, no. 4, pp. 4278–4287, Jan. 2019, doi: 10.1021/acsami.8b19836.

[14] J. D. Wiley, S. Pennington, and E. Schönherr, “Anisotropy of the intrinsic photoconductivity of GeS,” *physica status solidi (b)*, vol. 96, no. 1, Nov. 1979, doi: 10.1002/pssb.2220960163.

[15] R. Fei, W. Li, J. Li, and L. Yang, “Giant piezoelectricity of monolayer group IV monochalcogenides: SnSe, SnS, GeSe, and GeS,” *Appl Phys Lett*, vol. 107, no. 17, Oct. 2015, doi: 10.1063/1.4934750.

[16] M. Wu and X. C. Zeng, “Intrinsic Ferroelasticity and/or Multiferroicity in Two-Dimensional Phosphorene and Phosphorene Analogues,” *Nano Lett*, vol. 16, no. 5, pp. 3236–3241, May 2016, doi: 10.1021/acs.nanolett.6b00726.

[17] R. Fei, W. Kang, and L. Yang, “Ferroelectricity and Phase Transitions in Monolayer Group-IV Monochalcogenides,” *Phys Rev Lett*, vol. 117, no. 9, Aug. 2016, doi: 10.1103/PhysRevLett.117.097601.

[18] K. Kushnir, M. Wang, P. Devin Fitzgerald, K. J. Koski, and L. V Titova, “Ultrafast Zero-bias Photocurrent in GeS Nanosheets: Promise for Photovoltaics,” 2017. [Online]. Available: http://pubs.acs.org

[19] N. Latiff, W. Z. Teo, Z. Sofer, Š. Huber, A. C. Fisher, and M. Pumera, “Toxicity of layered semiconductor chalcogenides: beware of interferences,” *RSC Adv*, vol. 5, no. 83, pp. 67485–67492, 2015, doi: 10.1039/C5RA09404F.

[20] E. Sutter and P. Sutter, “1D Wires of 2D Layered Materials: Germanium Sulfide Nanowires as Efficient Light Emitters,” *ACS Appl Nano Mater*, vol. 1, no. 3, pp. 1042–1049, Mar. 2018, doi: 10.1021/acsanm.7b00053.

[21] P. Sutter, S. Wimer, and E. Sutter, “Chiral twisted van der Waals nanowires,” *Nature*, vol. 570, no. 7761, pp. 354–357, Jun. 2019, doi: 10.1038/s41586-019-1147-x.

[22] R. K. Ulaganathan *et al.*, “High photosensitivity and broad spectral response of multi-layered germanium sulfide transistors,” *Nanoscale*, vol. 8, no. 4, pp. 2284–2292, 2016, doi: 10.1039/C5NR05988G.

[23] P. D. Antunez, J. J. Buckley, and R. L. Brutchey, “Tin and germanium monochalcogenide IV–VI semiconductor nanocrystals for use in solar cells,” *Nanoscale*, vol. 3, no. 6, p. 2399, 2011, doi: 10.1039/c1nr10084j.

[24] L. C. Gomes, P. E. Trevisanutto, A. Carvalho, A. S. Rodin, and A. H. Castro Neto, “Strongly bound Mott-Wannier excitons in GeS and GeSe monolayers,” *Phys Rev B*, vol. 94, no. 15, p. 155428, Oct. 2016, doi: 10.1103/PhysRevB.94.155428.

[25] B. R. Tuttle, S. M. Alhassan, and S. T. Pantelides, “Large excitonic effects in group-IV sulfide monolayers,” *Phys Rev B*, vol. 92, no. 23, p. 235405, Dec. 2015, doi: 10.1103/PhysRevB.92.235405.

[26] J. Gou *et al.*, “Two-dimensional ferroelectricity in a single-element bismuth monolayer,” *Nature*, vol. 617, no. 7959, pp. 67–72, May 2023, doi: 10.1038/s41586-023-05848-5.

[27] N. Higashitarumizu *et al.*, “Purely in-plane ferroelectricity in monolayer SnS at room temperature,” *Nat Commun*, vol. 11, no. 1, Dec. 2020, doi: 10.1038/s41467-020-16291-9.

[28] Y. Yan *et al.*, “In-plane ferroelectricity in few-layered GeS and its van der Waals ferroelectric diodes,” *Nanoscale*, vol. 13, no. 38, pp. 16122–16130, Oct. 2021, doi: 10.1039/d1nr03807a.

[29] K. Chang *et al.*, “Discovery of robust in-plane ferroelectricity in atomic-thick SnTe,” *Science (1979)*, vol. 353, no. 6296, pp. 274–278, Jul. 2016, doi: 10.1126/science.aad8609.

[30] C. Cui, F. Xue, W. J. Hu, and L. J. Li, “Two-dimensional materials with piezoelectric and ferroelectric functionalities,” *npj 2D Materials and Applications*, vol. 2, no. 1. Nature Publishing Group, Dec. 01, 2018. doi: 10.1038/s41699-018-0063-5.

[31] M. Wu and P. Jena, “The rise of two-dimensional van der Waals ferroelectrics,” *Wiley Interdisciplinary Reviews: Computational Molecular Science*, vol. 8, no. 5. Blackwell Publishing Inc., Sep. 01, 2018. doi: 10.1002/wcms.1365.

[32] D. Li and D. A. Bonnell, “Controlled patterning of ferroelectric domains: Fundamental concepts and applications,” *Annu Rev Mater Res*, vol. 38, pp. 351–368, 2008, doi: 10.1146/annurev.matsci.37.052506.084303.

[33] J. Z. Larese, T. Arnold, L. Frazier, R. J. Hinde, and A. J. Ramirez-Cuesta, “Direct observation of H2 binding to a metal oxide surface,” *Phys Rev Lett*, vol. 101, no. 16, Oct. 2008, doi: 10.1103/PhysRevLett.101.165302.

[34] J. Rogal, K. Reuter, and M. Scheffler, “First-principles statistical mechanics study of the stability of a subnanometer thin surface oxide in reactive environments: CO oxidation at Pd(100),” *Phys Rev Lett*, vol. 98, no. 4, 2007, doi: 10.1103/PhysRevLett.98.046101.

[35] J. G. Wang *et al.*, “One-dimensional PtO 2 at Pt steps: Formation and reaction with CO,” *Phys Rev Lett*, vol. 95, no. 25, Dec. 2005, doi: 10.1103/PhysRevLett.95.256102.

[36] L. Y. Kraya and R. Kraya, “Determination of the electronic structure of ferroelectric surfaces by scanning tunneling microscopy,” *J Appl Phys*, vol. 111, no. 1, Jan. 2012, doi: 10.1063/1.3675160.

[37] S. Y. Yang *et al.*, “Above-bandgap voltages from ferroelectric photovoltaic devices,” *Nat Nanotechnol*, vol. 5, no. 2, pp. 143–147, 2010, doi: 10.1038/nnano.2009.451.

[38] J. F. Scott, “Applications of modern ferroelectrics,” *Science*, vol. 315, no. 5814. pp. 954–959, Feb. 16, 2007. doi: 10.1126/science.1129564.

[39] H. Zhang, C. X. Liu, X. L. Qi, X. Dai, Z. Fang, and S. C. Zhang, “Topological insulators in Bi 2 Se 3, Bi 2 Te 3 and Sb 2 Te 3 with a single Dirac cone on the surface,” *Nat Phys*, vol. 5, no. 6, pp. 438–442, Jun. 2009, doi: 10.1038/nphys1270.

[40] P. F. P. Poudeu and M. G. Kanatzidis, “Design in solid state chemistry based on phase homologies. Sb 4Te3 and Sb8Te9 as new members of the series (Sb2Te3)m·(Sb 2)n,” *Chemical Communications*, no. 21, pp. 2672–2674, Jun. 2005, doi: 10.1039/b500695c.

[41] Y. Ma, Y. Dai, L. Kou, T. Frauenheim, and T. Heine, “Robust two-dimensional topological insulators in methyl-functionalized bismuth, antimony, and lead bilayer films,” *Nano Lett*, vol. 15, no. 2, pp. 1083–1089, Feb. 2015, doi: 10.1021/nl504037u.

[42] H. L. Zhuang, V. R. Cooper, H. Xu, P. Ganesh, R. G. Hennig, and P. R. C. Kent, “Rashba effect in single-layer antimony telluroiodide SbTeI,” *Phys Rev B Condens Matter Mater Phys*, vol. 92, no. 11, Sep. 2015, doi: 10.1103/PhysRevB.92.115302.

[43] A. Takayama, T. Sato, S. Souma, and T. Takahashi, “Rashba effect in antimony and bismuth studied by spin-resolved ARPES,” *New J Phys*, vol. 16, 2014, doi: 10.1088/1367-2630/16/5/055004.

[44] T. R. Chang *et al.*, “Band topology of bismuth quantum films,” *Crystals (Basel)*, vol. 9, no. 10, Oct. 2019, doi: 10.3390/cryst9100510.

[45] I. N. Yakovkin and N. V. Petrova, “Band structure of free Sb layers and spin-orbit splitting of surface bands,” *Physics Letters, Section A: General, Atomic and Solid State Physics*, vol. 430, Apr. 2022, doi: 10.1016/j.physleta.2022.127987.

[46] T.-C. Chiang, “Photoemission studies of quantum well states in thin films,” *Surf Sci Rep*, vol. 39, no. 7–8, pp. 181–235, Sep. 2000, doi: 10.1016/S0167-5729(00)00006-6.

[47] Samares Kar, *High Permittivity Gate Dielectric Materials*, 1st ed., vol. 13. in Springer Series in Advanced Microelectronics, vol. 13. Berlin, Heidelberg: Springer Berlin Heidelberg, 2013. doi: 10.1007/978-3-642-36535-5.

[48] F. Q. Wang, S. Zhang, J. Yu, and Q. Wang, “Thermoelectric properties of single-layered SnSe sheet,” *Nanoscale*, vol. 7, no. 38, pp. 15962–15970, 2015, doi: 10.1039/C5NR03813H.

[49] G. Ramalingam *et al.*, “Quantum Confinement Effect of 2D Nanomaterials,” in *Quantum Dots - Fundamental and Applications*, IntechOpen, 2020. doi: 10.5772/intechopen.90140.

[50] S. Yang, F. Liu, C. Wu, and S. Yang, “Tuning Surface Properties of Low Dimensional Materials via Strain Engineering,” *Small*, vol. 12, no. 30, pp. 4028–4047, Aug. 2016, doi: 10.1002/smll.201601203.

[51] M. Xia, “A Review on Applications of Two-Dimensional Materials in Surface-Enhanced Raman Spectroscopy,” *Int J Spectrosc*, vol. 2018, pp. 1–9, Jan. 2018, doi: 10.1155/2018/4861472.

[52] J. Tan, Y. Chen, J. He, L. G. Occhipinti, Z. Wang, and X. Zhou, “Two-dimensional material-enhanced surface plasmon resonance for antibiotic sensing,” *J Hazard Mater*, vol. 455, p. 131644, Aug. 2023, doi: 10.1016/j.jhazmat.2023.131644.

[53] B. M. Sow, J. Lu, H. Liu, K. E. J. Goh, and C. H. Sow, “2D Materials: Enriched Fluorescence Emission from WS Monoflake Empowered by Au Nanoexplorers (Advanced Optical Materials 14/2017),” *Adv Opt Mater*, vol. 5, no. 14, Jul. 2017, doi: 10.1002/adom.201770075.

[54] M. Bernardi, C. Ataca, M. Palummo, and J. C. Grossman, “Optical and Electronic Properties of Two-Dimensional Layered Materials,” *Nanophotonics*, vol. 6, no. 2, pp. 479–493, Mar. 2017, doi: 10.1515/nanoph-2015-0030.

[55] P. Kumbhakar, C. Chowde Gowda, and C. S. Tiwary, “Advance Optical Properties and Emerging Applications of 2D Materials,” *Front Mater*, vol. 8, Aug. 2021, doi: 10.3389/fmats.2021.721514.

[56] J. H. Kim, J. H. Jeong, N. Kim, R. Joshi, and G.-H. Lee, “Mechanical properties of two-dimensional materials and their applications,” *J Phys D Appl Phys*, vol. 52, no. 8, p. 083001, Feb. 2019, doi: 10.1088/1361-6463/aaf465.

[57] C. Androulidakis, K. Zhang, M. Robertson, and S. Tawfick, “Tailoring the mechanical properties of 2D materials and heterostructures,” *2d Mater*, vol. 5, no. 3, p. 032005, Jun. 2018, doi: 10.1088/2053-1583/aac764.

[58] M. Sharma, P. M. Ajayan, and P. Deb, “Quantum Energy Storage in 2D Heterointerfaces,” *Adv Mater Interfaces*, vol. 10, no. 11, Apr. 2023, doi: 10.1002/admi.202202058.

[59] V. K. Sangwan and M. C. Hersam, “Electronic Transport in Two-Dimensional Materials,” *Annu Rev Phys Chem*, vol. 69, no. 1, pp. 299–325, Apr. 2018, doi: 10.1146/annurev-physchem-050317-021353.

[60] J. Wang, V. Malgras, Y. Sugahara, and Y. Yamauchi, “Electrochemical energy storage performance of 2D nanoarchitectured hybrid materials,” *Nat Commun*, vol. 12, no. 1, p. 3563, Jun. 2021, doi: 10.1038/s41467-021-23819-0.

[61] Y. Yang *et al.*, “The Role of Geometric Sites in 2D Materials for Energy Storage,” *Joule*, vol. 2, no. 6, pp. 1075–1094, Jun. 2018, doi: 10.1016/j.joule.2018.04.027.

[62] Y. Li, Y. Sun, G. Na, W. A. Saidi, and L. Zhang, “Diverse electronic properties of 2D layered Se-containing materials composed of quasi-1D atomic chains,” *Physical Chemistry Chemical Physics*, vol. 22, no. 4, pp. 2122–2129, 2020, doi: 10.1039/C9CP05914H.

[63] R. Vargas-Bernal, “Electrical Properties of Two-Dimensional Materials Used in Gas Sensors,” *Sensors*, vol. 19, no. 6, p. 1295, Mar. 2019, doi: 10.3390/s19061295.

[64] T. Dutta *et al.*, “Electronic properties of 2D materials and their junctions,” *Nano Materials Science*, Jun. 2023, doi: 10.1016/j.nanoms.2023.05.003.

[65] S. Zhang, R. Xu, N. Luo, and X. Zou, “Two-dimensional magnetic materials: structures, properties and external controls,” *Nanoscale*, vol. 13, no. 3, pp. 1398–1424, 2021, doi: 10.1039/D0NR06813F.

[66] Q. H. Wang *et al.*, “The Magnetic Genome of Two-Dimensional van der Waals Materials,” *ACS Nano*, vol. 16, no. 5, pp. 6960–7079, May 2022, doi: 10.1021/acsnano.1c09150.

[67] X. Jiang *et al.*, “Recent progress on 2D magnets: Fundamental mechanism, structural design and modification,” *Appl Phys Rev*, vol. 8, no. 3, Sep. 2021, doi: 10.1063/5.0039979.

[68] P. Tipler, *Física Moderna*, 6th ed. LTC, 2014.

[69] M. Kohmoto, “Topological invariant and the quantization of the Hall conductance,” *Ann Phys (N Y)*, vol. 160, no. 2, pp. 343–354, Apr. 1985, doi: 10.1016/0003-4916(85)90148-4.

[70] K. v. Klitzing, G. Dorda, and M. Pepper, “New Method for High-Accuracy Determination of the Fine-Structure Constant Based on Quantized Hall Resistance,” *Phys Rev Lett*, vol. 45, no. 6, pp. 494–497, Aug. 1980, doi: 10.1103/PhysRevLett.45.494.

[71] S. A. Mikhailov, “A new approach to the ground state of quantum Hall systems. Basic principles,” *Physica B Condens Matter*, vol. 299, no. 1–2, pp. 6–31, May 2001, doi: 10.1016/S0921-4526(00)00769-9.

[72] X.-L. Qi and S.-C. Zhang, “Topological insulators and superconductors,” *Rev Mod Phys*, vol. 83, no. 4, pp. 1057–1110, Oct. 2011, doi: 10.1103/RevModPhys.83.1057.

[73] J. E. Moore and L. Balents, “Topological invariants of time-reversal-invariant band structures,” *Phys Rev B*, vol. 75, no. 12, p. 121306, Mar. 2007, doi: 10.1103/PhysRevB.75.121306.

[74] J. Sakurai, *Modern Quantum Mechanics*, 2nd ed. Cambridge University Press, 2017.

[75] C. Wu, B. A. Bernevig, and S.-C. Zhang, “Helical Liquid and the Edge of Quantum Spin Hall Systems,” *Phys Rev Lett*, vol. 96, no. 10, p. 106401, Mar. 2006, doi: 10.1103/PhysRevLett.96.106401.

[76] D. J. Thouless, M. Kohmoto, M. P. Nightingale, and M. den Nijs, “Quantized Hall Conductance in a Two-Dimensional Periodic Potential,” *Phys Rev Lett*, vol. 49, no. 6, pp. 405–408, Aug. 1982, doi: 10.1103/PhysRevLett.49.405.

[77] S. Weinberg, *The Quantum Theory of Fields*, 1st ed., vol. 1. Austin: Cambridge University Press, 1995.

[78] M. Z. Hasan and C. L. Kane, “Colloquium : Topological insulators,” *Rev Mod Phys*, vol. 82, no. 4, pp. 3045–3067, Nov. 2010, doi: 10.1103/RevModPhys.82.3045.

[79] C. L. Kane and E. J. Mele, “A New Spin on the Insulating State,” *Science (1979)*, vol. 314, no. 5806, pp. 1692–1693, Dec. 2006, doi: 10.1126/science.1136573.

[80] B. A. Bernevig, T. L. Hughes, and S.-C. Zhang, “Quantum Spin Hall Effect and Topological Phase Transition in HgTe Quantum Wells,” *Science (1979)*, vol. 314, no. 5806, pp. 1757–1761, Dec. 2006, doi: 10.1126/science.1133734.

[81] M. König *et al.*, “Quantum Spin Hall Insulator State in HgTe Quantum Wells,” *Science (1979)*, vol. 318, no. 5851, pp. 766–770, Nov. 2007, doi: 10.1126/science.1148047.

[82] C. L. Kane and E. J. Mele, “Z2 Topological Order and the Quantum Spin Hall Effect,” *Phys Rev Lett*, vol. 95, no. 14, p. 146802, Sep. 2005, doi: 10.1103/PhysRevLett.95.146802.

[83] M. Z. Hasan and J. E. Moore, “Three-Dimensional Topological Insulators,” *Annu Rev Condens Matter Phys*, vol. 2, no. 1, pp. 55–78, Mar. 2011, doi: 10.1146/annurev-conmatphys-062910-140432.

[84] Y. Xia *et al.*, “Observation of a large-gap topological-insulator class with a single Dirac cone on the surface,” *Nat Phys*, vol. 5, no. 6, pp. 398–402, Jun. 2009, doi: 10.1038/nphys1274.

[85] C. Lamuta, “Elastic constants determination of anisotropic materials by depth-sensing indentation,” *SN Appl Sci*, vol. 1, no. 10, p. 1263, Oct. 2019, doi: 10.1007/s42452-019-1301-y.

[86] L. Fu, “Hexagonal warping effects in the surface states of the topological insulator Bi2Te3,” *Phys Rev Lett*, vol. 103, no. 26, Dec. 2009, doi: 10.1103/PhysRevLett.103.266801.

[87] Y. L. Chen *et al.*, “Experimental Realization of a Three-Dimensional Topological Insulator, Bi2Te3,” *Science (1979)*, vol. 325, no. 5937, pp. 178–181, Jul. 2009, doi: 10.1126/science.1173034.

[88] L. Fu, “Hexagonal warping effects in the surface states of the topological insulator Bi2Te3,” *Phys Rev Lett*, vol. 103, no. 26, Dec. 2009, doi: 10.1103/PhysRevLett.103.266801.

[89] A. J. Moulson and J. M. Herbert, *Electroceramics*, 2nd ed. Wiley, 2003. doi: 10.1002/0470867965.

[90] A. Rodriguez-Fortea, P. Alemany, and T. Ziegler, “Density Functional Calculations of NMR Chemical Shifts with the Inclusion of Spin−Orbit Coupling in Tungsten and Lead Compounds,” *J Phys Chem A*, vol. 103, no. 41, pp. 8288–8294, Oct. 1999, doi: 10.1021/jp9912004.

[91] G. Saielli, A. Bagno, F. Castiglione, R. Simonutti, M. Mauri, and A. Mele, “Understanding Cage Effects in Imidazolium Ionic Liquids by 129 Xe NMR: MD Simulations and

Relativistic DFT Calculations," *J Phys Chem B*, vol. 118, no. 48, pp. 13963–13968, Dec. 2014, doi: 10.1021/jp511207s.

[92] A. Alam, B. Kraczek, and D. D. Johnson, "Structural, magnetic, and defect properties of Co-Pt-type magnetic-storage alloys: Density-functional theory study of thermal processing effects," *Phys Rev B*, vol. 82, no. 2, p. 024435, Jul. 2010, doi: 10.1103/PhysRevB.82.024435.

[93] P. Hohenberg and W. Kohn, "Inhomogeneous Electron Gas," *Physical Review*, vol. 136, no. 3B, pp. B864–B871, Nov. 1964, doi: 10.1103/PhysRev.136.B864.

[94] D. Vanderbilt, *Berry Phases in Electronic Structure Theory: Electric Polarization, Orbital Magnetization and Topological Insulators*, 1st ed. Cambridge: Cambridge University Press, 2018.

[95] R. Martin, *Electronic Structure: Basic Theory and Practical Methods*, 1st ed. Cambridge : Cambridge University Press, 2008.

[96] W. Kohn and L. J. Sham, "Self-Consistent Equations Including Exchange and Correlation Effects," *Physical Review*, vol. 140, no. 4A, pp. A1133–A1138, Nov. 1965, doi: 10.1103/PhysRev.140.A1133.

[97] D. M. Ceperley and B. J. Alder, "Ground State of the Electron Gas by a Stochastic Method," *Phys Rev Lett*, vol. 45, no. 7, pp. 566–569, Aug. 1980, doi: 10.1103/PhysRevLett.45.566.

[98] P. Haas, F. Tran, and P. Blaha, "Calculation of the lattice constant of solids with semilocal functionals," *Phys Rev B*, vol. 79, no. 8, p. 085104, Feb. 2009, doi: 10.1103/PhysRevB.79.085104.

[99] A. D. Becke, "Density-functional exchange-energy approximation with correct asymptotic behavior," *Phys Rev A (Coll Park)*, vol. 38, no. 6, pp. 3098–3100, Sep. 1988, doi: 10.1103/PhysRevA.38.3098.

[100] J. P. Perdew, K. Burke, and M. Ernzerhof, "Generalized Gradient Approximation Made Simple," 1996.

[101] A. P. Bartók and J. R. Yates, “Ultrasoft pseudopotentials with kinetic energy density support: Implementing the Tran-Blaha potential,” *Phys Rev B*, vol. 99, no. 23, p. 235103, Jun. 2019, doi: 10.1103/PhysRevB.99.235103.

[102] D. R. Hamann, M. Schlüter, and C. Chiang, “Norm-Conserving Pseudopotentials,” *Phys Rev Lett*, vol. 43, no. 20, pp. 1494–1497, Nov. 1979, doi: 10.1103/PhysRevLett.43.1494.

[103] D. Vanderbilt, “Soft self-consistent pseudopotentials in a generalized eigenvalue formalism,” *Phys Rev B*, vol. 41, no. 11, pp. 7892–7895, Apr. 1990, doi: 10.1103/PhysRevB.41.7892.

[104] P. Giannozzi *et al.*, “QUANTUM ESPRESSO: a modular and open-source software project for quantum simulations of materials,” *Journal of Physics: Condensed Matter*, vol. 21, no. 39, p. 395502, Sep. 2009, doi: 10.1088/0953-8984/21/39/395502.

[105] G. Kresse and J. Hafner, “Ab initio molecular dynamics for liquid metals,” *Phys Rev B*, vol. 47, no. 1, pp. 558–561, Jan. 1993, doi: 10.1103/PhysRevB.47.558.

[106] E. Artacho *et al.*, “The SIESTA method; Developments and applicability,” *Journal of Physics Condensed Matter*, vol. 20, no. 6, Feb. 2008, doi: 10.1088/0953-8984/20/6/064208.

[107] G. Binnig, H. Rohrer, Ch. Gerber, and E. Weibel, “Surface Studies by Scanning Tunneling Microscopy,” *Phys Rev Lett*, vol. 49, no. 1, pp. 57–61, Jul. 1982, doi: 10.1103/PhysRevLett.49.57.

[108] G. Binnig, H. Rohrer, Ch. Gerber, and E. Weibel, “Surface Studies by Scanning Tunneling Microscopy,” *Phys Rev Lett*, vol. 49, no. 1, pp. 57–61, Jul. 1982, doi: 10.1103/PhysRevLett.49.57.

[109] C. J. Chen, *Introduction to Scanning Tunneling Microscopy Third Edition*, 2nd ed. Oxford: Oxford University Press, 2021.

[110] L. E. Ballentine, *Quantum Mechanics*. WORLD SCIENTIFIC, 1998. doi: 10.1142/3142.

[111] G. Binnig, H. Rohrer, Ch. Gerber, and E. Weibel, “Tunneling through a controllable vacuum gap,” *Appl Phys Lett*, vol. 40, no. 2, pp. 178–180, Jan. 1982, doi: 10.1063/1.92999.

[112] J. Tersoff and D. R. Hamann, “Theory of the scanning tunneling microscope,” *Phys Rev B*, vol. 31, no. 2, pp. 805–813, Jan. 1985, doi: 10.1103/PhysRevB.31.805.

[113] J. Bardeen, “Tunnelling from a Many-Particle Point of View,” *Phys Rev Lett*, vol. 6, no. 2, pp. 57–59, Jan. 1961, doi: 10.1103/PhysRevLett.6.57.

[114] A. Damascelli, Z. Hussain, and Z.-X. Shen, “Angle-resolved photoemission studies of the cuprate superconductors,” *Rev Mod Phys*, vol. 75, no. 2, pp. 473–541, Apr. 2003, doi: 10.1103/RevModPhys.75.473.

[115] C. N. Berglund and W. E. Spicer, “Photoemission Studies of Copper and Silver: Theory,” *Physical Review*, vol. 136, no. 4A, pp. A1030–A1044, Nov. 1964, doi: 10.1103/PhysRev.136.A1030.

[116] F. Reinert and S. Hüfner, “Photoemission spectroscopy—from early days to recent applications,” *New J Phys*, vol. 7, pp. 97–97, Apr. 2005, doi: 10.1088/1367-2630/7/1/097.

[117] S. Hüfner, *Photoelectron Spectroscopy*. Berlin, Heidelberg: Springer Berlin Heidelberg, 2003. doi: 10.1007/978-3-662-09280-4.

[118] R. Kurleto and J. Fink, “About two-dimensional fits for the analysis of the scattering rates and renormalization functions from angle-resolved photoelectron spectroscopy data,” *J Electron Spectros Relat Phenomena*, vol. 253, p. 147127, Dec. 2021, doi: 10.1016/j.elspec.2021.147127.

[119] J. Fink *et al.*, “Linkage between scattering rates and superconductivity in doped ferropnictides,” *Phys Rev B*, vol. 103, no. 15, p. 155119, Apr. 2021, doi: 10.1103/PhysRevB.103.155119.

[120] T. Valla, A. V. Fedorov, P. D. Johnson, and S. L. Hulbert, “Many-Body Effects in Angle-Resolved Photoemission: Quasiparticle Energy and Lifetime of a Mo(110) Surface State,” *Phys Rev Lett*, vol. 83, no. 10, pp. 2085–2088, Sep. 1999, doi: 10.1103/PhysRevLett.83.2085.

[121] P. Richard, T. Sato, K. Nakayama, T. Takahashi, and H. Ding, “Fe-based superconductors: an angle-resolved photoemission spectroscopy perspective,” *Reports on Progress in Physics*, vol. 74, no. 12, p. 124512, Dec. 2011, doi: 10.1088/0034-4885/74/12/124512.

[122] A. Tamai *et al.*, “Spin-orbit splitting of the Shockley surface state on Cu(111),” *Phys Rev B*, vol. 87, no. 7, p. 075113, Feb. 2013, doi: 10.1103/PhysRevB.87.075113.

[123] D. Haberer, “Electronic Properties of Functionalized Graphene Studied With Photoemis- sion Spectroscopy,” PhD, Technische Universität Dresden, Dresden, 2012.

[124] D. Li and D. A. Bonnell, “Controlled patterning of ferroelectric domains: Fundamental concepts and applications,” *Annu Rev Mater Res*, vol. 38, pp. 351–368, 2008, doi: 10.1146/annurev.matsci.37.052506.084303.

[125] J. Z. Larese, T. Arnold, L. Frazier, R. J. Hinde, and A. J. Ramirez-Cuesta, “Direct observation of H2 binding to a metal oxide surface,” *Phys Rev Lett*, vol. 101, no. 16, Oct. 2008, doi: 10.1103/PhysRevLett.101.165302.

[126] J. Rogal, K. Reuter, and M. Scheffler, “First-principles statistical mechanics study of the stability of a subnanometer thin surface oxide in reactive environments: CO oxidation at Pd(100),” *Phys Rev Lett*, vol. 98, no. 4, 2007, doi: 10.1103/PhysRevLett.98.046101.

[127] J. G. Wang *et al.*, “One-dimensional PtO 2 at Pt steps: Formation and reaction with CO,” *Phys Rev Lett*, vol. 95, no. 25, Dec. 2005, doi: 10.1103/PhysRevLett.95.256102.

[128] L. Y. Kraya and R. Kraya, “Determination of the electronic structure of ferroelectric surfaces by scanning tunneling microscopy,” *J Appl Phys*, vol. 111, no. 1, Jan. 2012, doi: 10.1063/1.3675160.

[129] S. Y. Yang *et al.*, “Above-bandgap voltages from ferroelectric photovoltaic devices,” *Nat Nanotechnol*, vol. 5, no. 2, pp. 143–147, 2010, doi: 10.1038/nnano.2009.451.

[130] J. F. Scott, “Applications of modern ferroelectrics,” *Science*, vol. 315, no. 5814. pp. 954–959, Feb. 16, 2007. doi: 10.1126/science.1129564.

[131] C. Cui, F. Xue, W. J. Hu, and L. J. Li, “Two-dimensional materials with piezoelectric and ferroelectric functionalities,” *npj 2D Materials and Applications*, vol. 2, no. 1. Nature Publishing Group, Dec. 01, 2018. doi: 10.1038/s41699-018-0063-5.

[132] Z. Guan *et al.*, “Recent Progress in Two-Dimensional Ferroelectric Materials,” *Adv Electron Mater*, vol. 6, no. 1, Jan. 2020, doi: 10.1002/aelm.201900818.

[133] M. Wu and P. Jena, “The rise of two-dimensional van der Waals ferroelectrics,” *Wiley Interdisciplinary Reviews: Computational Molecular Science*, vol. 8, no. 5. Blackwell Publishing Inc., Sep. 01, 2018. doi: 10.1002/wcms.1365.

[134] J. Gou *et al.*, “Two-dimensional ferroelectricity in a single-element bismuth monolayer,” *Nature*, vol. 617, no. 7959, pp. 67–72, May 2023, doi: 10.1038/s41586-023-05848-5.

[135] N. Higashitarumizu *et al.*, “Purely in-plane ferroelectricity in monolayer SnS at room temperature,” *Nat Commun*, vol. 11, no. 1, Dec. 2020, doi: 10.1038/s41467-020-16291-9.

[136] Y. Yan *et al.*, “In-plane ferroelectricity in few-layered GeS and its van der Waals ferroelectric diodes,” *Nanoscale*, vol. 13, no. 38, pp. 16122–16130, Oct. 2021, doi: 10.1039/d1nr03807a.

[137] K. Chang *et al.*, “Discovery of robust in-plane ferroelectricity in atomic-thick SnTe,” *Science (1979)*, vol. 353, no. 6296, pp. 274–278, Jul. 2016, doi: 10.1126/science.aad8609.

[138] L. Makinistian and E. A. Albanesi, “First-principles calculations of the band gap and optical properties of germanium sulfide,” *Phys Rev B*, vol. 74, no. 4, p. 045206, Jul. 2006, doi: 10.1103/PhysRevB.74.045206.

[139] Y. J. Cho *et al.*, “Germanium sulfide(ii and iv) nanoparticles for enhanced performance of lithium ion batteries,” *Chemical Communications*, vol. 49, no. 41, p. 4661, 2013, doi: 10.1039/c3cc41853g.

[140] L. Lutterotti, “Maud: a Rietveld analysis program designed for the internet and experiment integration,” *Acta Crystallogr A*, vol. 56, no. s1, pp. s54–s54, Aug. 2000, doi: 10.1107/s0108767300021954.

[141] P. Sutter, R. Ibragimova, H.-P. Komsa, B. A. Parkinson, and E. Sutter, “Self-organized twist-heterostructures via aligned van der Waals epitaxy and solid-state transformations,” *Nat Commun*, vol. 10, no. 1, p. 5528, Dec. 2019, doi: 10.1038/s41467-019-13488-5.

[142] B. L. Henke, E. M. Gullikson, and J. C. Davis, “X-Ray Interactions: Photoabsorption, Scattering, Transmission, and Reflection at E = 50-30,000 eV, Z = 1-92,” *At Data Nucl Data Tables*, vol. 54, no. 2, pp. 181–342, Jul. 1993, doi: 10.1006/adnd.1993.1013.

[143] D. R. G. Mitchell, “DiffTools: Electron diffraction software tools for DigitalMicrograph™,” *Microsc Res Tech*, vol. 71, no. 8, pp. 588–593, Aug. 2008, doi: 10.1002/jemt.20591.

[144] G. Kresse and J. Furthmüller, “Efficient iterative schemes for ab initio total-energy calculations using a plane-wave basis set,” *Phys Rev B*, vol. 54, no. 16, pp. 11169–11186, Oct. 1996, doi: 10.1103/PhysRevB.54.11169.

[145] J. Heyd, G. E. Scuseria, and M. Ernzerhof, “Hybrid functionals based on a screened Coulomb potential,” *J Chem Phys*, vol. 118, no. 18, pp. 8207–8215, May 2003, doi: 10.1063/1.1564060.

[146] E. Sutter, B. Zhang, M. Sun, and P. Sutter, “Few-Layer to Multilayer Germanium(II) Sulfide: Synthesis, Structure, Stability, and Optoelectronics,” *ACS Nano*, vol. 13, no. 8, pp. 9352–9362, Aug. 2019, doi: 10.1021/acsnano.9b03986.

[147] E. D. Farias, M. E. Zoloff Michoff, V. Sueldo Occello, V. Brunetti, M. C. G. Passeggi (Jr.), and T. Glatzel, “KPFM and DFT as tools to correlate the charge distribution and molecular orientation of dendritic adsorbates on different surfaces,” *Appl Surf Sci*, vol. 565, p. 150552, Nov. 2021, doi: 10.1016/j.apsusc.2021.150552.

[148] R. Fei, W. Kang, and L. Yang, “Robust Ferroelectricity in Monolayer Group-IV Monochalcogenides,” Apr. 2016, doi: 10.1103/PhysRevLett.117.097601.

[149] K. Chang *et al.*, “Microscopic Manipulation of Ferroelectric Domains in SnSe Monolayers at Room Temperature,” *Nano Lett*, vol. 20, no. 9, pp. 6590–6597, Sep. 2020, doi: 10.1021/acs.nanolett.0c02357.

[150] M. Wu and X. C. Zeng, “Intrinsic Ferroelasticity and/or Multiferroicity in Two-Dimensional Phosphorene and Phosphorene Analogues,” *Nano Lett*, vol. 16, no. 5, pp. 3236–3241, May 2016, doi: 10.1021/acs.nanolett.6b00726.

[151] Z. Guan *et al.*, “Recent Progress in Two-Dimensional Ferroelectric Materials,” *Adv Electron Mater*, vol. 6, no. 1, Jan. 2020, doi: 10.1002/aelm.201900818.

[152] A. R. P. Montblanch, M. Barbone, I. Aharonovich, M. Atatüre, and A. C. Ferrari, “Layered materials as a platform for quantum technologies,” *Nature Nanotechnology*, vol. 18, no. 6. Nature Research, pp. 555–571, Jun. 01, 2023. doi: 10.1038/s41565-023-01354-x.

[153] H. O. Pastore and L. Marchese, “Themed issue: Layered materials: Structure and properties,” *Journal of Materials Chemistry*, vol. 19, no. 17. pp. 2453–2456, 2009. doi: 10.1039/b904902a.

[154] H. R. Gutiérrez, “Two-Dimensional Layered Materials Offering Expanded Applications in Flatland,” *ACS Applied Nano Materials*, vol. 3, no. 7. American Chemical Society, pp. 6134–6139, Jul. 24, 2020. doi: 10.1021/acsanm.0c01763.

[155] D. Johnson, S. Clarke, J. Wiley, and K. Koumoto, “Layered materials,” *Semiconductor Science and Technology*, vol. 29, no. 6. Institute of Physics Publishing, 2014. doi: 10.1088/0268-1242/29/6/060301.

[156] D. G. Cahill *et al.*, “Nanoscale thermal transport. II. 2003-2012,” *Applied Physics Reviews*, vol. 1, no. 1. American Institute of Physics Inc., 2014. doi: 10.1063/1.4832615.

[157] Z. Guan *et al.*, “Recent Progress in Two-Dimensional Ferroelectric Materials,” *Advanced Electronic Materials*, vol. 6, no. 1. Blackwell Publishing Ltd, Jan. 01, 2020. doi: 10.1002/aelm.201900818.

[158] G. Yu *et al.*, “Understanding charge storage in hydrated layered solids MOPO4 (M = V, Nb) with tunable interlayer chemistry,” *ACS Nano*, vol. 14, no. 10, pp. 13824–13833, Oct. 2020, doi: 10.1021/acsnano.0c06193.

[159] Z. Zhai *et al.*, “Multi-dimensional materials with layered structures for supercapacitors: Advanced synthesis, supercapacitor performance and functional mechanism,” *Nano Energy*, vol. 78. Elsevier Ltd, Dec. 01, 2020. doi: 10.1016/j.nanoen.2020.105193.

[160] Z. Luo *et al.*, “Anisotropic in-plane thermal conductivity observed in few-layer black phosphorus,” *Nat Commun*, vol. 6, 2015, doi: 10.1038/ncomms9572.

[161] S. Feng *et al.*, “The thermal and electrical transport properties of layered LaCuOSe under high pressure,” *J Alloys Compd*, vol. 861, Apr. 2021, doi: 10.1016/j.jallcom.2020.157984.

[162] J. Yao and G. Yang, “2D Layered Material Alloys: Synthesis and Application in Electronic and Optoelectronic Devices,” *Advanced Science*, vol. 9, no. 1. John Wiley and Sons Inc, Jan. 01, 2022. doi: 10.1002/advs.202103036.

[163] P. Zhao *et al.*, “2D layered materials: From materials properties to device applications,” in *2015 IEEE International Electron Devices Meeting (IEDM)*, IEEE, Dec. 2015, pp. 27.3.1-27.3.4. doi: 10.1109/IEDM.2015.7409780.

[164] P. F. P. Poudeu and M. G. Kanatzidis, “Design in solid state chemistry based on phase homologies. Sb 4Te3 and Sb8Te9 as new members of the series (Sb2Te3)m·(Sb 2)n,” *Chemical Communications*, no. 21, pp. 2672–2674, Jun. 2005, doi: 10.1039/b500695c.

[165] Y. Ma, Y. Dai, L. Kou, T. Frauenheim, and T. Heine, “Robust two-dimensional topological insulators in methyl-functionalized bismuth, antimony, and lead bilayer films,” *Nano Lett*, vol. 15, no. 2, pp. 1083–1089, Feb. 2015, doi: 10.1021/nl504037u.

[166] H. Zhang, C. X. Liu, X. L. Qi, X. Dai, Z. Fang, and S. C. Zhang, “Topological insulators in Bi 2 Se 3, Bi 2 Te 3 and Sb 2 Te 3 with a single Dirac cone on the surface,” *Nat Phys*, vol. 5, no. 6, pp. 438–442, Jun. 2009, doi: 10.1038/nphys1270.

[167] H. L. Zhuang, V. R. Cooper, H. Xu, P. Ganesh, R. G. Hennig, and P. R. C. Kent, “Rashba effect in single-layer antimony telluroiodide SbTeI,” *Phys Rev B Condens Matter Mater Phys*, vol. 92, no. 11, Sep. 2015, doi: 10.1103/PhysRevB.92.115302.

[168] A. Takayama, T. Sato, S. Souma, and T. Takahashi, “Rashba effect in antimony and bismuth studied by spin-resolved ARPES,” *New J Phys*, vol. 16, 2014, doi: 10.1088/1367-2630/16/5/055004.

[169] I. N. Yakovkin and N. V. Petrova, “Band structure of free Sb layers and spin-orbit splitting of surface bands,” *Physics Letters, Section A: General, Atomic and Solid State Physics*, vol. 430, Apr. 2022, doi: 10.1016/j.physleta.2022.127987.

[170] T.-C. Chiang, “Photoemission studies of quantum well states in thin films,” *Surf Sci Rep*, vol. 39, no. 7–8, pp. 181–235, Sep. 2000, doi: 10.1016/S0167-5729(00)00006-6.

[171] I. K. Robinson, “Crystal truncation rods and surface roughness,” *Phys Rev B*, vol. 33, no. 6, pp. 3830–3836, Mar. 1986, doi: 10.1103/PhysRevB.33.3830.

[172] C. Xu *et al.*, “Topological Type-II Dirac Fermions Approaching the Fermi Level in a Transition Metal Dichalcogenide NiTe2,” *Chemistry of Materials*, vol. 30, no. 14, pp. 4823–4830, Jul. 2018, doi: 10.1021/acs.chemmater.8b02132.

[173] T. Chagas *et al.*, “Multiple strong topological gaps and hexagonal warping in Bi4Te3,” *Phys Rev B*, vol. 105, no. 8, Feb. 2022, doi: 10.1103/PhysRevB.105.L081409.

[174] J. Hu, Z. Zhu, and R. Wu, “Chern half metals: A new class of topological materials to realize the quantum anomalous hall effect,” *Nano Lett*, vol. 15, no. 3, pp. 2074–2078, Mar. 2015, doi: 10.1021/nl504981g.

[175] H. Pan, M. Xie, F. Wu, and S. Das Sarma, “Topological Phases in AB-Stacked MoTe2/WSe2: Z2 Topological Insulators, Chern Insulators, and Topological Charge Density Waves,” *Phys Rev Lett*, vol. 129, no. 5, Jul. 2022, doi: 10.1103/PhysRevLett.129.056804.

[176] P. Zhang, P. Richard, T. Qian, Y.-M. Xu, X. Dai, and H. Ding, “A precise method for visualizing dispersive features in image plots,” *Review of Scientific Instruments*, vol. 82, no. 4, Apr. 2011, doi: 10.1063/1.3585113.

[177] T. R. Chang *et al.*, “Band topology of bismuth quantum films,” *Crystals (Basel)*, vol. 9, no. 10, Oct. 2019, doi: 10.3390/cryst9100510.

[178] K. Sugawara, T. Sato, S. Souma, T. Takahashi, M. Arai, and T. Sasaki, “Fermi Surface and Anisotropic Spin-Orbit Coupling of Sb(111) Studied by Angle-Resolved Photoemission Spectroscopy,” *Phys Rev Lett*, vol. 96, no. 4, p. 046411, Feb. 2006, doi: 10.1103/PhysRevLett.96.046411.

[179] P. Giannozzi *et al.*, “QUANTUM ESPRESSO: a modular and open-source software project for quantum simulations of materials,” *Journal of Physics: Condensed Matter*, vol. 21, no. 39, p. 395502, Sep. 2009, doi: 10.1088/0953-8984/21/39/395502.

[180] J. P. Perdew, K. Burke, and M. Ernzerhof, “Generalized Gradient Approximation Made Simple,” 1996.

[181] N. Marzari, D. Vanderbilt, A. De Vita, and M. C. Payne, “Thermal Contraction and Disordering of the Al(110) Surface,” *Phys Rev Lett*, vol. 82, no. 16, pp. 3296–3299, Apr. 1999, doi: 10.1103/PhysRevLett.82.3296.

[182] M. L. Cohen, M. Schlüter, J. R. Chelikowsky, and S. G. Louie, “Self-consistent pseudopotential method for localized configurations: Molecules,” *Phys Rev B*, vol. 12, no. 12, pp. 5575–5579, Dec. 1975, doi: 10.1103/PhysRevB.12.5575.